PHASE CONJUGATION VIA FOUR-WAVE MIXING IN A RESONANT MEDIUM

Thesis by

Joseph Michael Nilsen

In Partial Fulfillment of the Requirements

for the Degree of

Doctor of Philosophy

California Institute of Technology

Pasadena, California

1982

(Submitted April 7, 1982)

to my parents

in memory of Henri Provost

ACKNOWLEDGMENTS

I would like to thank my advisor, Professor Amnon Yariv, for introducing me to the field of phase conjugate optics and for his subsequent outstanding support and guidance during the course of my thesis work at Caltech. I extend thanks to Desmond Armstrong and Larry Begay for their technical advice and invaluable assistance in providing many important components used in my experimental work. Steve Cohen must be thanked for his patience and assistance in filling the many sodium and barium cells which were used in the course of the experiments. I would like to thank Dr. William Bridges and Randy Bartman for the loan of and advice with one of the two dye lasers used in some of the experiments. Thanks also go to Jana Mercado for preparing many of the papers I have published. Very special thanks go to Natalie Gluck, my colleague in the laboratory during all the experimental research conducted on phase conjugation, and a very special friend with whom I have shared many of my most enjoyable experiences at Caltech.

I am very grateful to Dr. Lowell Wood who first aroused my interest in laser physics during the first of several summers I spent doing research at Lawrence Livermore Laboratory. I am thankful to Dr. Jack Marling for teaching me how to operate dye lasers, and to Mr. Donald Duerre for his continual assistance in operating the laser systems I used at LLL. This gave me the experience needed to undertake my experimental thesis research.

The financial support provided by the Fannie and John Hertz Foundation for graduate studies throughout my entire stay at Caltech is most appreciated. For providing the funding necessary to purchase the experimental apparatus and to finance the indispensible computer time, the financial assistance of the Army Research Office, Durham, North Carolina is gratefully acknowledged.

Finally, to my close friends and family go my most sincere gratitude. Special thanks go to John Feldsted, Dimitri Chamieh, and Ann Kramer for their constant support. My parents, most of all, have been a source of constant encouragement to accomplish all that I can. Their support and guidance are most warmly appreciated and have contributed immensely to my reaching this high point in my academic career.

ABSTRACT

This thesis describes the theoretical solution and experimental verification of phase conjugation via nondegenerate four-wave mixing in resonant media. The theoretical work models the resonant medium as a two-level atomic system with the lower state of the system being the ground state of the atom. Working initially with an ensemble of stationary atoms, the density matrix equations are solved by third-order perturbation theory in the presence of the four applied electro-magnetic fields which are assumed to be nearly resonant with the atomic transition. Two of the applied fields are assumed to be non-depleted counterpropagating pump waves while the third wave is an incident signal wave. The fourth wave is the phase conjugate wave which is generated by the interaction of the three previous waves with the nonlinear medium. The solution of the density matrix equations gives the local polarization of the atom. The polarization is used in Maxwell's equations as a source term to solve for the propagation and generation of the signal wave and phase conjugate wave through the nonlinear medium. Studying the dependence of the phase conjugate signal on the various parameters such as frequency, we show how an ultrahigh-Q isotropically sensitive optical filter can be constructed using the phase conjugation process.

In many cases the pump waves may saturate the resonant medium so we also present another solution to the density matrix equations which is correct to all orders in the amplitude of the pump waves since the third-order solution is correct only to first-order in each of the field amplitudes. In the saturated regime, we predict several new phenomena associated with degenerate four-wave mixing and also describe the ac Stark effect and how it modifies the frequency response of the filtering process. We also show how a narrow bandwidth optical filter with an efficiency

greater than unity can be constructed.

In many atomic systems the atoms are moving at significant velocities such that the Doppler linewidth of the system is larger than the homogeneous linewidth. The latter linewidth dominates the response of the ensemble of stationary atoms. To better understand this case the density matrix equations are solved to third-order by perturbation theory for an atom of velocity **v**. The solution for the polarization is then integrated over the velocity distribution of the macroscopic system which is assumed to be a gaussian distribution of velocities since that is an excellent model of many real systems. Using the Doppler broadened system, we explain how a tunable optical filter can be constructed whose bandwidth is limited by the homogeneous linewidth of the atom while the tuning range of the filter extends over the entire Doppler profile.

Since it is a resonant system, sodium vapor is used as the nonlinear medium in our experiments. The relevant properties of sodium are discussed in great detail. In particular, the wavefunctions of the 3S and 3P states are analyzed and a discussion of how the 3S-3P transition models a two- level system is given.

Using sodium as the nonlinear medium we demonstrate an ultrahigh-Q optical filter using phase conjugation via nondegenerate four-wave mixing as the filtering process. The filter has a FWHM bandwidth of 41 MHz and a maximum efficiency of 4×10^{-3}. However, our theoretical work and other experimental work with sodium suggest that an efficient filter with both gain and a narrower bandwidth should be quite feasible.

TABLE OF CONTENTS

Chapter I

INTRODUCTION TO PHASE CONJUGATION VIA FOUR-WAVE MIXING

1.1 Outline of Thesis

In this first chapter, we will discuss the basic concept of phase conjugation via four-wave mixing and the mathematical methods for describing this process by linearizing Maxwell's equations. Some applications of phase conjugation will be presented as well as a description of various materials which are used as nonlinear media in this process.

The second chapter describes phase conjugation via nondegenerate four-wave mixing in a two-level system, with the macroscopic medium consisting of an ensemble of stationary atoms. For this system, the density matrix equations are solved to third order by perturbation theory to determine the polarization which is used as a source term in Maxwell's equations. Taking into consideration only the relevant spatial and temporal Fourier components, Maxwell's equations are linearized to produce a set of coupled mode equations which will be used throughout this thesis. The emphasis in this chapter, as well as in the entire thesis, is on the study of the frequency response of the phase conjugation process as applied to the case of optical filtering.

Generalizing the problem to include an ensemble of atoms with atomic motion, as is commonly encountered in most physical situations, Chapter III presents a solution to the velocity dependent density matrix equations. Supposing that the distribution of velocities is given by a gaussian profile, the macroscopic polarizations are determined by third-order perturbation theory and used in the coupled mode equations to demonstrate the effects that atomic motion has on the phase conjugation process.

Chapter IV extends the perturbation solution of the density matrix equations presented in Chapter II to include all orders in the pump wave amplitudes. This enables us to consider the effect of saturating pump waves on the process and, in particular, to discuss the ac Stark effect and its importance to phase conjugation.

In our experiments, sodium vapor is used as the nonlinear medium. In the fifth chapter, the important characteristics of sodium, both macroscopically and on the atomic level, are explained in great detail. Various drawbacks to using sodium are presented and several alternative materials are mentioned and analyzed.

Chapter VI gives a description of the equipment employed in the experimental research conducted on phase conjugation. In particular, the ring dye laser, which is the critical component in all the experiments, is described in great detail.

The final chapter, Chapter VII, presents a very important series of experiments which demonstrate, for the first time, an ultrahigh-Q optical filter utilizing the phase conjugation process in sodium vapor.

1.2 Introduction

Phase conjugation via four-wave mixing is part of a rather new field called phase conjugate optics, which has attracted a lot of attention because of the way it can be applied to restore severely distorted optical beams to their original, unaberrated condition[1].

First, we will briefly review the work leading up to the present interest in the field[2]. The early work of Zeldovich, Nosach, and colleagues[3,4] demonstated the cancellation of propagation distortion by stimulated Brillouin scattering. Yariv[5,6], independently, proposed and analyzed the use of three-wave mixing in crystals for overcoming image "loss" by modal phase dispersion in multimode fibers and for real-time holography. Four-wave mixing was suggested as an attactive process for phase conjugation by Hellwarth[7], who showed that it overcomes some serious phase

matching problems inherent in three-wave mixing. Yariv and Pepper[8] showed that the four-wave mixing process for phase conjugation is also capable of amplifying an incoming wave, as well as rendering its complex conjugate version and, in the limit of sufficient pumping, of mirrorless oscillation.

The first observations of phase conjugation by four-wave mixing were reported by Jensen and Hellwarth[9] and by Bloom and Bjorklund[10], both of whom used CS_2 as the nonlinear medium. Parametric amplification and oscillation in four-wave mixing was demonstrated by Pepper, Fekete, and Yariv[11] and by Bloom, Liao, and Economou[12]. Avizonis et al[13] demonstated phase conjugation by three-wave mixing in crystals. The ability of the stimulated Brillouin process to restore high spatial frequencies was reported by Wang and Giuliano[14]. Zeldovich and colleagues[15] demonstated optical phase conjugation and image restoration by stimulated Raman scattering.

1.3 Phase Conjugation

To understand what is meant by phase conjugation consider an optical wave of frequency ω moving in the + z direction,

$$E = \mathrm{Re}[\psi(x,y,z)e^{i\omega t}] \tag{1.3-1}$$

where

$$\psi(x,y,z) = A(x,y)e^{-ikz + i\varphi(x,y)} \tag{1.3-2}$$

with A real. The phase conjugate of wave E is defined as

$$\begin{aligned} E_{\text{phase conjugate}} &= \mathrm{Re}[\psi^*(x,y,z)e^{i\omega t}] \\ &= \mathrm{Re}[A(x,y)e^{ikz - i\varphi(x,y)}e^{i\omega t}] \\ &= \mathrm{Re}[A(x,y)e^{-ikz + i\varphi(x,y)}e^{-i\omega t}] \end{aligned} \tag{1.3-3}$$

As the above equations show, a phase conjugate wave is one in which the spatial phase factors are reversed; in other words, the electric field has all its spatial factors conjugated. The result is that the propagation direction of the wave is reversed, with a converging wave now becoming a diverging wave and vice versa. More generally, all the wave fronts are reversed. This process is also equivalent to leaving the spatial part of E unchanged and reversing the sign of t; in this sense, phase conjugation[1] is equivalent to "time reversal."

To better appreciate the consequences of phase conjugation, Fig 1.1 compares reflections of a diverging spherical wave from a conjugate mirror and from an ordinary mirror. The spherical wave strikes an ordinary mirror at an angle ϑ and leaves it at an angle $-\vartheta$ and continues to diverge. For the conjugate mirror the wave strikes the mirror and is converted to a converging wave that retraces the path of the incident wave. To elaborate further, if we take a nice plane wave, send it through a dispersive medium,and phase conjugate it, the phase conjugated wave will travel back through the medium, correct for any aberrations, and come out as a nice plane wave. On the other hand, an ordinary mirror would double the distortion[1].

1.4 Degenerate Four-Wave Mixing

Four-wave mixing is a nonlinear process by which three input waves mix to yield a fourth output wave. The geometry[8] for four-wave mixing is shown in Fig 1.2 . We will assume that all the waves have the same frequency. There are two counter-propagating pump waves A_1 and A_2. We have an input signal wave $A_4^*(0)$ which interacts with A_1 and A_2 in the nonlinear medium to produce a wave A_3 which is proportional to the complex conjugate of A_4. The physical process involved can be thought of as A_4 interacting with A_1 to produce a grating which diffracts A_2. This is shown in Fig 1.3, where we let the angle between $\mathbf{k}_4$ and $\mathbf{k}_1$ equal 30°. This grating formed between the forward pump A_1 and the signal A_4 is called the large-spaced

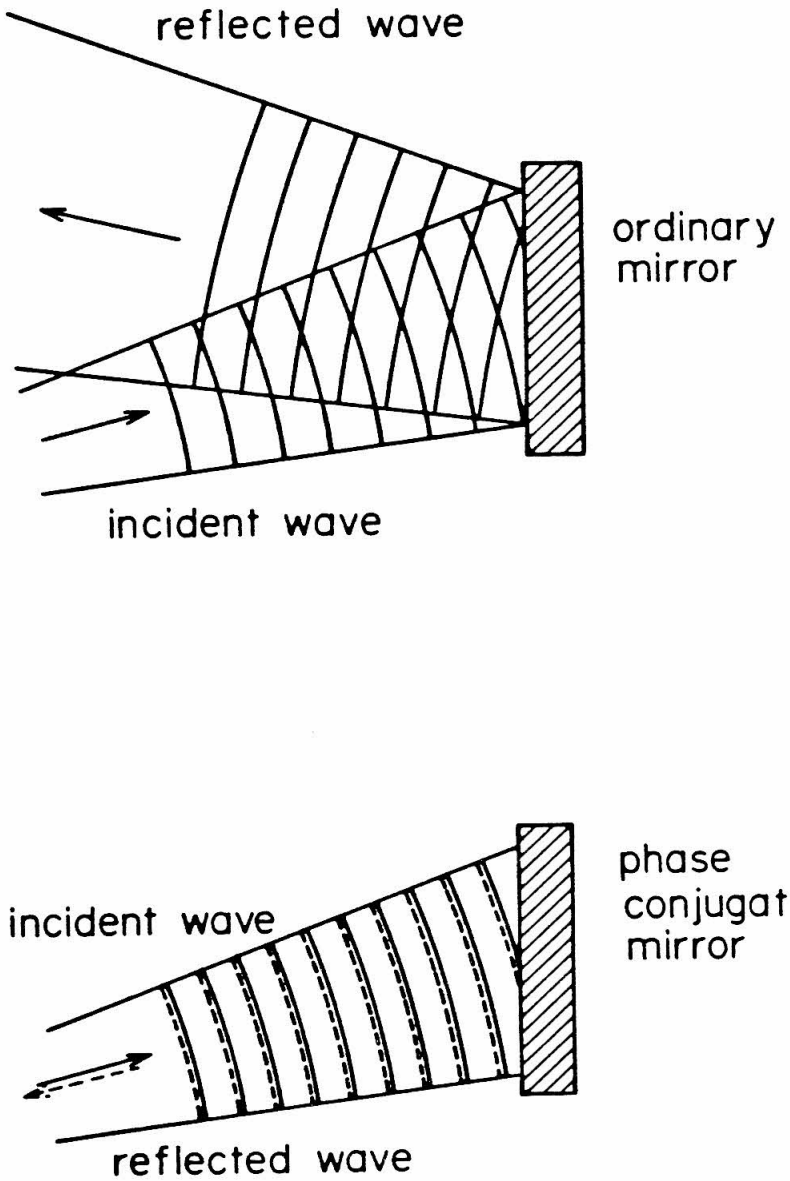

Fig. 1.1 **Comparison of a phase conjugate mirror to an ordinary mirror.**

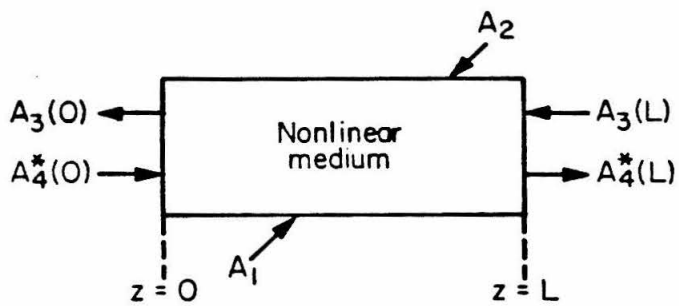

Fig. 1.2 Geometry for nearly degenerate four-wave mixing (assuming nondepleting pump waves)

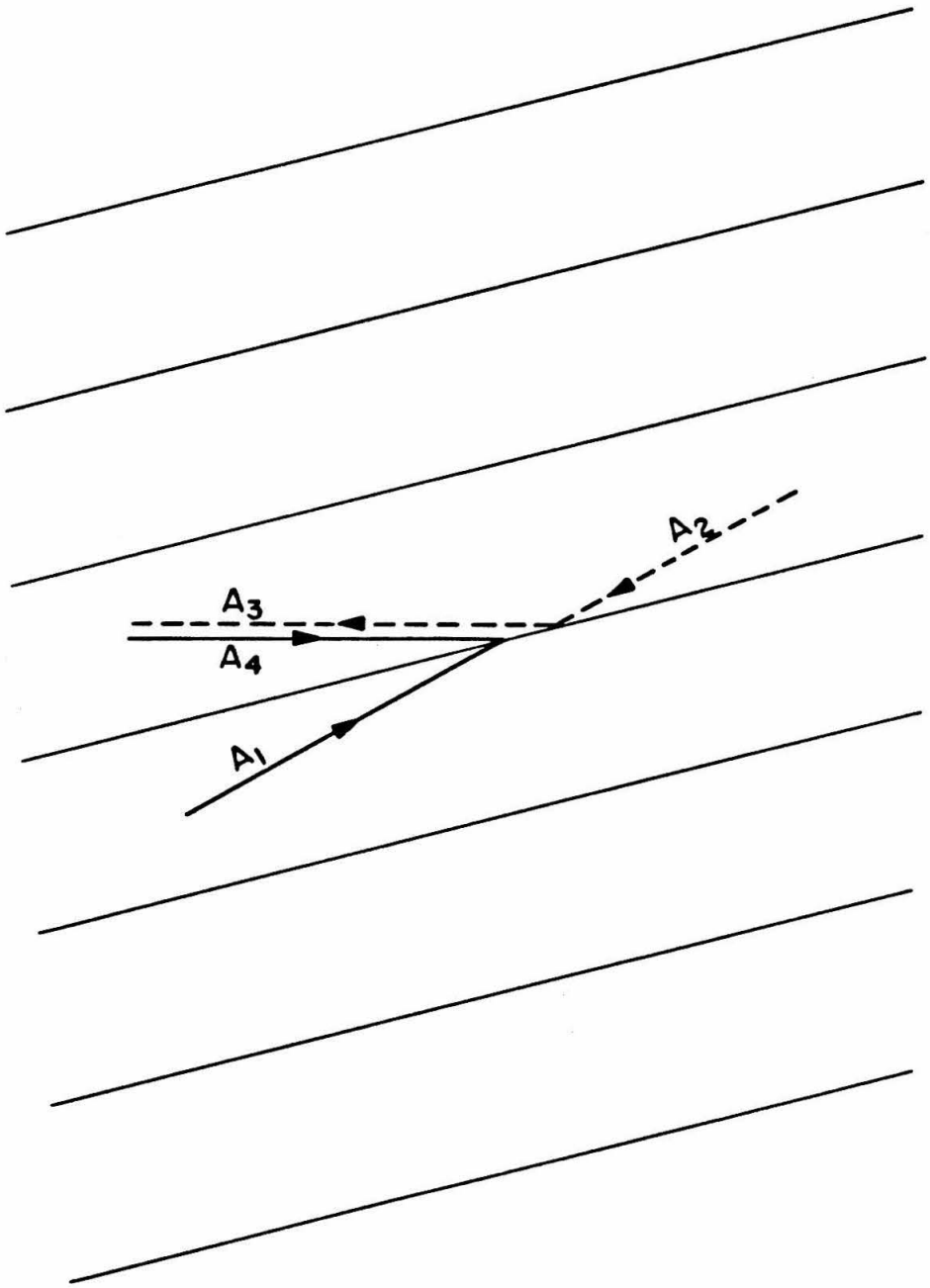

Fig. 1.3 Grating formed by waves A_1 and A_4. A_2 is diffracted off this grating into the direction A_3.

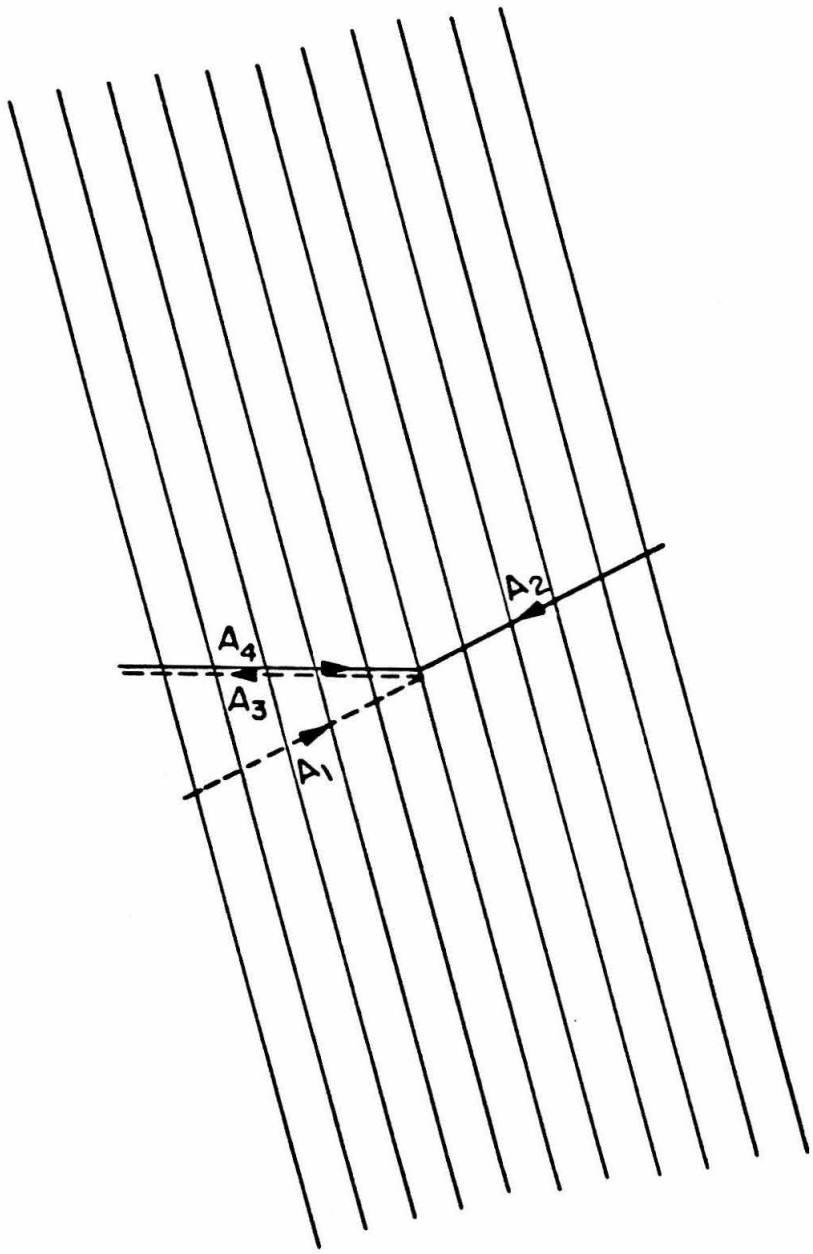

Fig. 1.4 Grating formed by waves A_2 and A_4. A_1 is diffracted off this grating into the direction A_3.

grating. A_4 and A_2 form the other grating, which is shown in Fig 1.4 and is called the small-spaced grating. The separation of the planes in the grating is given by

$$D = \lambda/(2\sin(\Theta/2)) \tag{1.4-1}$$

where Θ is the angle between the two wave vectors forming the grating.

Mathematically, we explain this process by introducing the nonlinear polarization P^{NL} which couples the waves.

$$P^{NL}(\omega_4 = \omega_1 + \omega_2 - \omega_3) = \tfrac{1}{2}\chi^{(3)} A_1 A_2 A_3^* e^{i[\omega_4 t - (\mathbf{k}_1 + \mathbf{k}_2 - \mathbf{k}_3)\cdot \mathbf{r}]}$$

$$P^{NL}(\omega_3 = \omega_1 + \omega_2 - \omega_4) = \tfrac{1}{2}\chi^{(3)} A_1 A_2 A_4^* e^{i[\omega_3 t - (\mathbf{k}_1 + \mathbf{k}_2 - \mathbf{k}_4)\cdot \mathbf{r}]} \tag{1.4-2}$$

The fields are taken as plane waves:

$$E_i(r_i,t) = \tfrac{1}{2}A_i(r_i)\exp[i(\omega_i t - \mathbf{k}_i\cdot\mathbf{r})] + \text{c.c.}, \tag{1.4-3}$$

where r_i is the distance along $\mathbf{k}_i$. In this section, we consider degenerate four-wave mixing, where $\omega_1 = \omega_2 = \omega_3 = \omega_4$. Therefore, we have

$$\mathbf{k}_1 + \mathbf{k}_2 = 0 \qquad \mathbf{k}_3 + \mathbf{k}_4 = 0\,. \tag{1.4-4}$$

We consider a medium with a nonlinear susceptibility $\chi^{(3)}$ and look at the spatial evolution of waves A_3 and A_4 when subject to the pumping by A_1 and A_2.

We apply the standard methods[16] of nonlinear optics to solve the wave equation ($\varepsilon = \mu = 1$)

$$\nabla \times \nabla \times E + \frac{1}{c^2}\frac{\partial^2}{\partial t^2}E = -\frac{4\pi}{c^2}\frac{\partial^2}{\partial t^2}P \tag{1.4-5}$$

and obtain

$$\frac{dA_3}{dz} = i\kappa^* A_4^*$$

$$\frac{dA_4^*}{dz} = i\kappa A_3 \tag{1.4-6}$$

when pump depletion is neglected and the adiabatic approximation

$$\left| \frac{d^2A_i}{dz^2} \right| << \left| k_i \frac{dA_i}{dz} \right| \tag{1.4-7}$$

is used.

The coupling constant κ^* is given by

$$\kappa^* = \frac{2\pi\omega}{cn} \chi^{(3)} A_1 A_2. \tag{1.4-8}$$

Specifying the boundary conditions, $A_3(L)$ and $A_4^*(0)$, of the two signal waves, the solution of Eqs. (1.4-6) is

$$A_3(z) = \frac{\cos|\kappa|z}{\cos|\kappa|L} A_3(L) + i \frac{\kappa^*}{|\kappa|} \frac{\sin|\kappa|(z-L)}{\cos|\kappa|L} A_4^*(0)$$

$$A_4^*(z) = i \frac{|\kappa|}{\kappa^*} \frac{\sin|\kappa|z}{\cos|\kappa|L} A_3(L) + \frac{\cos|\kappa|(z-L)}{\cos|\kappa|L} A_4^*(0). \tag{1.4-9}$$

The most interesting case is that of a single input $A_4^*(0)$ at $z = 0$. In this case the reflected wave at the input is

$$A_3(0) = \frac{-i\kappa^*}{|\kappa|} \tan|\kappa|L \; A_4^*(0) \tag{1.4-10}$$

while at the output,

$$A_4^*(L) = \frac{A_4^*(0)}{\cos|\kappa|L}. \tag{1.4-11}$$

For $|\kappa|L > \pi/4$, we note the reflected wave amplitude exceeds that of the input. The device acts as a reflection amplifier.

When $|\kappa|L = \pi/2$,

$$\frac{A_3(0)}{A_4^*(0)} = \infty \qquad \frac{A_4^*(L)}{A_4^*(0)} = \infty \,, \tag{1.4-12}$$

which corresponds to oscillation. Therefore, gain and oscillation are both possible in the phase conjugation process for large enough pump waves.

1.5 Resonant Medium

We will now consider the case of phase conjugation in a resonant medium. The medium is modeled as a two-level absorbing system and is the representation of the resonant medium that will be used throughout this work. This section is based mainly on the work of Abrams and Lind[17] who did the first calculations for a two-level system. This is presented now in order to show the important differences between a resonant medium and the transparent medium considered in the previous section. In the two-level absorbing system, linear absorption, saturation, and the frequency dependence of the coupling coefficients in the mode equations all need to be considered.

The fields of Eq. (1.4-3) are used with $\omega_i = \omega$ since we are considering the degenerate case. The polarization, including both linear absorption and the nonlinear terms, are calculated from the density matrix equations. Since the solution of the density matrix equations is the main topic of this thesis, we will just present the results of the calculation for now and consider how they are obtained later.

When the first order polarization is included, the coupled mode equations become

$$\frac{dA_3}{dz} = \alpha A_3 + i\kappa^* A_4^*$$

$$\frac{dA_4^*}{dz} = -\alpha^* A_4^* + i\kappa A_3 \qquad (1.5\text{-}1)$$

In these equations, α accounts for the saturated absorption and dispersion of fields A_3 and A_4^* and is given by

$$\alpha = \alpha_0 \frac{1 - i\delta}{(1+\delta^2)^{1/2}} \frac{1 + \delta^2 + 2I}{(1 + \delta^2 + 4I)^{3/2}} \equiv \alpha_R - i\alpha_I \qquad (1.5\text{-}2)$$

The coupling coefficient κ^* is given by

$$\kappa^* = i\alpha_0 \frac{1 - i\delta}{(1 + \delta^2)^{1/2}} \frac{2I}{(1 + \delta^2 + 4I)^{3/2}} \tag{1.5-3}$$

where I is the normalized pump intensity which is defined as

$$I = \frac{A_1 A_1^*}{E_s^2} = \frac{A_2 A_2^*}{E_s^2}, \tag{1.5-4}$$

assuming equal intensity pump waves. E_s^2 is the line-center saturation intensity, α_0 is the line center small signal field attenuation coefficient, and $\delta = (\omega - \omega_0)T_2$ is the normalized detuning of the fields from line center with T_2 the transverse relaxation time[16].

Using the boundary conditions $A_3(L)$ and $A_4^*(0)$, the solutions for Eqs. (1.5-1) are

$$A_3(z) = \frac{w\cos wz + \alpha_R \sin wz}{w\cos wL + \alpha_R \sin wL} e^{-i\alpha_I(z-L)} A_3(L) + \frac{i\kappa^* \sin w(z-L)}{w\cos wL + \alpha_R \sin wL} e^{-i\alpha_I z} A_4^*(0)$$

$$A_4^*(z) = \frac{i\kappa \sin wz}{w\cos wL + \alpha_R \sin wL} e^{-i\alpha_I z} A_4(L) + \frac{w\cos w(z-L) - \alpha_R \sin w(z-L)}{w\cos wL + \alpha_R \sin wL} e^{-i\alpha_I z} A_4^*(0) \tag{1.5-5}$$

where $w = (|\kappa|^2 - \alpha_R^2)^{1/2}$.

We consider the case of a single input $A_4^*(0)$, which is the boundary condition used in the filter case. The reflection coefficient R is

$$R = \frac{|\kappa \sin wL|^2}{|w\cos wL + \alpha_R \sin wL|^2} \tag{1.5-6}$$

For w real, $|\kappa|^2 > \alpha_R^2$, the oscillation condition is

$$\tan wL = \frac{-w}{\alpha_R}. \tag{1.5-7}$$

If the medium is an absorbing medium, $\alpha_0 > 0$, then oscillation occurs for $wL > \pi/2$. If $\alpha_0 < 0$, the case of gain, then the oscillation condition requires

$wL < \pi/2$. For the transparent medium discussed in the previous section, $\alpha_0 = 0$, and oscillation occurs when $wL = |\kappa|L = \pi/2$. When $|\kappa|^2 < \alpha_R^2$, which corresponds to w being imaginary, the oscillation condition is given by

$$\tanh|wL| = \frac{-|w|}{\alpha_R}. \qquad (1.5\text{-}8)$$

In this case oscillation can occur only if there is gain, $\alpha_0 < 0$.

1.6 Applications of Phase Conjugation

The main property of phase conjugators is their ability to restore severely aberrated waves to their original state on passing through a distorting medium twice. Now we will consider some of the applications this property can be used for. Much of this section is drawn from several excellent review articles by Yariv[2] and Giuliano[1].

One application, motivated by the laser fusion work done at LASL, is to utilize the properties of phase conjugation to deliver the maximum possible energy onto the target pellet used in the fusion experiments. This scheme involves first illuminating the target with a pulsed laser of a wavelength compatible with the amplifiers of the system. Some of the light reflected off the target will be captured in the aperture of the focusing element and will enter the optical system. The next step is amplification of the distorted reference wave followed by conjugation of the wave. The conjugated wave is then amplified a second time and propagates back through the optical elements. The phase distortions accumulated on the first pass are eliminated as the wave makes a second pass through the system. The net result is the delivery of an intense, diffraction limited, pulse of light to the target. In laser fusion, the problem of beam alignment, pointing, and focusing is extremely complex in the conventional technology, demanding that the target be precisely located within a narrowly defined field of view and requiring sophisticated sensor/servo systems. The great advantage of the phase conjugate scheme is, that once the refer-

ence is created, everything else happens automatically[1].

A similar application applies to sending laser energy through the atmosphere. In conventional adaptive optics, one measures the atmospheric turbulence along the propagation path using a probe beam that originates at the target. The probe signal is received at the aperture of the laser transmitter. The aperture is divided into subapertures. The local wavefront tilt is measured using shearing interferometers or some similar technique. This information is used to drive actuators on a deformable mirror. The deformable mirrors are then used to predistort the outgoing beam in a way that compensates exactly for the atmospheric distortions to be encountered along the propagation path to the target. In the phase conjugate case the probe beam is amplified, conjugated, and retransmitted. One big advantage of the nonlinear approach over the conventional one is that compensation will still occur even if the probe beam has substantial amplitude variation over the wavefront, as in the case of severe turbulence. The conventional approach compensates only for phase variations. It should be noted that neither approach can compensate for absorption of the laser energy or time varying changes in the distorting medium if the changes occur on a time scale shorter then the time it takes the phase conjugate wave to retrace the path of the probe beam[1].

Another potentially valuable application for phase conjugate optics is the use of a phase conjugator as a mirror in an optical resonator. Several papers have discussed the idea of replacing one of the conventional mirrors[18-22] by a phase conjugate mirror. This has been demonstrated by Pepper and colleagues[20]. Phase conjugate resonators are expected to exhibit several unique properties . The property that Pepper and coworkers demonstrated was its ability to compensate for intracavity distortion. They also showed that light extracted from the end of the resonator with a conventional mirror has a transverse phase which depends only on the output mirror's radius of curvature and not on any distortions within the body of the

resonator. A second important property of this resonator is that it does not possess longitudinal modes that depend on the cavity length. Usually an optical resonator has longitudinal modes separated in frequency by $c/2L$, where L is the cavity length. This is due to the requirement that the accumulated phase after one round trip of the cavity equals 2π times an integer, so that waves will constructively interfere with themselves. In a phase conjugate resonator the phase that is accumulated as the wave propagates from the conventional mirror to the conjugate mirror is subtracted by the same amount on the way back to the conventional mirror, so the net phase which is accumulated is always zero. The phase conjugate resonator can therefore support any wavelength which is within the bandwidth of the gain medium and of the phase conjugate mirror. In addition the problem of mode hopping due to cavity length drift can be eliminated.

It has also been shown[23] that the fundamental oscillation mode of a resonator with a phase conjugate mirror has extremely low losses compared with the corresponding oscillation modes of similarly filled resonators of the same geometric dimensions but formed by conventional mirrors.

Another application suggested by the group at Caltech[24,25] was to use phase conjugation to do spatial convolution and correlation. This involves placing the nonlinear medium at the focal plane of a set of lenses which are used to obtain the Fourier transform of the pump and signal waves. The medium is used to do a multiplication of the Fourier transforms of the waves. By choosing pump wave A_1 to be a point source and placing spatial information on waves A_2 and A_4, we can obtain a correlation between these two fields. We obtain the spatial convolution of A_1 and A_2 by taking A_4 as a point source. This approach makes possible autocorrelation and autoconvolution as well as other high-speed, real-time information processing.

Photolithography is another area of potential application of phase conjugation.

Photolithography involves projecting complex patterns onto photo-resist layers. This is usually accomplished using conventional optical techniques which require diffraction limited, low f-number performance. In the phase conjugate approach the mask is illuminated from the back by a laser. The image is formed on the photoresist surface of a substrate, after being reflected from the conjugator by way of a beam splitter. The advantage of this scheme is that diffraction limited performance can be achieved without using expensive optical components. In addition this approach achieves the same goal as contact photolithography, without placing the mask in direct contact with the sample. Projection of high-quality images using this technique has recently been demonstrated[26].

A more esoteric application of phase conjugation suggested by Yuen and Shapiro[27] is the generation of photons in a two-photon coherent state by using proper combinations of the phase conjugate wave with the incident signal wave. They have shown theoretically that two-photon coherent states are minimum uncertainty states[28] with unequal uncertainties in the two field quadratures. The uncertainty in one of the field quadratures can be arbitrarily reduced at the expense of the other quadrature. In optical systems, homodyne detection[29] can measure one of these field quadratures.

An application suggested by Shapiro[30] is its use as an optical waveguide tap with infinitesimal insertion loss. The novel statistics of the two-photon coherent state make possible high signal to noise detection from a directional coupler that is very weakly linked to an information bearing optical waveguide. Carlton Caves[31] of the gravitation group at Caltech has suggested using these states to increase the sensitivity of the interferometers which are proposed as gravitational wave detectors.

Optical filtering via phase conjugation is the application which is the main topic of this thesis. To construct an optical filter, the pump waves, A_1 and A_2, are provided

by one laser at frequency ω. The signal wave $A_4^*(0)$ at frequency ω_4 is the input to the filter. The output of the filter is the phase conjugate wave $A_3(0)$ whose amplitude depends on the relative detuning of ω_4 from ω. The phase conjugate property is used to provide a high signal to noise ratio for the filter.

Using a resonant medium as the nonlinear medium, we discuss the properties of optical filtering in both homogeneous[32] and inhomogeneous media[33,34] and then demonstrate an ultrahigh-Q optical filter[35] which uses sodium vapor as the medium. The bandwidth of the filter depends on the homogeneous linewidth of the resonant medium. Other authors[36,37] have discussed optical filtering via phase conjugation in a transparent medium. In that case the filtering depends on phase mismatching between the various waves and typically does not achieve the narrow bandwidth of the resonant medium.

1.7 Materials used as Nonlinear Media

Now we will look at a few of the materials people have used to generate phase conjugated waves via four-wave mixing. As previously mentioned, the first observation of phase conjugation was by Jensen and Hellwarth[9] of USC. They observed a reflectivity $R \approx 10\%$ in CS_2 using a Q-switched ruby laser. In a second experiment they demonstrated phase conjugation in a dielectric waveguide[38] filled with CS_2.

At Caltech, Pepper, Fekete, and Yariv[11] used a Q-switched ruby laser to measure $\chi^{(3)}$ for CS_2. They observed amplification and even oscillation at a pump intensity of 8.8 MW/cm^2. John AuYeung[39] observed a backward wave conversion efficiency of 0.45% using a pump power of only 6mW in a 4μm i.d. CS_2 filled optical fiber. This was done using an argon laser at 5145Å.

At Bell Laboratories, Dave Bloom and co-workers have worked with a variety of materials. They observed phase conjugation in CS_2 using a Q-switched, frequency doubled, Nd:Yag laser[10]. In ruby[40], they used a CW argon laser to observe a

$R \approx 2 \times 10^{-3}$ with a pump intensity of only $95 W/cm^2$. Ruby can be modeled as a three level system with a broad band absorption and a large $\chi^{(3)}$. With sodium[12] as the medium, they used a nitrogen laser-pumped dye laser which was detuned $1.25\ cm^{-1}$ from the D_1 line of Na to obtain signal gains up to 100. In the CW case[41], they used a single mode dye laser and observed $R \approx 2 \times 10^{-3}$ with pump power of only $600\ mW/cm^2$.

At LASL, Fischer and group have done some very interesting intracavity four-wave mixing. In the first case, they demonstrated phase conjugation in germanium[42] by inserting the output mirror of a CO_2 laser backwards into the laser cavity so that the germanium substrate was intracavity. The pump waves were the standing waves of the laser cavity and the signal wave was a small part of the output of the laser. The intracavity experiment has the advantage in that this guarantees counterpropagating pump waves if the laser is lasing. In subsequent experiments[43], they used the CO_2 lasing medium as the nonlinear material and obtained 2% reflectivity.

At Hughes Aircraft Research Laboratories, Lind and group[44] have demonstrated reflectivities of 7% in a few torr of SF_6 using a CO_2 laser. They have also used a Q-switched Nd:Yag laser to obtain R as high as 180 in silicon[45].

These are just a few of the materials which were first used to demonstrate phase conjugation via four-wave mixing. Many other materials, such as lithium–niobate[13], organic dyes[46–49], ammonia[50], barium titanate[51], and $Bi_{12}SiO_{20}$ crystals[52], just to name a few, have also been used.

1.8 Conclusion

In this chapter we have presented the basic concepts of phase conjugation along with the mathematical formulation used to describe the process. We have considered both a transparent medium and a resonant medium as possible nonlinear media. Several applications of phase conjugation were presented. Finally, various

materials used as the nonlinear medium have been presented.

References for Chapter I

1. C. R. Giuliano, "Applications of optical phase conjugation," Phys. Today 34,27 (1981).

2. Amnon Yariv, 'Phase conjugate optics and real-time holography," IEEE J. Quantum Electron. QE-14,650 (1978).

3. B. Y. Zeldovich, V. I. Popovichev, V. V. Ragulskii, and F. S. Faisullov, 'Connection between the wave fronts of the reflected and exciting light in stimulated Mandel'shtam-Brillouin scattering," Sov. Phys. JETP 15,109 (1972).

4. O. Y. Nosach, V. I. Popovichev, V. V. Ragulskii, and F. S. Faisullov, 'Cancellation of phase distortions in an amplifying medium with a 'Brillouin Mirror"," Sov. Phys. JETP Lett. 16,435 (1972).

5. A. Yariv, 'Three-dimensional pictorial transmission in optical fibers," Appl. Phys. Lett. 28,88 (1976).

6. A. Yariv, 'On transmission and recovery of three-dimensional image information in optical waveguides," J. Opt. Soc. Am. 66,301 (1976).

7. R. W. Hellwarth, 'Generation of time reversal wavefronts by nonlinear refraction," J. Opt. Soc. Am. 67,1 (1977).

8. A. Yariv and D. M. Pepper, "Amplified reflection, phase conjugation, and oscillation in degenerate four-wave mixing," Opt. Lett. 1,16 (1977).

9. S. L. Jensen and R. W. Hellwarth, 'Observation of the time-reversed replica of a monochromatic optical wave," Appl. Phys. Lett. 32,166 (1978).

10. D. M. Bloom and G. E. Bjorklund, 'Conjugate wave front generation and image reconstruction by four-wave mixing," Appl. Phys. Lett. 31,592 (1977).

11. D. M. Pepper, D. Fekete, and A. Yariv, 'Observation of amplified phase-conjugate

reflection and optical parametric oscillation by degenerate four-wave mixing in a transparent medium," Appl. Phys. Lett. 33,41 (1978).

12. D. M. Bloom, P. F. Liao, and N. P. Economu, "Observation of amplified reflection by degenerate four-wave mixing in atomic sodium vapor," Opt. Lett. 2,58 (1978).

13. P. V. Avizonis, F. A. Hopf, W. D. Bamberger, S. F. Jacobs, A. Tomita, and K. H. Womack, "Optical phase conjugation in a lithium-niobate crystal," Appl. Phys. Lett. 31,435 (1977).

14. V. Wang and C. R. Giuliano, "Correction of phase aberrations via stimulated Brillouin scattering," Opt. Lett. 2,4 (1978).

15. B. Ya. Zeldovich and V. V. Shkunov, "Wavefront reproduction in stimulated Raman scattering," Sov. J. Quantum Electron. 7,610 (1977).

16. A. Yariv, **Quantum Electronics** (Wiley, New York, 1975), pp. 149-155, 418-421, 553-558.

17. R. L. Abrams and R. C. Lind, "Degenerate four-wave mixing in absorbing media," Opt. Lett. 2,94 (1978).

18. I. M. Bel'dyugin, M. G. Galushkin, and E. M. Zemskov, "Properties of resonators with wavefront-reversing mirrors," Sov. J. Quantum Electron. 9,20 (1979).

19. J. F. Lam and W. P. Brown, "Optical resonators with phase-conjugate mirrors," Opt. Lett. 5,61 (1980).

20. J. AuYeung, D. Fekete, D. M. Pepper, and A. Yariv, "A theoretical and experimental investigation of the modes of optical resonators with phase-conjugate mirrors," IEEE J. Quantum Electron. QE-15,1180 (1979).

21. P. A. Belanger, A. Hardy, and A. E. Siegman, "Resonant modes of optical cavities with phase-conjugate mirrors," Appl. Opt. 19,602 (1980).

22. P. A. Belanger, A. Hardy, and A. E. Siegman, "Resonant modes of optical cavities with phase conjugate mirrors: higher-order modes," Appl. Opt. 19,479 (1980).

23. M. G. Reznikov and A. I. Khizhnyak, "Properties of a resonator with a wavefront-reversing mirror," Sov. J. Quantum Electron. 10,633 (1980).

24. David M. Pepper, John AuYeung, Dan Fekete, and Amnon Yariv, "Spatial convolution and correlation of optical fields via degenerate four-wave mixing," Opt. Lett. 3,7 (1978).

25. Jeffrey O. White and Amnon Yariv, "Real-time image processing via four-wave mixing in a photorefractive medium," Appl. Phys. Lett. 37,5 (1980).

26. M. D. Levenson, "High-resolution imaging by wave-front conjugation," Opt. Lett. 5,182 (1980).

27. Horace P. Yuen and Jeffrey H. Shapiro, "Generation and detection of two-photon coherent states in degenerate four-wave mixing," Opt. Lett. 4,334 (1979).

28. H. P. Yuen and J. H. Shapiro, "Optical communication with two-photon coherent states-Part I: Quantum-state propagation and quantum-noise reduction," IEEE Trans. Inform. Theory IT-24,657 (1978).

29. J. H. Shapiro, H. P. Yuen, and J. A. M. Mata, "Optical communication with two-photon coherent states-Part II: Photoemissive detection and structured receiver performance," IEEE Trans. Inform. Theory IT-25,179 (1979).

30. Jeffrey H. Shapiro, "Optical waveguide tap with infinitesimal insertion loss," Opt. Lett. 5,351 (1980).

31. Carlton M. Caves, "Quantum-mechanical noise in an interferometer," Phys. Rev. D23,1693 (1981).

32. J. Nilsen and A. Yariv, "Nearly degenerate four-wave mixing applied to optical filters," Appl. Opt. 18,143 (1979).

33. J. Nilsen and A. Yariv, "Nondegenerate four-wave mixing in a Doppler-broadened resonant medium," J.Opt.Soc.Am. 71,180 (1981).

34. Joseph Nilsen and Amnon Yariv, "A tunable narrowband optical filter via phase conjugation by nondegenerate four-wave mixing in a Doppler-broadened resonant medium," Opt. Comm. 39,199 (1981).

35. J. Nilsen, N. S. Gluck, and A. Yariv, "Narrowband optical filter via phase conjugation by nondegenerate four-wave mixing in sodium vapor," Opt. Lett. 6,380 (1981).

36. D. M. Pepper and R. L. Abrams, "Narrow optical bandpass filter via nearly degenerate four-wave mixing," Opt. Lett. 3,212 (1978).

37. N. F. Pilipetsky and V. V. Shkunov, "Narrowband four-wave reflecting filter with frequency and angular tuning," Opt. Comm. 37,217 (1981).

38. S. M. Jensen and R. W. Hellwarth, "Generation of time-reversed waves by nonlinear refraction in a waveguide," Appl. Phys. Lett. 33,404 (1978).

39. J. AuYeung, D. Fekete, D. M. Pepper, A. Yariv, and R. K. Jain, "Continuous backward-wave generation by degenerate four-wave mixing in optical fibers," Opt. Lett. 4,42 (1979).

40. P. F. Liao and D. M. Bloom, "Continuous-wave backward-wave generation by degenerate four-wave mixing in ruby," Opt. Lett. 3,4 (1978).

41. P. F. Liao, D. M. Bloom, and N. P. Economou, "CW optical wave-front conjugtion by saturated absorption in atomic sodium vapor," Appl. Phys. Lett. 32,813 (1978)

42. E. E. Bergmann, I. J. Bigio, B. J. Feldman, and R. A. Fisher, "High-efficiency pulsed 10.6-μm phase-conjugate reflection via degenerate four-wave mixing," Opt. Lett. 3,82 (1978).

43. R. A. Fisher and B. J. Feldman, "On-resonant phase-conjugate reflection and amplification at 10.6μm in inverted CO_2," Opt. Lett. 4,140 (1979).

44. R. C. Lind, D. G. Steel, M. B. Klein, R. L. Abrams, C. R. Giuliano, and R. K. Jain, "Phase conjugation at 10.6μm by resonantly enhanced degenerate four-wave mixing," Appl. Phys. Lett. 34,457 (1979).

45. R. K. Jain, M. B. Klein, and R. C. Lind, "High-efficiency degenerate four-wave mixing of 1.06–μm radiation in silicon," Opt. Lett. 4,328 (1979).

46. Wu Cun-Kai, Fan Jun-Yin, and Wang Zhi-Ying, "Investigation of degenerate four-wave mixing and phase conjugation in organic dye solutions,"Acta Phys. Sin. 30,189 (1981).

47. Wu Cun-Kai, Cui Yang-zhao, and Wang Zhi-Ying, "Degenerate four-wave mixing and phase conjugation in organic dye solutions," Acta. Phys. Sin. 29,937 (1980).

48. J. O. Tocho, W. Sibbett, and D. J. Bradley, "Picosecond phase-conjugate reflection from organic dye saturable absorbers," Opt. Comm. 34,122 (1980).

49. C. K. Wu, J. Y. Fan, and Z. Y. Wang, "Investigation of degenerate 4-wave mixing and phase conjugation in organic-dye solutions, J. Opt. Soc. Am. 70,601 (1980).

50. A. Elci, D. Rogovin, D. Depatie, and D. Haueisen, "Phase conjugation in ammonia," J. Opt. Soc. Am. 70, 990 (1980).

51. J. Feinberg, D. Heiman, A.R. Tanguay Jr., and R. W. Hellwarth, "Photorefractive effects and light-induced charge migration in barium titanate," J. Appl. Phys., 51,1296 (1980).

52. J. P. Huignard, J. P. Herriau, G. Rivet, and P. Gunter, "Phase-conjugation and spatial-frequency dependence of wave-front reflectivity in $Bi_{12}SiO_{20}$ crystals," Opt. Lett. 5,102 (1980).

Chapter II

NONDEGENERATE FOUR-WAVE MIXING IN A HOMOGENEOUSLY BROADENED TWO-LEVEL SYSTEM

2.1 Introduction

In the first chapter we discussed the basic properties of the phase conjugation process as they affect a wave which is incident on a phase conjugator and the properties of the subsequent phase conjugate wave. We gave examples of various applications of phase conjugation and examined different types of media which are used to do the nonlinear mixing which generates the phase conjugate wave.

Applying the standard methods of nonlinear optics, we will consider phase conjugation via four-wave mixing in a nonlinear medium using a plane wave coupled-mode treatment. The nonlinear medium used throughout most of this work will be a two-level system. The coupled-mode equations for the conjugation process will include both the linear loss and the nonlinear coupling between the waves.

This chapter will study nondegenerate four-wave mixing[1] in a homogeneously broadened two-level system. First we will describe the two-level system, then present the density matrix solutions for a particular choice of the applied electromagnetic fields and use these in the coupled- mode equations to solve for the phase conjugate signal.

2.2 Density Matrix Equations for a Two-Level System

The nonlinear medium is modeled as an ensemble of stationary atoms. As shown in Fig. 2.1, we assume the atoms have only two energy levels, E_1 and E_2 with energy splitting $\hbar\omega_0$, which are involved in the nonlinear interaction. The angular frequencies of the electromagnetic fields are assumed to be nearly resonant only with these

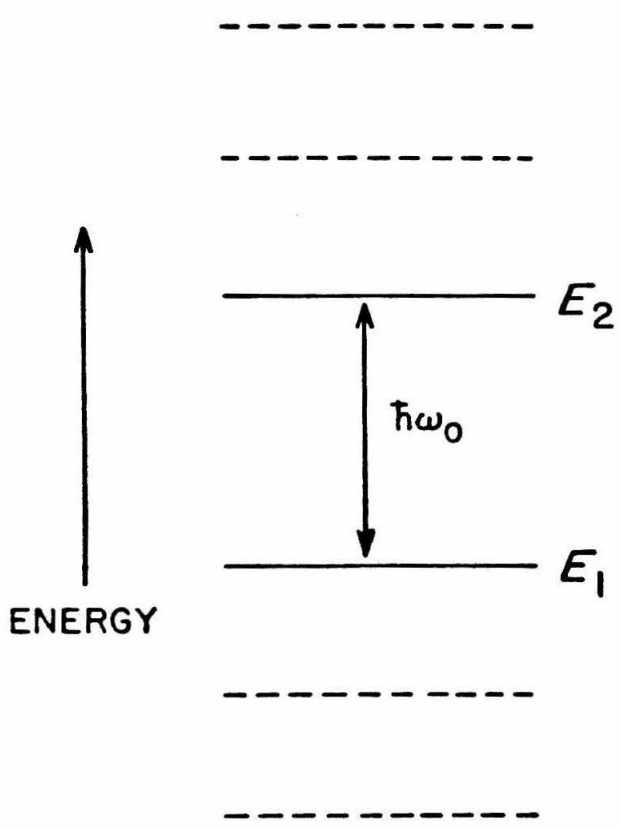

Fig. 2.1 Energy levels of the two-level system

two energy levels.

The Hamiltonian of the two-level system is

$$H = H_0 + H' \tag{2.2-1}$$

where H_0 is the Hamiltonian of the system in the absence of any field. The interaction Hamiltonian H' is assumed to be of the dipole type

$$H' = -\hat{\mu}E(\mathbf{r},t) \tag{2.2-2}$$

where $\hat{\mu}$ is the component of the dipole operator along the direction of the electric field $E(\mathbf{r},t)$. The electric field $E(\mathbf{r},t)$ will be considered as a classical variable.

The total wavefunction of the system is

$$\Psi = c_1(\mathbf{r},t)\,\psi_1 + c_2(\mathbf{r},t)\,\psi_2 \tag{2.2-3}$$

where ψ_n are eigenfunctions of the unperturbed Hamiltonian H_0 such that

$$H_0\psi_1 = E_1\psi_1$$

$$H_0\psi_2 = E_2\psi_2 \tag{2.2-4}$$

The functions $c_1(\mathbf{r},t)$ and $c_2(\mathbf{r},t)$ represent the amplitude for the atom to be located at position $\mathbf{r}$ at time t and occupy energy levels E_1 and E_2, respectively. The Schrodinger equation is given by

$$i\hbar\frac{\partial\Psi}{\partial t} = H\Psi \tag{2.2-5}$$

Using the eigenfunctions ψ_1 and ψ_2 as a basis, the density matrix operator ρ can be represented as a 2×2 matrix with elements $\rho_{11}, \rho_{12}, \rho_{21}, \rho_{22}$. The components of the matrix ρ are shown below.

$$\rho = \begin{pmatrix} c_1c_1^* & c_1c_2^* \\ c_2c_1^* & c_2c_2^* \end{pmatrix} \tag{2.2-6}$$

The density matrix equation, which is equivalent to the Schrodinger equation, is

given by

$$i\hbar \frac{\partial \rho}{\partial t} = [\, H, \rho \,]. \tag{2.2-7}$$

In this basis the unperturbed Hamiltonian is

$$H_0 = \begin{pmatrix} E_1 & 0 \\ 0 & E_2 \end{pmatrix}. \tag{2.2-8}$$

The diagonal matrix elements of H' are taken as zero

$$\langle \psi_1 | \hat{\mu} | \psi_1 \rangle = \langle \psi_2 | \hat{\mu} | \psi_2 \rangle = 0 \tag{2.2-9}$$

as appropriate to transitions between states of definite parity. The phases of the off diagonal elements of H' are taken such that

$$\langle \psi_1 | \hat{\mu} | \psi_2 \rangle = \langle \psi_2 | \hat{\mu} | \psi_1 \rangle \equiv \mu. \tag{2.2-10}$$

The density matrix equations can be written as

$$\begin{aligned} \frac{d\rho_{21}}{dt} &= -i\omega_0 \rho_{21} + i\frac{\mu}{\hbar} E(\mathbf{r},t)\,(\rho_{11} - \rho_{22}) \\ \frac{d}{dt}(\rho_{11} - \rho_{22}) &= 2i\frac{\mu}{\hbar} E(\mathbf{r},t)\,(\rho_{21} - \rho_{21}^{*}) \end{aligned} \tag{2.2-11}$$

where $\rho_{11} + \rho_{22} = 1$ is the normalization condition.

We will incorporate the loss of phase coherence due to collisions as well as the natural lifetime of the atoms into the density matrix formalism by including the phenomological relaxation times T_1 and T_2 in the density matrix equations[2]. The resulting equations are

$$\begin{aligned} \frac{d\rho_{21}}{dt} &= -i\omega_0 \rho_{21} + i\frac{\mu}{\hbar} E(\mathbf{r},t)\,(\rho_{11} - \rho_{22}) - \frac{\rho_{21}}{T_2} \\ \frac{d}{dt}(\rho_{11} - \rho_{22}) &= 2i\frac{\mu}{\hbar} E(\mathbf{r},t)\,(\rho_{21} - \rho_{21}^{*}) - \frac{(\rho_{11} - \rho_{22}) - (\rho_{11} - \rho_{22})_0}{T_1} \end{aligned} \tag{2.2-12}$$

where $(\rho_{11} - \rho_{22})_0$ is the equilibrium value of $(\rho_{11} - \rho_{22})$ in the absence of the applied

field $E(r,t)$.

2.3 Solving the Density Matrix Equations by Perturbation Theory

In the phase conjugation problem, which is the subject of this work, the mixing involves two intense counterpropagating pump waves E_1 and E_2 of the same frequency ω and two weak counterpropagating waves E_3 and E_4 with frequencies ω_3 and ω_4. The geometry of Yariv and Pepper[3] shown in Fig. 2.2 is used.

The fields are taken as plane waves:

$$E_i(r_i,t) = \tfrac{1}{2}A_i(r_i)\exp[i(\omega_i t - \mathbf{k}_i\cdot\mathbf{r})] + \text{c.c.}, \tag{2.3-1}$$

where r_i is the distance along $\mathbf{k}_i$. We have

$$\mathbf{k}_1 + \mathbf{k}_2 = 0, \qquad \omega_3 + \omega_4 = 2\omega. \tag{2.3-2}$$

The applied electric fields are polarized along the same direction. The density matrix equations are now solved to third-order by pertubation theory.

To use perturbation theory[2], we first expand the density matrix equations as

$$\rho_{ij} = \rho_{ij}^{(0)} + \lambda\rho_{ij}^{(1)} + \lambda^2\rho_{ij}^{(2)} . \tag{2.3-3}$$

Then we solve for ρ_{ij} by iteration up to some desired order, third-order in our case, and then put $\lambda = 1$ in the final results. In Eqs. (2.2-12) we replace H' by λ H' and equate the same powers of λ on both sides of the equation to obtain

$$\frac{\partial\rho_{ij}^{(n)}}{\partial t} = -(i\omega_{ij} + \gamma_{ij})\rho_{ij}^{(n)} - \frac{i}{\hbar}[\, H' \,,\, \rho^{(n-1)} \,]_{ij} \tag{2.3-4}$$

where

$$\gamma_{12} = \gamma_{21} = 1/T_2 \qquad \gamma_{11} = \gamma_{22} = 1/T_1 . \tag{2.3-5}$$

The solution is

$$\rho_{ij}^{(n)}(t) = \frac{-i}{\hbar}\int_{-\infty}^{t} e^{i(\omega_{ij} - i\gamma_{ij})(s-t)}\,[\, H'(s) \,,\, \rho^{(n-1)}(s) \,]_{ij}\, ds .$$

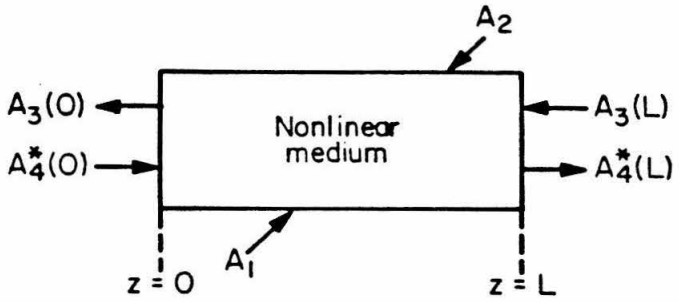

Fig. 2.2 Geometry for nearly degenerate four-wave mixing (assuming nondepleting pump waves)

(2.3-6)

To zero order we assume

$$\rho_{12}^{(0)} = 0 = \rho_{21}^{(0)} \tag{2.3-7}$$

and $(\rho_{11} - \rho_{22})_0$ the equilibrium value of $\rho_{11} - \rho_{22}$ for zero applied field.

To obtain the first order solutions, we calculate $[\, H' \,,\, \rho^{(0)} \,]_{ij}$. The components of the commutator are given by

$$[\, H' \,,\, \rho^{(0)} \,]_{11} = 0 \qquad [\, H' \,,\, \rho^{(0)} \,]_{11} = 0$$

and

$$[\, H' \,,\, \rho^{(0)} \,]_{12} = \mu(\rho_{11} - \rho_{22})_0 \, E(\mathbf{r},t) \tag{2.3-8}$$

Using these commutators in Eqs. (2.3-6) and neglecting the nonresonant denominators, we obtain

$$\rho_{12}^{(1)} = \frac{-\mu}{2\hbar}(\rho_{11} - \rho_{22})_0 \left[A_1 \frac{e^{i(\omega t - \mathbf{k}_1 \cdot \mathbf{r})}}{(\omega - \omega_0 - i/T_2)} + A_2 \frac{e^{i(\omega t - \mathbf{k}_2 \cdot \mathbf{r})}}{(\omega - \omega_0 - i/T_2)} \right.$$

$$\left. + A_3 \frac{e^{i(\omega_3 t - \mathbf{k}_3 \cdot \mathbf{r})}}{(\omega_3 - \omega_0 - i/T_2)} + A_4 \frac{e^{i(\omega_4 t - \mathbf{k}_4 \cdot \mathbf{r})}}{(\omega_4 - \omega_0 - i/T_2)} \right] \tag{2.3-9}$$

Using the same procedure, first calculating the commutators and substituting these in Eqs. (2.3-6), we can calculate the higher order terms. We have done the perturbation solutions out to third-order.

The macroscopic polarization is given by $P = N\mu(\rho_{12} + \rho_{21})$. N is the density of atoms. The solutions for the polarizations are

$$P(\omega_3 = 2\omega - \omega_4) = \frac{c}{4\pi\omega_3}\{-i\,\alpha_3 A_3 + \kappa_3^* A_4^* \exp[i(\Delta k)z]\}$$

$$\times \exp[i(\omega_3 t - \mathbf{k}_3 \cdot \mathbf{r})],$$

$$P(\omega_4 = 2\omega - \omega_3) = \frac{c}{4\pi\omega_4}\{-i\alpha_4 A_4 + \kappa_4^* A_3^* \exp[i(\Delta k)z]\}$$

$$\times \exp[i(\omega_4 t - \mathbf{k}_4 \cdot \mathbf{r})]. \qquad (2.3\text{-}10)$$

The coupling constants are given by

$$\alpha_3 = \frac{-i\alpha_0}{(\delta - \nu - i)}, \quad \alpha_4^* = \frac{i\alpha_0}{(\delta + \nu + i)},$$

$$\kappa_4 = 2\alpha_0\left[\frac{[1 - (i\nu)/2]}{(\delta + i)(1 - ia\nu)(\delta - \nu - i)(\delta + \nu + i)}\right] \cdot \frac{A_1^* A_2^*}{E_s^2}$$

$$\kappa_3^* = 2\alpha_0\left[\frac{[1 - (i\nu)/2]}{(\delta - i)(1 - ia\nu)(\delta - \nu - i)(\delta + \nu + i)}\right] \cdot \frac{A_1 A_2}{E_s^2} \qquad (2.3\text{-}11)$$

where $\delta = (\omega - \omega_0)T_2$ is the normalized detuning of the pump fields from line center, $\nu = (\omega_4 - \omega)T_2$ is the normalized detuning of the signal frequency from the pump fields, $a = T_1/T_2$, $E_s^2 = \hbar^2/T_1 T_2 \mu^2$ is the line-center saturation intensity, $\alpha_0 = 4\pi\mu^2 \Delta N_0 T_2 k_0/2\hbar$ is the line-center homogeneous-broadening absorption coefficient of the subject gas, k_0 is the magnitude of the wave number at frequency ω_0, and $\Delta k = 2(\omega_4 - \omega)/c$.

2.4 Coupled Mode Equations

Using the wave equation ($\varepsilon = \mu = 1$)

$$\nabla^2 E - \frac{1}{c^2}\frac{\partial^2}{\partial t^2}E = \frac{4\pi}{c^2}\frac{\partial^2}{\partial t^2}P \qquad (2.4\text{-}1)$$

we will derive the coupled mode equations for $A_3(z)$ and $A_4^*(z)$. The first assumption we will make is that the pump waves A_1 and A_2 are undepleted by the phase conjugation process. This assumes that the pump waves are much larger than either A_3 or A_4^* so that the fraction of pump light diffracted into the direction of the signal waves results in a negligible change in the amplitude of the pump waves. Linear absorption of the pump waves by the nonlinear medium will also be neglected as it depends on the geometry of the experiment and can easily be included as discussed below.

Suppose the pump waves propagate through a length L_p of the nonlinear medium along the s axis. Assume the nonlinear medium is contained between $s = 0$ and $s = L_p$ such that $A_1(0)$ and $A_2(L_p)$ represent the incident amplitudes of the pump waves on the material. The pump waves, as they propagate through the material, can be expressed by the following equations:

$$A_1(s) = A_1(0)\, e^{-\alpha s}$$

$$A_2(s) = A_2(L_p)\, e^{\alpha(s - L_p)} \tag{2.4-2}$$

where α is the linear absorption coefficient for the pump waves. The important quantity in the nonlinear polarization is the product $A_1(s)A_2(s)$ which becomes

$$A_1(s)A_2(s) = A_1(0)A_2(L_p)\, e^{-\alpha L_p} \tag{2.4-3}$$

We observe that the product of the pump amplitudes is independent of the position inside the material but is reduced by the factor $e^{-\alpha L_p}$. This can easily be included in the expressions for κ_i.

The first step in deriving the coupled mode equations is to equate terms in E and P which have the same frequency ω and the same wave vector $\mathbf{k}$. As an example, consider the components of E and P at ω_3 and $\mathbf{k}_3$.

$$E(\omega_3, \mathbf{k}_3) = \tfrac{1}{2}A_3(z)\exp[i(\omega_3 t + k_3 z)]$$

$$P(\omega_3, \mathbf{k}_3) = \frac{c}{4\pi\omega_3}\{-i\alpha_3 A_3(z) + \kappa_3^* A_4^*(z)$$

$$\times\exp[i(\Delta k)z]\}\exp[i(\omega_3 t + k_3 z)]. \tag{2.4-4}$$

These expressions for E and P are substituted in the wave equation, Eq. (2.4-1). Taking derivatives, we obtain

$$\frac{\partial^2}{\partial t^2}E(\omega_3, \mathbf{k}_3) = -\omega_3^2\, E(\omega_3, \mathbf{k}_3) = -\tfrac{1}{2}\omega_3^2\, A_3(z)\exp[i(\omega_3 t + k_3 z)] \tag{2.4-5}$$

$$\frac{\partial^2}{\partial t^2}P(\omega_3, \mathbf{k}_3) = -(\omega_3)^2\, P(\omega_3, \mathbf{k}_3)$$

$$= \frac{-\omega_3 c}{4\pi}\{-i\alpha_3 A_3(z) + \kappa_3^* A_4^*(z)\exp[i(\Delta k)z]\}\exp[i(\omega_3 t + k_3 z)].$$

(2.4-6)

$$\nabla^2 E(\omega_3, \mathbf{k}_3) = \frac{\partial}{\partial z}\left[\frac{1}{2}\frac{dA_3(z)}{dz} + \frac{ik_3}{2}A_3(z)\right]\exp[i(\omega_3 t + k_3 z)].$$

$$= \left[\frac{1}{2}\frac{d^2A_3(z)}{dz^2} + ik_3\frac{dA_3(z)}{dz} - \frac{1}{2}k_3^2 A_3(z)\right]\exp[i(\omega_3 t + k_3 z)]. \qquad (2.4\text{-}7)$$

Substituting into Eq. (2.4-1) yields

$$\left[\frac{1}{2}\frac{d^2A_3(z)}{dz^2} + ik_3\frac{dA_3(z)}{dz} - \frac{1}{2}k_3^2 A_3(z)\right]\exp[i(\omega_3 t + k_3 z)].$$

$$+ \frac{1}{2}\frac{\omega_3^2}{c^2}A_3(z)\exp[i(\omega_3 t + k_3 z)]$$

$$= \frac{-\omega_3}{c}\{-i\alpha_3 A_3(z) + \kappa_3^* A_4^*(z)\times\exp[i(\Delta k)z]\}\exp[i(\omega_3 t + k_3 z)]. \qquad (2.4\text{-}8)$$

Using the dispersion relation

$$\frac{\omega_3^2}{c^2} - k_3^2 = 0 \qquad (2.4\text{-}9)$$

several terms can be cancelled. In addition we will assume that

$$\left|\frac{d^2A_3}{dz^2}\right| << \left|k_3\frac{dA_3}{dz}\right| \qquad (2.4\text{-}10)$$

This is usually referred to as the adiabatic approximation, which we will use throughout this work. This simplifies the wave equation to yield

$$\frac{dA_3}{dz} = \alpha_3 A_3 + i\kappa_3^* A_4^* \exp[i(\Delta k)z], \qquad (2.4\text{-}11)$$

In a similar manner we can obtain the mode equation for A_4^*. This becomes

$$\frac{dA_4^*}{dz} = -\alpha_4^* A_4^* + i\kappa_4 A_3 \exp[-i(\Delta k)z]. \qquad (2.4\text{-}12)$$

The solutions to Eqs. (2.4-11) and (2.4-12), using the boundary conditions of $A_3(z = L) = A_3(L)$ and $A_4^*(z = 0) = A_4^*(0)$, are

$$A_3(z) = \frac{i\kappa_3^*}{D}\left[e^{iS_1 z} - e^{i(S_1 - S_2)L} e^{iS_2 z} \right] A_4^*(0)$$

$$+ \frac{e^{-iS_2 L}}{D}\left[(\alpha_3 - iS_2)e^{iS_1 z} - (\alpha_3 - iS_1)e^{iS_2 z} \right] A_3(L)$$

$$A_4^*(z) = \frac{e^{-i\Delta k z}}{D}\left[(\alpha_3 - iS_2)e^{i(S_1 - S_2)L} e^{iS_2 z} - (\alpha_3 - iS_1)e^{iS_1 z} \right] A_4^*(0)$$

$$+ \frac{e^{-i\Delta k z}}{D} \frac{(iS_1 - \alpha_3)(iS_2 - \alpha_3)}{i\kappa_3^*} e^{-iS_2 L}\left[e^{iS_2 z} - e^{iS_1 z} \right] A_3(L) \qquad (2.4\text{-}13)$$

where

$$S_1 = (-i/2)(\alpha_3 - \alpha_4^* + i\Delta k) + (1/2)[4\kappa_3^*\kappa_4 - (\alpha_3 + \alpha_4^*)^2 + (\Delta k)^2$$

$$+ 2i\Delta k(\alpha_3 + \alpha_4^*)]^{1/2},$$

$$S_2 = (-i/2)(\alpha_3 - \alpha_4^* + i\Delta k) - (1/2)[4\kappa_3^*\kappa_4 - (\alpha_3 + \alpha_4^*)^2 + (\Delta k)^2$$

$$+ 2i\Delta k(\alpha_3 + \alpha_4^*)]^{1/2}.$$

$$D = \alpha_3(e^{i(S_1 - S_2)L} - 1) + i(S_1 - S_2 e^{i(S_1 - S_2)L}) \qquad (2.4\text{-}14)$$

Since we are interested in the filter application we will consider the case of a single input $A_4^*(0)$, with $A_3(L) = 0$. In this case, the solution for the reflected wave at the input plane becomes

$$A_3(0) = \frac{i\kappa_3^*}{D}\left[1 - e^{i(S_1 - S_2)L} \right] A_4^*(0) \qquad (2.4\text{-}15)$$

We can now appreciate a very important filter characteristic of the four-wave mixing process. $A_3(0)$ is proportional to $A_4^*(0)$, which implies that the output is a phase conjugate of the input wave. In other words we have time reversed the input wave except for a small shift in frequency since $\Delta k \neq 0$. If the input wave is passed

through various optical devices such as a spatial filter and a lens system the output wave will retrace its path and we can greatly enhance the signal to noise ratio of the filter using this technique. However this is done at the expense of the field of view of the filter.

The power reflection coefficient is defined as

$$R \equiv |A_3(0)|^2 / |A_4(0)|^2. \tag{2.4-16}$$

The solution for R is

$$R = \left| \frac{\kappa_3^* \{1 - \exp[i(S_1 - S_2)L]\}}{i\{S_1 - S_2 \exp[i(S_1 - S_2)L]\} + \alpha_3\{\exp[i(S_1 - S_2)L] - 1\}} \right|^2. \tag{2.4-17}$$

It should be noted that the reflected wave is frequency shifted from the incident wave. The output frequency is upshifted from the pump frequency by the same amount that the input frequency is downshifted from the pump, and vice versa. However, the frequency shift is very small for any significant reflection coefficient.

Using $\alpha_0 L = 1$, $a = 1/2$, $2L/cT_2 = 0.01$, and $A_1 A_2 / E_s^2 = 0.1$, the frequency dependence of the the reflected (output) signal is studied.

In the degenerate case ($\nu = 0$), Fig. 2.3 shows the dependence of the reflection coefficient on the pump detuning δ. The plot indicates that the reflectivity diminishes very rapidly with increasing δ. From Eqs. (2.3-11) we expect R to be inversely proportional to the sixth power of δ for δ larger than unity. Therefore operation near line-center is necessary to optimize the amplitude of the reflected wave. However, under certain situations, for example, $\alpha_0 L >> 1$, it would be advantageous to have the pump fields detuned from line-center. Fig. 2.4 shows the reflection coefficient, normalized to unity, plotted versus the signal detuning ν for several small values of the pump detuning δ. The important feature to notice is the broadening of the curves as δ increases. As shown clearly in Fig. 2.5, the normalized bandwidth $B = \Delta\omega T_2$ ($\Delta\omega$ is defined as the full width at the half maximum of $R(\nu = 0)$)

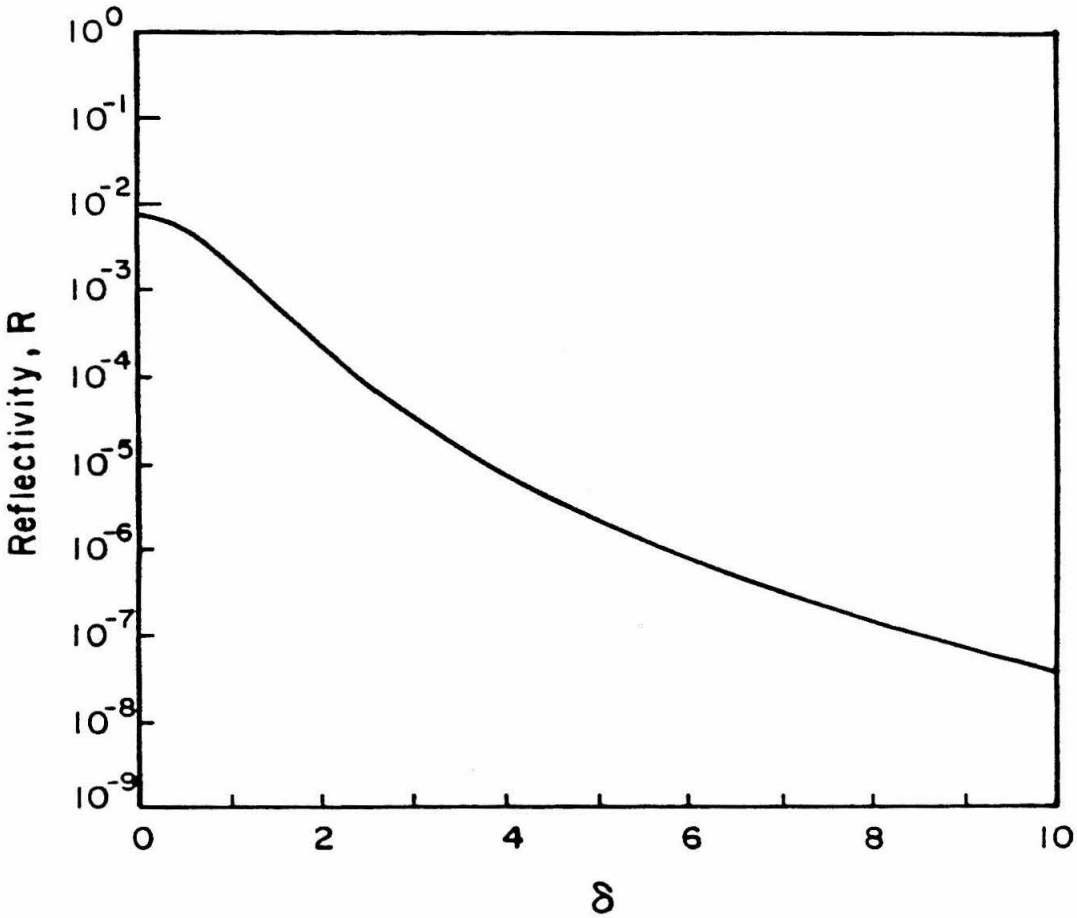

Fig. 2.3 Reflectivity, for degenerate four-wave mixing, versus pump detuning δ

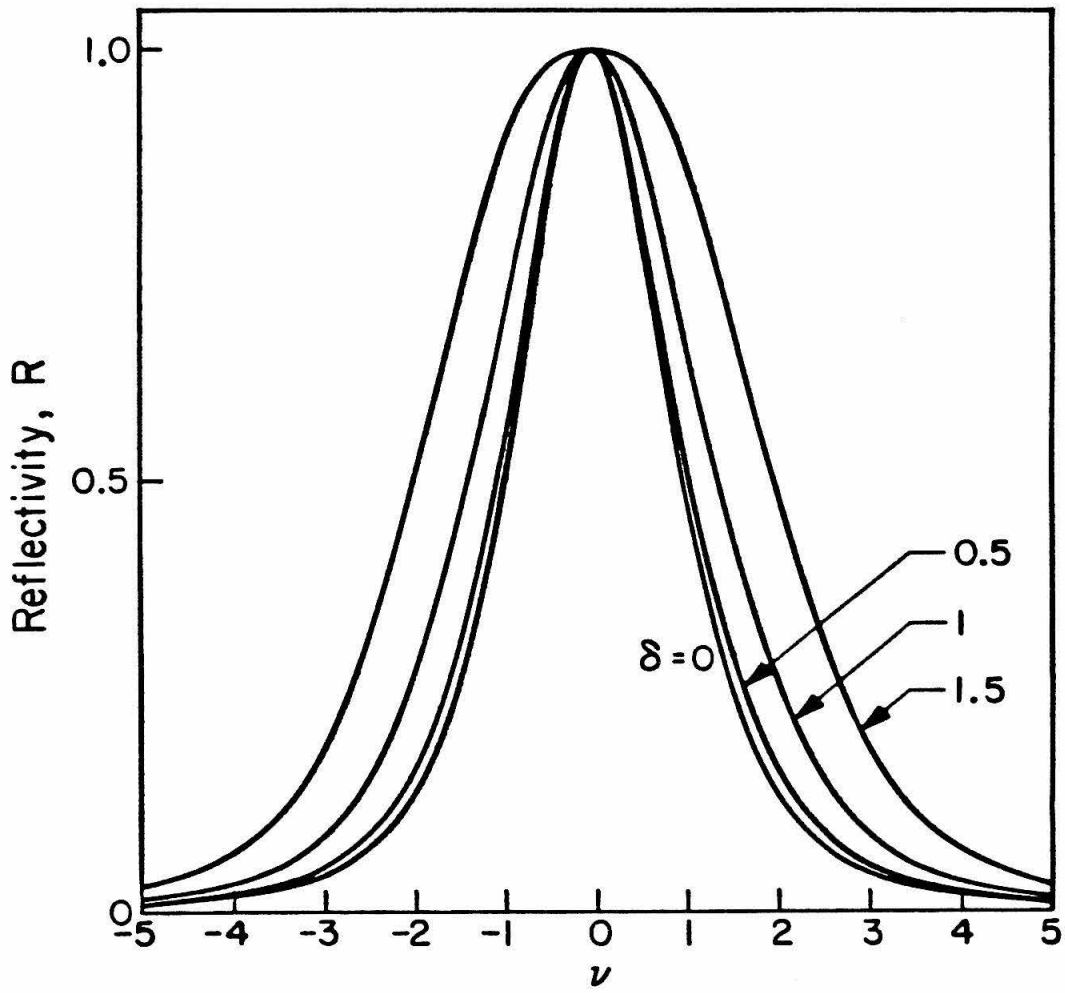

Fig. 2.4 Reflection coefficient versus signal detuning ν for several values of the pump detuning δ. All curves are normalized to unit reflectivity in order to more clearly display the bandwidth of the system.

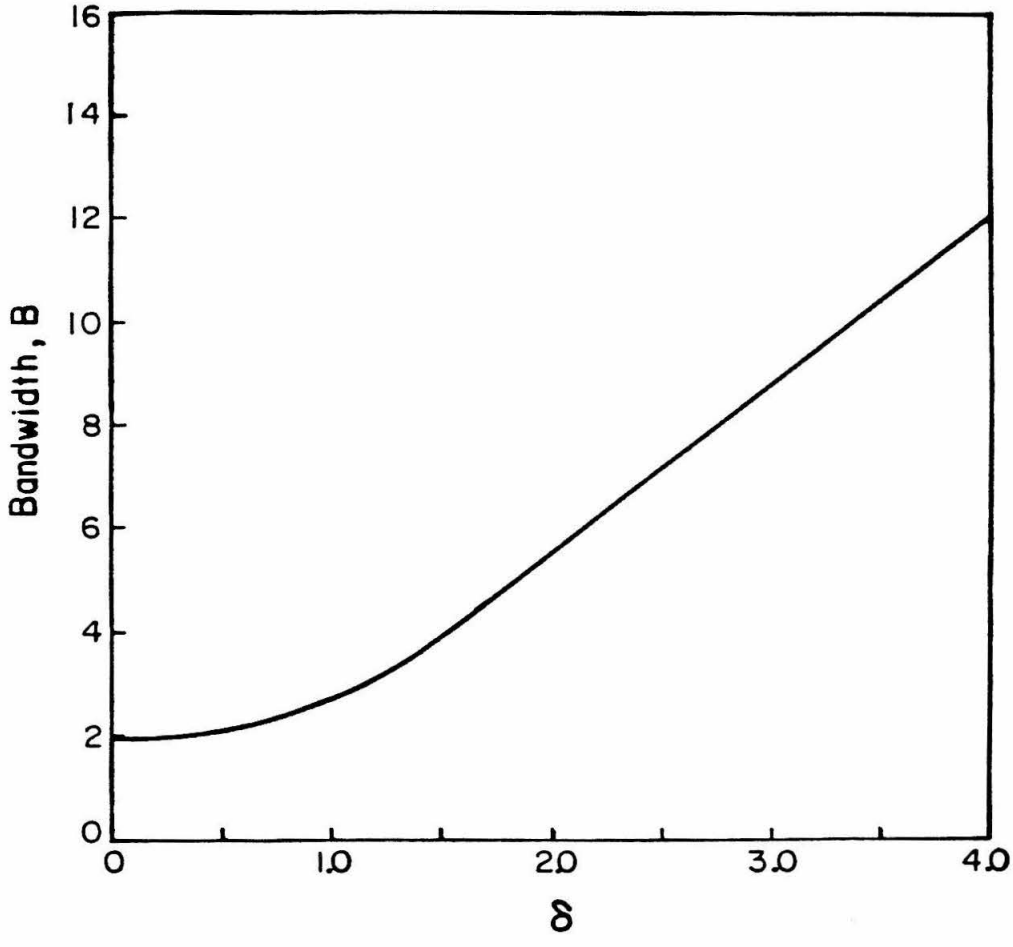

Fig. 2.5 Normalized bandwidth ($B = \Delta\omega T_2$) versus pump detuning δ

increases with the pump detuning δ. For larger δ, Fig. 2.6 shows the absolute reflectivity plotted versus the signal detuning ν. The reflection coefficient takes on a double peaked structure. The peaks are at $\nu = \pm A\delta$ with A = .50,.88,.95,.97,and.98 respectively, as δ increases from 2 to 10 in the plot. Apparently the value of A approaches unity for large δ. Physically, the peak occurring at $\nu = -\delta$ corresponds to $\omega_4 = \omega_0$ while the peak at $\nu = +\delta$ corresponds to $\omega_3 = \omega_0$. The peaks are due to an enhancement of the nonlinear coupling coefficients by having either the signal wave or the phase conjugate wave resonant with the two-level system.

It should be noted that the values we have chosen for $2L/cT_2$ makes phase mismatch constraints a negligible consideration and the frequency response is dominated by the frequency dependence of the nonlinear coupling coefficients. For example, if we choose a system such as sodium, where T_2 = 32nsec, then our choice of $2L/cT_2$ implies an interaction length L = 5cm. This is a resonable choice of values for an experiment[4-6]. In the next section we will consider the effect of phase mismatch constraints only.

2.5 Effect of Phase Mismatch

If we take the nonlinear medium to be a nondispersive, lossless medium possessing a third-order nonlinear optical susceptibility $\chi^{(3)}$ and use the same fields as before, Eqs. (2.4-11) and (2.4-12), the coupled mode equations now become

$$\frac{dA_3}{dz} = i\kappa_3^* A_4^* \exp[i(\Delta k)z],$$

$$\frac{dA_4^*}{dz} = i\kappa_4 A_3 \exp[-i(\Delta k)z], \qquad (2.5\text{-}1)$$

where $\kappa_i^* = \frac{2\pi\omega_i}{c}\chi^{(3)} A_1 A_2$ and the phase mismatch is

$$\Delta k = 2(\omega_4 - \omega)/c \qquad (2.5\text{-}2)$$

As before, we assume that the pump fields are nondepleted and use the adiabatic

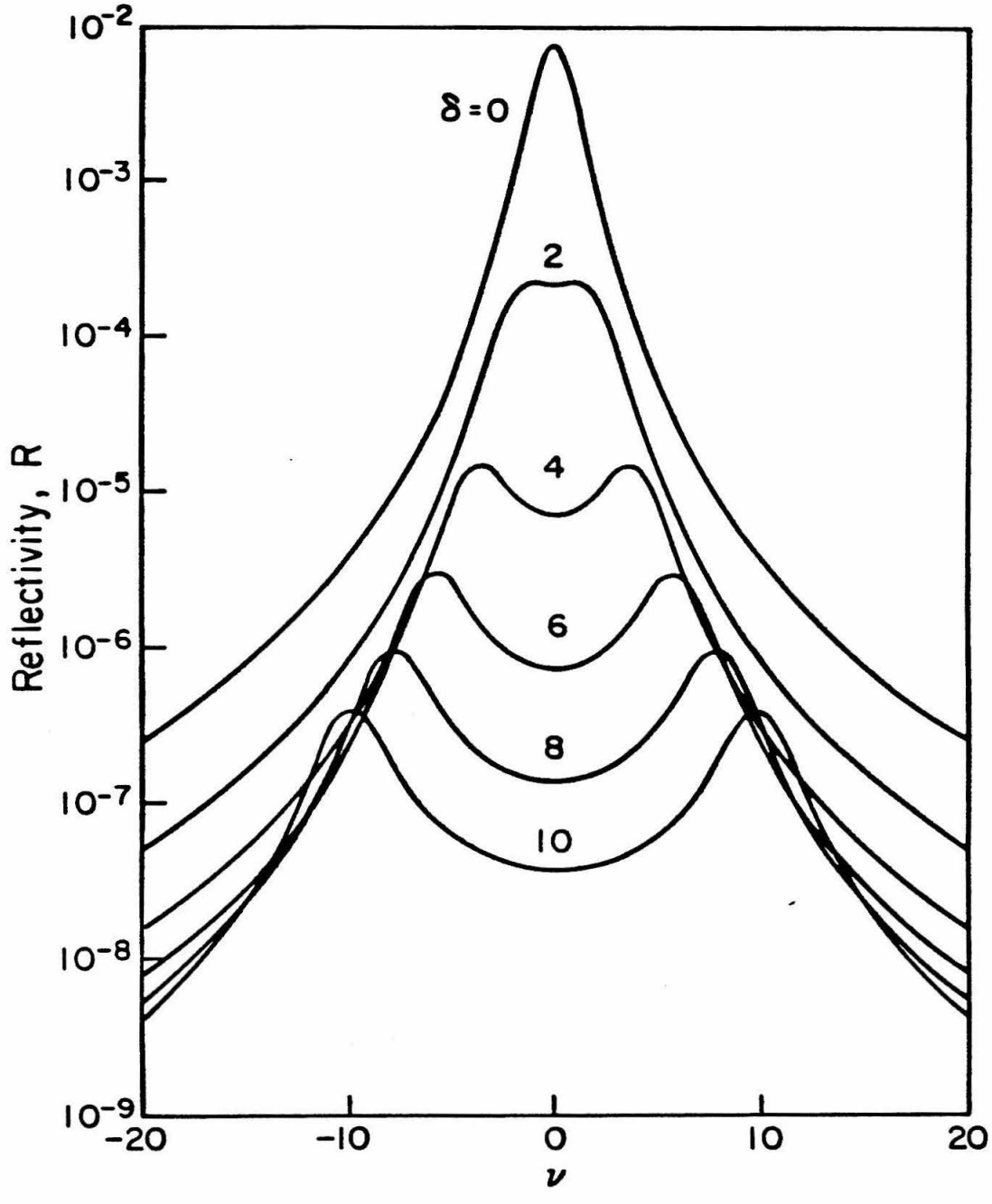

Fig. 2.6 Reflectivity versus signal detuning ν for several values of the pump detuning δ.

approximation.

Since we are primarily concerned with the filter application, we assume that $A_3(L) = 0$ with only a single input $A_4^*(0)$ at $z = 0$. The solution for the phase conjugate wave[7,8] is

$$A_3(0) = \frac{-i\kappa_3^* \tan(\beta L)\, A_4^*(0)}{\beta - \frac{i\Delta k}{2}\tan(\beta L)} \tag{2.5-3}$$

with β defined as

$$\beta \equiv [\, \kappa_3^* \kappa_4 + (\Delta k/2)^2 \,]^{1/2} . \tag{2.5-4}$$

As before we note that $A_3(0) \propto A_4^*(0)$, implying the output wave is time reversed. If we look at the limit of weak coupling, $|\, \kappa_i/\Delta k \,| \to 0$, the power reflection coefficient becomes

$$R \to |\kappa L|^2 \left\{ \frac{\sin(\frac{\Delta kL}{2})}{(\frac{\Delta kL}{2})} \right\}^2 \tag{2.5-5}$$

using $\kappa_3 \approx \kappa_4 \equiv \kappa$.

Fig. 2.7 shows the normalized reflectivity plotted versus ν^* with $\nu^* = \Delta kL/2$. An equivalent expression for ν^* is $(\omega_4 - \omega)L/c$. The full width half maximum bandwidth for R is $\nu^* = 2.78$. To compare this with the results of the previous section we can define $T_2^* = L/c$. ν^* can now be rewritten as $\nu^* = (\omega_4 - \omega)T_2^*$. The bandwidth is now a function of T_2^*. For L = 5cm, $T_2^* = .17$nsec. This shows that the effect of the phase mismatch is not as important as the frequency dependence of the coupling coefficients since the larger of $[T_2, T_2^*]$ will dominate the frequency response. For the case of sodium, where $T_2 = 32$nsec, L would have to equal 960cm for the phase mismatch constraints to be of equal importance in determining the filter response.

We can compare the four-wave mixing process with real time holography. The

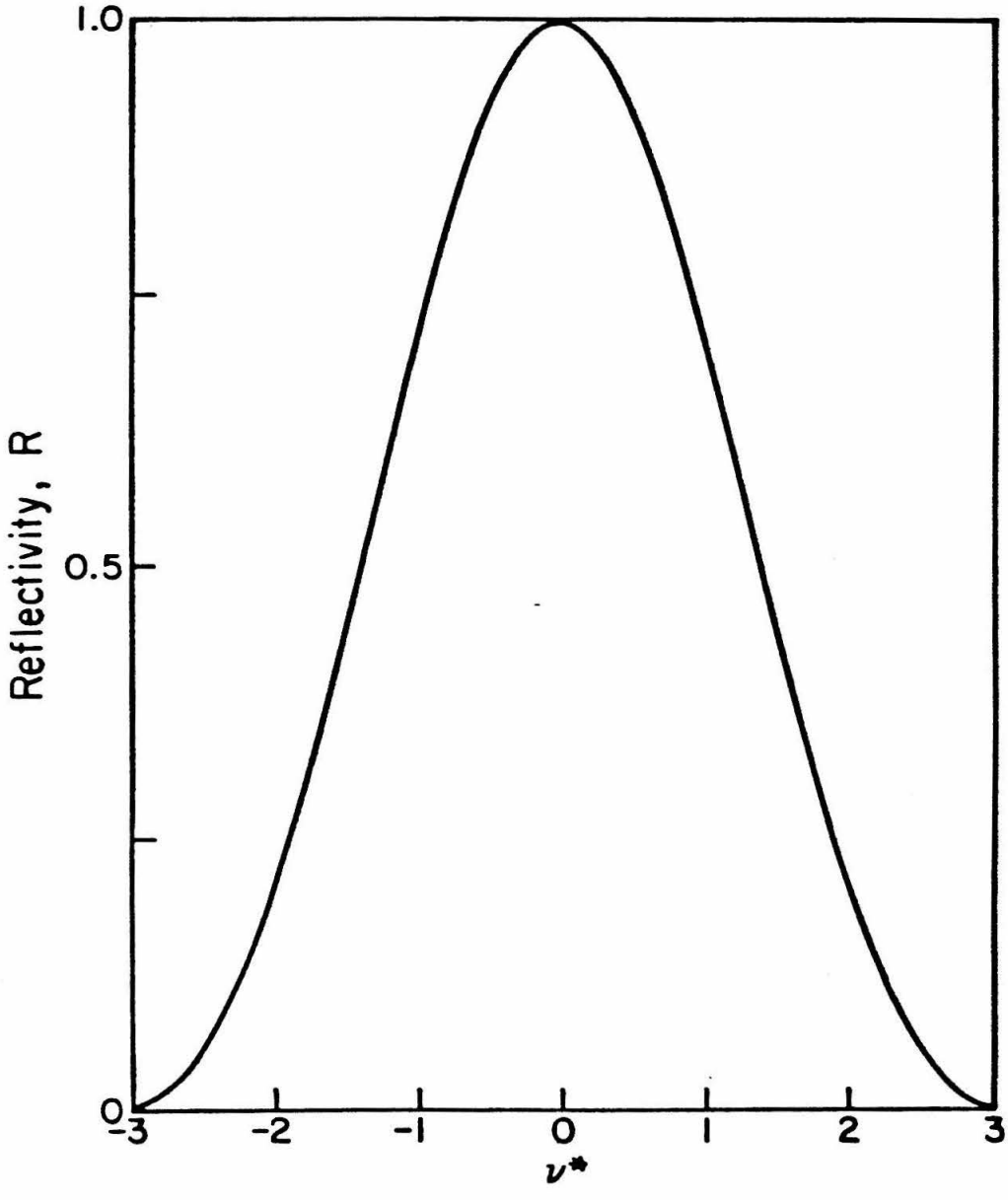

Fig. 2.7 Reflectivity, normalized to unity, versus the phase mismatch parameter ν^*

nonlinear mixing can be viewed as forming and illuminating a real time diffraction grating. From Eq. (2.5-5) we see that phase matching occurs for $(\Delta kL/2) \leq \pi$. This gives a wavelength resolution of $(\Delta\lambda/\lambda) \leq (\lambda/L)$. This result is consistent with the resolution of a diffraction grating $(\Delta\lambda/\lambda) \approx 1/mN$, where N is the number of lines illuminated and m is the order of the grating. For four-wave mixing only the first order terms are phase matched so we set m = 1. N, the number of lines illuminated, is analagous to L/λ.

2.6 Conclusion

In this chapter we have demonstrated how nondegenerate four-wave mixing in a homogeneously broadened two-level system can yield an active narrow bandwidth optical filter, which also has a large field of view (i.e., several steradians). The large field of view is a consequence of the fact that four-wave mixing does not depend on phase matching. The frequency response depends primarily on T_2 for the values presented here. The bandwidth is directly proportional to the inverse of the relaxation time T_2 and monotonically increases with the pump detuning δ. The effects of phase matching have been discussed and we have shown how they are dominated by the frequency dependence of the nonlinear coupling coefficients for many experimental situations involving resonant systems.

References for Chapter II

1. J. Nilsen and A. Yariv, "Nearly degenerate four-wave mixing applied to optical filters," Appl. Opt. 18,143 (1979).

2. A. Yariv, **Quantum Electronics** (Wiley, New York, 1975), pp. 149-155, 418-421, 553-558.

3. A. Yariv and D. M. Pepper, "Amplified reflection, phase conjugation, and oscillation in degenerate four-wave mixing," Opt. Lett. 1,16 (1977).

4. J. Nilsen, N. S. Gluck, and A. Yariv, "Narrowband optical filter via phase conjugation by nondegenerate four-wave mixing in sodium vapor," Opt. Lett. 6,380 (1981).

5. L. M. Humphrey, J. P. Gordon, and P. F. Liao, "Angular dependence of line shape and strength of degenerate four-wave mixing in a Doppler-broadened system with optical pumping," Opt. Lett. 5,56 (1980)

6. P. F. Liao, D. M. Bloom, and N. P. Economou, "CW optical wave-front conjugtion by saturated absorption in atomic sodium vapor," Appl. Phys. Lett. 32,813 (1978)

7 D. M. Pepper, "Phase conjugate optics: On the theory, observation, and utilization of temporally-reversed wavefronts as generated via nonlinear optical parametric interactions," thesis, California Institute of Technology (1980).

8. D. M. Pepper and R. L. Abrams, "Narrow optical bandpass filter via nearly degenerate four-wave mixing," Opt. Lett. 3,212 (1978).

Chapter III

NONDEGENERATE FOUR-WAVE MIXING IN A DOPPLER-BROADENED TWO-LEVEL SYSTEM

3.1 Introduction

In the last chapter we studied phase conjugation via nondegenerate four-wave mixing in a homogeneously broadened two-level system. Many nonlinear media of interest are resonant systems which are inhomogeneously broadened[1-5] due to atomic motion. In this chapter we will extend our previous treatment of phase conjugation to include the effects of atomic motion (Doppler broadening) on the four-wave mixing process. The results[6,7] presented can be used to analyze the efficiency of four-wave mixing in spectroscopy, optical filters, and other applications.

3.2 Density Matrix Equations for a Doppler-Broadened Two-Level System

The model of a two-level system introduced in the previous chapter[8] is still valid except that now we will assume the ensemble of atoms has a velocity distribution given by the Doppler profile.

The velocity dependence of the density matrix equations can be taken into account by replacing

$$\frac{d}{dt} \text{ with } \frac{\partial}{\partial t} + \mathbf{v} \cdot \nabla \tag{3.2-1}$$

in Eqs. (2.2-12). The resulting equations are

$$\frac{\partial \rho_{21}}{\partial t} + \mathbf{v} \cdot \nabla \rho_{21} = -i\omega_0 \rho_{21} + i\frac{\mu}{\hbar} E(\mathbf{r},t)(\rho_{11} - \rho_{22}) - \frac{\rho_{21}}{T_2}$$

$$\frac{\partial}{\partial t}(\rho_{11} - \rho_{22}) + \mathbf{v} \cdot \nabla \ (\rho_{11} - \rho_{22}) = 2i\frac{\mu}{\hbar} E(\mathbf{r},t)(\rho_{21} - \rho_{21}^*) - \frac{(\rho_{11} - \rho_{22}) - (\rho_{11} - \rho_{22})_0}{T_1}$$

(3.2-2)

This is analagous to considering the problem in the frame of an atom with velocity $\mathbf{v}$, Doppler shifting the waves into this frame as shown in Fig. 3.1 ,solving Eqs. (3.2-2) in this frame, and then transforming back into the laboratory frame.

Generalizing the problem slightly, the mixing will involve two intense counterpropagating pump waves E_1 and E_2 of frequencies ω_1 and ω_2, respectively, and two weak counterpropagating signal waves E_3 and E_4 with frequencies ω_3 and ω_4. The geometry of Yariv and Pepper[9] shown in Fig. 2.2 is used. The fields are taken as plane waves:

$$E_i(r_i,t) = \tfrac{1}{2}A_i(r_i)\exp[i(\omega_i t - \mathbf{k}_i\cdot\mathbf{r})] + \text{c.c.}, \tag{3.2-3}$$

where r_i is the distance along $\mathbf{k}_i$. We have

$$\omega_1 + \omega_2 = \omega_3 + \omega_4 = 2\omega. \tag{3.2-4}$$

The density matrix equations are then solved to third-order by pertubation theory for an atom of velocity $\mathbf{v}$ to determine the induced polarizations at ω_3 and ω_4.

$$P(\omega_3 = 2\omega - \omega_4, \mathbf{v}_N) = \frac{c}{4\pi\omega_3}\{-i\alpha_3(\mathbf{v}_N)A_3 + \kappa_3^*(\mathbf{v}_N)A_4^*\exp[i(\Delta k)z]\}$$

$$\times\exp[i(\omega_3 t - \mathbf{k}_3\cdot\mathbf{r})],$$

$$P(\omega_4 = 2\omega - \omega_3, \mathbf{v}_N) = \frac{c}{4\pi\omega_4}\{-i\alpha_4(\mathbf{v}_N)A_4 + \kappa_4^*(\mathbf{v}_N)A_3^*\exp[i(\Delta k)z]\}$$

$$\times\exp[i(\omega_4 t - \mathbf{k}_4\cdot\mathbf{r})]. \tag{3.2-5}$$

The velocity dependent coupling constants appearing in Eqs. (3.2-5) are given by

$$\alpha_3(\mathbf{v}_N) = \frac{-i\alpha_0}{(\delta - \nu - \mathbf{n}_3\cdot\mathbf{v}_N - i)}, \quad \alpha_4^*(\mathbf{v}_N) = \frac{i\alpha_0}{(\delta + \nu - \mathbf{n}_4\cdot\mathbf{v}_N + i)},$$

$$\kappa_3^*(\mathbf{v}_N) = \frac{\alpha_0}{2}\frac{A_1A_2}{E_s^2}\left\{\frac{-i}{(\delta + \varepsilon - \mathbf{n}_1\cdot\mathbf{v}_N - i)[1 - ia(\nu - \varepsilon) + ia\mathbf{v}_N\cdot(\mathbf{n}_4 - \mathbf{n}_1)](\delta - \nu - \mathbf{n}_3\cdot\mathbf{v}_N - i)}\right.$$

$$\left. + \frac{-i}{(\delta - \varepsilon - \mathbf{n}_2\cdot\mathbf{v}_N - i)[1 - ia(\nu + \varepsilon) + ia\mathbf{v}_N\cdot(\mathbf{n}_4 - \mathbf{n}_2)](\delta - \nu - \mathbf{n}_3\cdot\mathbf{v}_N - i)}\right.$$

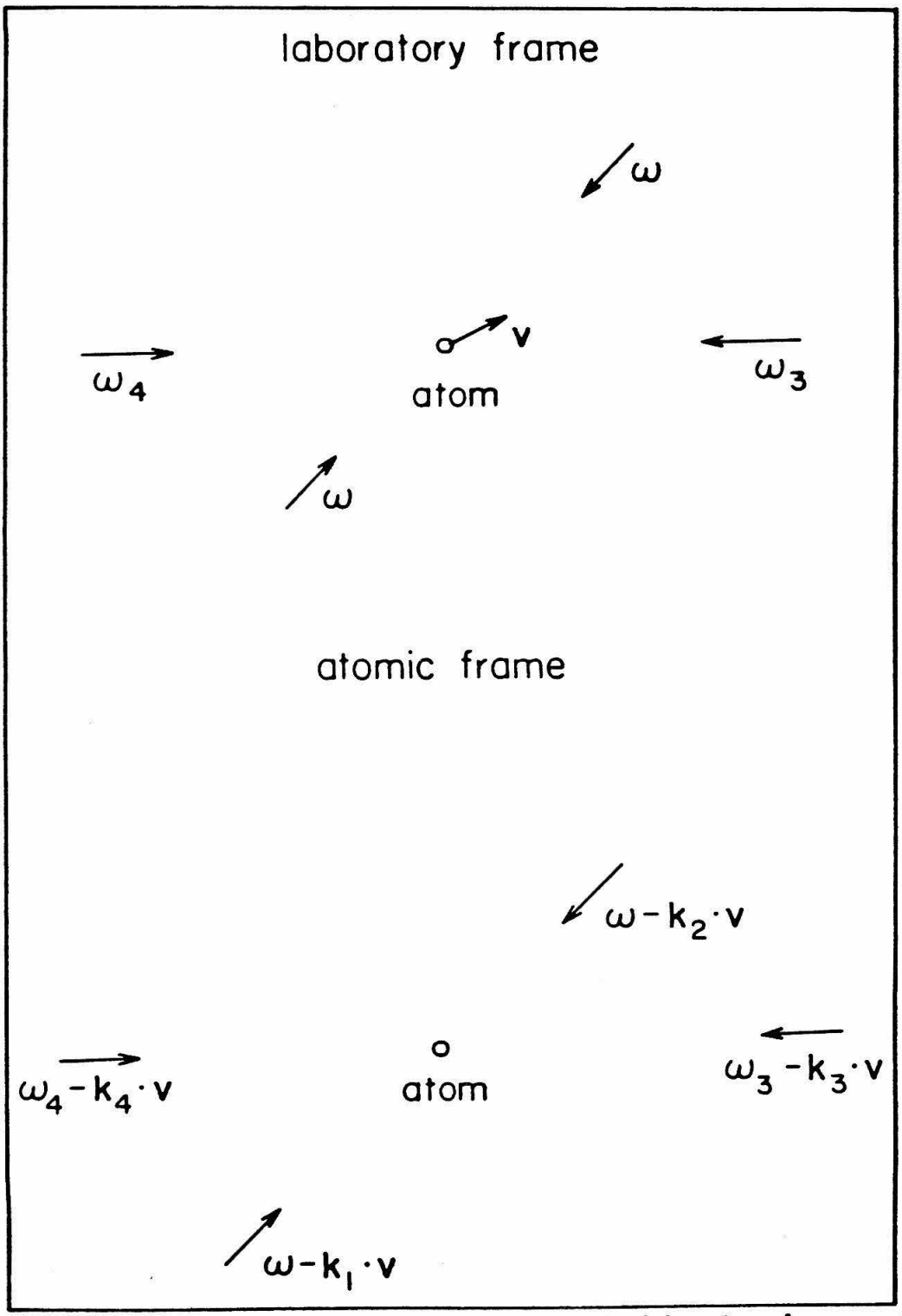

Fig. 3.1 Frequencies of the electric fields in the laboratory frame and the atomic frame.

$$+\frac{i}{(\delta+\nu-\mathbf{n}_4\cdot\mathbf{v}_N+i)[1-ia(\nu-\varepsilon)+ia\mathbf{v}_N\cdot(\mathbf{n}_4-\mathbf{n}_1)](\delta-\nu-\mathbf{n}_3\cdot\mathbf{v}_N-i)}$$

$$+\frac{i}{(\delta+\nu-\mathbf{n}_4\cdot\mathbf{v}_N+i)[1-ia(\nu+\varepsilon)+ia\mathbf{v}_N\cdot(\mathbf{n}_4-\mathbf{n}_2)](\delta-\nu-\mathbf{n}_3\cdot\mathbf{v}_N-i)}\Big\},$$

$$\kappa_4(\mathbf{v}_N)=\frac{\alpha_0}{2}\frac{A_1^*A_2^*}{E_s^2}\Big\{\frac{i}{(\delta+\varepsilon-\mathbf{n}_1\cdot\mathbf{v}_N+i)[1-ia(\nu+\varepsilon)+ia\mathbf{v}_N\cdot(\mathbf{n}_1-\mathbf{n}_3)](\delta+\nu-\mathbf{n}_4\cdot\mathbf{v}_N+i)}$$

$$+\frac{i}{(\delta-\varepsilon-\mathbf{n}_2\cdot\mathbf{v}_N+i)[1-ia(\nu-\varepsilon)+ia\mathbf{v}_N\cdot(\mathbf{n}_2-\mathbf{n}_3)](\delta+\nu-\mathbf{n}_4\cdot\mathbf{v}_N+i)}$$

$$+\frac{-i}{(\delta-\nu-\mathbf{n}_3\cdot\mathbf{v}_N-i)[1-ia(\nu+\varepsilon)+ia\mathbf{v}_N\cdot(\mathbf{n}_1-\mathbf{n}_3)](\delta+\nu-\mathbf{n}_4\cdot\mathbf{v}_N+i)}$$

$$+\frac{-i}{(\delta-\nu-\mathbf{n}_3\cdot\mathbf{v}_N-i)[1-ia(\nu-\varepsilon)+ia\mathbf{v}_N\cdot(\mathbf{n}_2-\mathbf{n}_3)](\delta+\nu-\mathbf{n}_4\cdot\mathbf{v}_N+i)}\Big\}, \tag{3.2-6}$$

where $\delta+\varepsilon=(\omega_1-\omega_0)T_2$ is the normalized detuning of the pump field E_1 from line center, $\delta-\varepsilon=(\omega_2-\omega_0)T_2$ is the normalized detuning of the pump field E_2 from line center, $\nu=(\omega_4-\omega)T_2$ is the normalized detuning of the signal frequency from the average pump frequency ω, $a=T_1/T_2$, $E_s^2=\hbar^2/T_1T_2\mu^2$ is the line-center saturation intensity, $\alpha_0=4\pi\mu^2\Delta N_0T_2k_0/2\hbar$ is the line-center homogeneous-broadening absorption coefficient of a gas with the same density as the subject gas, k_0 is the magnitude of the wave number at frequency ω_0, $\Delta k=(\mathbf{k}_4+\mathbf{k}_3-\mathbf{k}_1-\mathbf{k}_2)\cdot\mathbf{n}_4$, $\mathbf{n}_i=\mathbf{k}_ic/\omega_i$ is the normalized wave vector, and $\mathbf{v}_N=\omega_0T_2\mathbf{v}/c$ is the normalized velocity.

3.3 Doppler Profile

The probability function for the velocity distribution is given by

$$\rho(\mathbf{v}_N)=\frac{1}{(\pi u_N^2)^{3/2}}\exp[-(v_N/u_N)^2], \tag{3.3-1}$$

where u_N is the normalized Doppler velocity spread. The macroscopic polarizations that are used in Maxwell's equations are derived by summing the contributions from all velocities $\mathbf{v}$. The resulting expressions are identical with Eqs. (3.2-5) but with the

coupling constants $\alpha_i(\mathbf{v}_N)$, $\kappa_i(\mathbf{v}_N)$ replaced by their averages over all velocities. These are given by

$$\alpha_3 = \int \rho(\mathbf{v}_N)\alpha_3(\mathbf{v}_N)d^3v_N,$$

$$\alpha_4^* = \int \rho(\mathbf{v}_N)\alpha_4^*(\mathbf{v}_N)d^3v_N,$$

$$\kappa_4 = \int \rho(\mathbf{v}_N)\kappa_4(\mathbf{v}_N)d^3v_N,$$

$$\kappa_3^* = \int \rho(\mathbf{v}_N)\kappa_3^*(\mathbf{v}_N)d^3v_N, \qquad (3.3\text{-}2)$$

These coefficients are a function of δ, ε, and ν as well as the wave directions $\mathbf{n}_1$, $\mathbf{n}_2$, $\mathbf{n}_3$, $\mathbf{n}_4$, but no longer of $\mathbf{v}_N$.

We will consider the integrations in Eqs. (3.3-2) in the Doppler-broadened region ($u_N >> 1$). The integrations for α_i can be expressed in terms of the plasma dispersion function[10] which is tabulated. The solutions for α_i are given by

$$\alpha_3 = \frac{-i\alpha_0}{u_N} Z(\zeta_1), \quad \text{with} \quad \zeta_1 = \frac{\nu - \delta + i}{u_N}$$

$$\alpha_4^* = \frac{-i\alpha_0}{u_N} Z(\zeta_2), \quad \text{with} \quad \zeta_2 = \frac{\nu + \delta + i}{u_N} \qquad (3.3\text{-}3)$$

with the plasma dispersion fuction defined as

$$Z(\zeta) = \frac{1}{\sqrt{\pi}} \int_{-\infty}^{\infty} dx \, \frac{e^{-x^2}}{x - \zeta} \qquad (3.3\text{-}4)$$

for Im $\zeta > 0$. In this work the integrations are done numerically on an IBM 370/3032 computer.

The two dimensional integrations for κ_i are very time consuming on the computer so we have obtained approximate analytic expressions for them. We assume that the signal and pump waves are in the x-z plane with the signal wave along the z direction as shown in Fig. 2.2. The gaussian distribution in Eq. (3.3-1) is modeled by the inverse of a sixth-order polynomial for the gaussian with the $(v_N)_x$ dependence

and by the inverse of a fourth order polynomial for the gaussian with the $(v_N)_z$ dependence. This is done because the $(v_N)_z$ integral is for a sharply peaked function times a gaussian so only the value of the gaussian near $(v_N)_z = 0$ is important. On the other hand, the $(v_N)_x$ integral consists of a slowly varying function times a gaussian so we require a more accurate approximation for the gaussian function. The gaussian approximation[11] is given by:

$$\rho[(v_N)_x, (v_N)_z] = \frac{a_0}{[\, 2u_N^4 + 2u_N^2(v_N)_z^2 + (v_N)_z^4 \,][\, a_1 u_N^6 + a_2 u_N^4 (v_N)_x^2 + a_3 u_N^2 (v_N)_x^4 + (v_N)_x^6 \,]} \tag{3.3-5}$$

where

$$a_0 = 1.075871\, u_N^8 \qquad a_1 = 1.679374$$

$$a_2 = 2.002844 \qquad a_3 = -0.06753022$$

The integrations are done by contour integration. In the summation over the residues, only those residues with dominant poles closest to the origin are included. Fig. 3.2 shows the comparison between the gaussian distribution and the analytic approximation as a function of $(v_N)_x$ for $(v_N)_z = 0$. The solid curve plots a one dimensional gaussian, normalized to unity at the origin, versus the normalized coordinate $x = (v_N)_x/u_N$. The open circles are the data points generated by the approximation in Eq. (3.3-5) The fit is excellent, differing by no more than 1% over the range x=0 → x=1 and by no more than 0.01 in absolute value over the entire range of x in the figure.

For small positive angles, the gaussian distribution in Eq. (3.3-1) is modeled by a polynomial[11] and used in Eqs. (3.3-2) to obtain the nonlinear coupling coefficients. This is given by

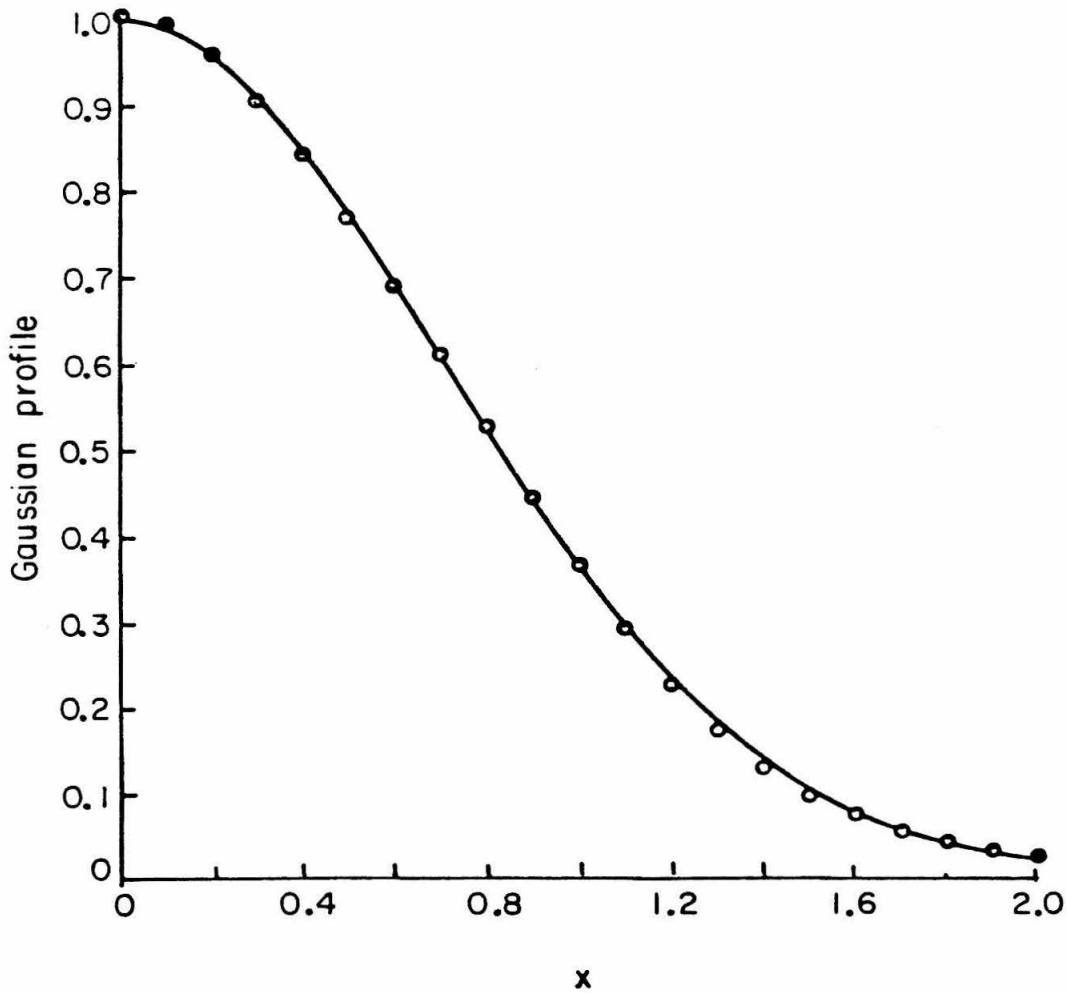

Fig. 3.2 Comparison of a gaussian, solid curve, with a polynomial fit given in Eq. (3.3-5), open circles.

$$\kappa_3^* L = \alpha_0 L \frac{A_1 A_2}{E_s^2} \frac{i c_1}{u_N \cos(\varphi/2)} \exp[-(\varepsilon/u_N)^2]$$

$$\times \left\{ \frac{1}{[1 + 2ac_2 u_N \sin(\varphi/2) + ia(\varepsilon - \nu)][2 + 2c_2 u_N \sin(\varphi/2) + i(2\delta + \varepsilon - \nu)]} \right.$$

$$+ \frac{i c_3 e^{i\varphi_1}}{[1 + 2ac_4 u_N \sin(\varphi/2) e^{i\varphi_2} + ia(\varepsilon - \nu)][2 + 2c_4 u_N \sin(\varphi/2) e^{i\varphi_2} + i(2\delta + \varepsilon - \nu)]}$$

$$\left. + \frac{-i c_3 e^{-i\varphi_1}}{[1 + 2ac_4 u_N \sin(\varphi/2) e^{-i\varphi_2} + ia(\varepsilon - \nu)][2 + 2c_4 u_N \sin(\varphi/2) e^{-i\varphi_2} + i(2\delta + \varepsilon - \nu)]} \right\} \tag{3.3-6}$$

with

$$c_1 = 1.878693 \qquad \varphi_1 = 4.1182°,$$

$$c_2 = 0.819668 \qquad \varphi_2 = 51.7614°,$$

$$c_3 = 0.3937158,$$

$$c_4 = 1.257383.$$

For $\varphi = 0°$, the coupling constants can be approximated by

$$\kappa_4 = \alpha_0 \frac{A_1^* A_2^*}{E_s^2} \frac{\sqrt{\pi}}{u_N} \frac{1}{[1 - ia(\nu - \varepsilon)](2\delta + \nu - \varepsilon + 2i)} \exp[-(\varepsilon/u_N)^2],$$

$$\kappa_3^* = \alpha_0 \frac{A_1 A_2}{E_s^2} \frac{\sqrt{\pi}}{u_N} \frac{1}{[1 - ia(\nu - \varepsilon)](2\delta - \nu + \varepsilon - 2i)} \exp[-(\varepsilon/u_N)^2]. \tag{3.3-7}$$

3.4 Numerical Results

The coupling constants calculated in the previous section are used in the mode equations

$$\frac{dA_3}{dz} = \alpha_3 A_3 + i\kappa_3^* A_4^* \exp[i(\Delta k)z],$$

$$\frac{dA_4^*}{dz} = -\alpha_4^* A_4^* + i\kappa_4 A_3 \exp[-i(\Delta k)z], \tag{3.4-1}$$

to describe the evolution of waves A_3 and A_4^*.

We will study the frequency and angular dependencies of the reflected signal for the case of a single input wave $A_4^*(0)$. The reflection coefficient R was previously defined in Eq. (2.4-16) and can be approximated by

$$R \approx |\kappa_3 L|^2 (1 - e^{-2\alpha_R L})^2 / 4\alpha_R^2 L^2 \tag{3.4-2}$$

with $2\alpha_R = \mathrm{Re}(\alpha_3 + \alpha_4^*)$ when phase mismatch constraints[6,7,12] can be neglected. The parameters are chosen to be $a = 1/2$, $u_N = 100$, $2L/cT_2 = 0.01$, $A_1A_2/E_s^2 = 0.1$, $\alpha_0 L\sqrt{\pi}/u_N = 0.1$.

First we will consider the degenerate case, $\nu = \varepsilon = 0$. Fig. 3.3 shows the reflection coefficient plotted versus sin φ (φ is the angle between $\mathbf{k}_1$ and $\mathbf{k}_4$) for the case in which $\delta = 0$. The data points used to generate this figure were calculated by doing a numerical integration to determine κ_3 for the various angles. The integrations were done numerically by the computer since the analytic expression is not as accurate for large angles. Unfortunately this requires large amounts of computer time. The important observation to make is that for large φ, R is inversely proportional to the fourth power of $u_N \sin\varphi$, in excellent agreement with the work of Wandzura[13]. For small angles, Fig. 3.4 shows the normalized reflectivity versus sin φ for several values of the pump detuning δ. This figure disagrees with the results presented by Wandzura, who used a simple formula to interpolate between his results at $\varphi = 0°$ and at large angles. The narrow field of view shown in this figure is inherent to any Doppler broadened system as a result of the angular bandwidth's being inversely proportional to u_N. As δ increases, the field of view does increase, but this is realized only with a concomitant decrease in the absolute value of R, as shown in Fig. 3.5, where the reflection coefficient is plotted versus the detuning δ for the case in which

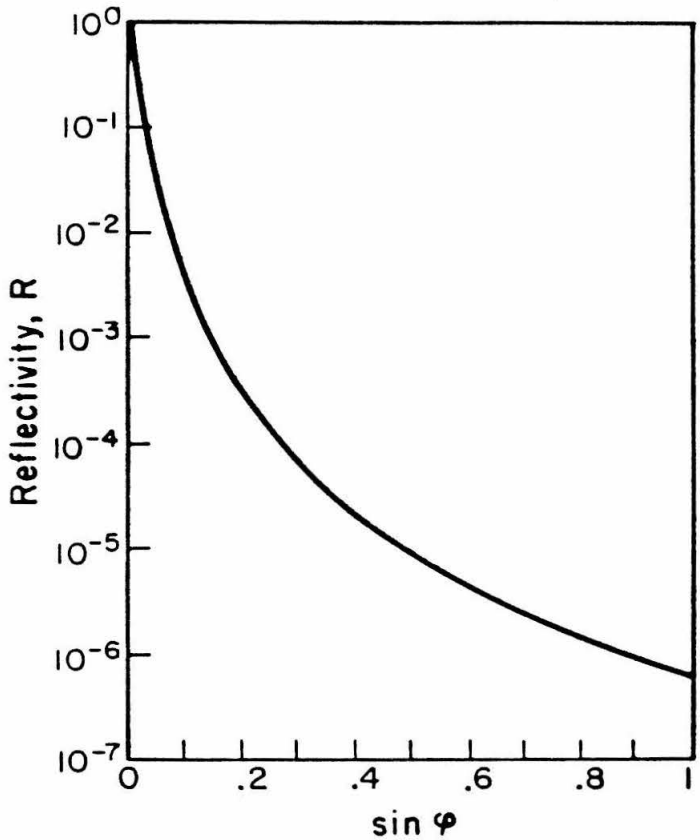

Fig. 3.3 Reflectivity versus $\sin\varphi$ for $\delta = 0$ and $\nu = 0$. The curve is normalized to unity at $\varphi = 0°$.

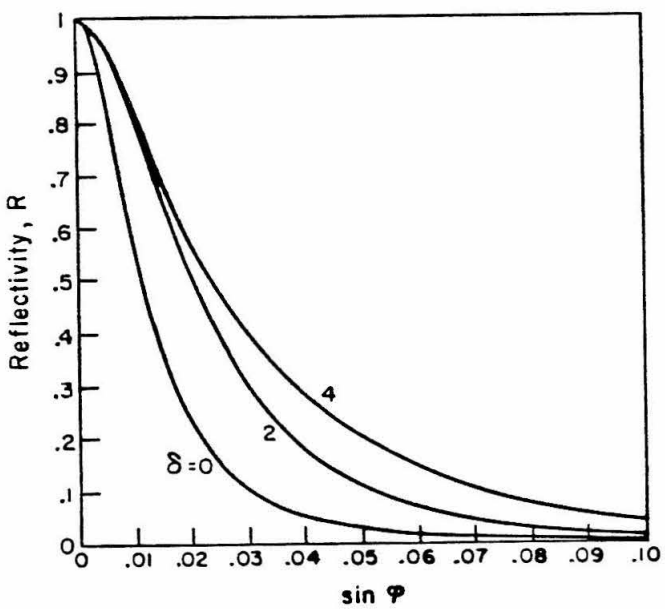

Fig. 3.4 Reflectivity for degenerate four-wave mixing versus sinφ for several values of the pump detuning δ. All curves are normalized to unity at $\varphi = 0°$.

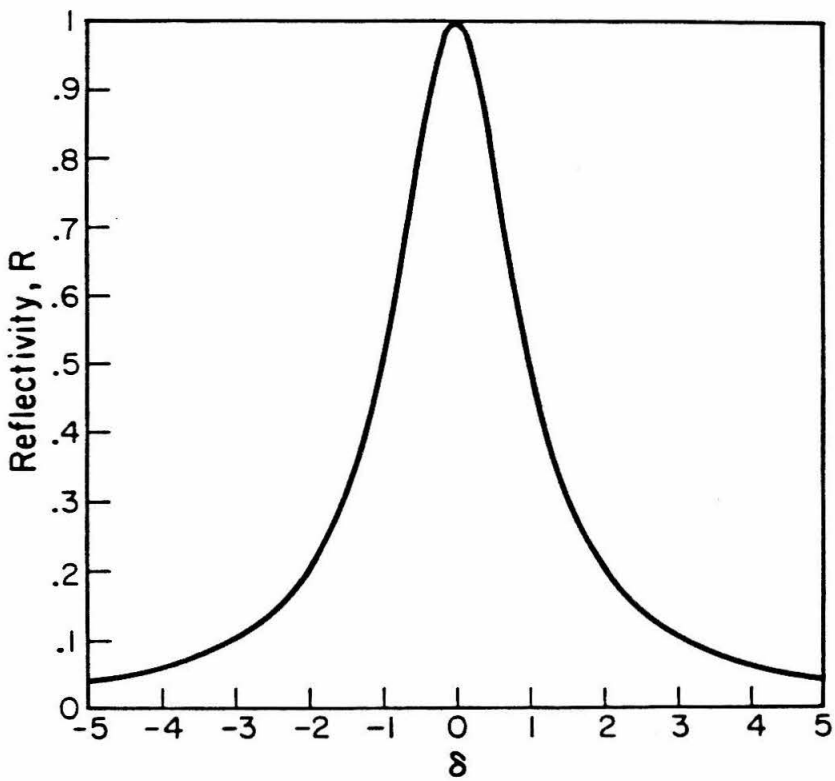

Fig. 3.5 Reflectivity for degenerate four-wave mixing versus pump detuning δ for the collinear case $\varphi = 0°$. The curve is normalized to unity at $\delta = 0$.

$\varphi = 0°$. From Fig. 3.5 , one notes that the reflectivity peaks on resonance, $\delta = 0$, and has a line shape determined by the homogeneous linewidth. Recent work by Elci and Rogovin[14] suggests that there should be a dip in the intensity of the phase conjugate wave at line center ($\delta = 0$). This prediction results from the incorrect method they used to include the effects of Doppler broadening on the third-order susceptibility. Elci and Rogovin account for the effects of Doppler motion by starting with $\chi^{(3)}$ calculated for a stationary atom. They replace ω with a Doppler-shifted frequency,$\omega - kv$ in $\chi^{(3)}$, and integrate $\chi^{(3)}$ over the velocity profile. Their method is basically incorrect because it does not allow for the different Doppler shifts that the two pump waves and the two signal waves are observed to have in the frame of the atom. The various Doppler shifts depend on the propagation direction of the waves relative to the velocity **v** of a given atom.

Since the reflectivity is the largest for the collinear geometry $\varphi = 0°$, the frequency dependence (filter function) of R in the nondegenerate case will be studied for that geometry. The pump waves are still assumed to be degenerate ($\varepsilon = 0$). Fig. 3.6 shows the reflection coefficient plotted versus signal detuning ν for several values of the pump detuning δ. As δ becomes larger, the reflectivity has a double-peaked structure with the two peaks occurring near $\nu = 0$ and $\nu = 2\delta$. This has been observed in some recent experiments[15] using sodium vapor as the Doppler-broadened medium. The resonance at $\nu = 0$ arises when the pump wave A_1 and the signal wave A_4 interact with the same velocity group of atoms while the resonance at $\nu = 2\delta$ occurs when the second pump wave A_2 interacts with the same velocity group as the signal wave A_4. This structure is shown better in Fig. 3.7 , where R, normalized to unity, is plotted versus $\nu - \delta$. This behavior is unique to a Doppler-broadened system and does not appear in a system of stationary atoms. The frequency response suggests that an active narrow-bandwidth optical filter can be constructed using a Doppler-broadened system. The bandwidth of the filter depends on the

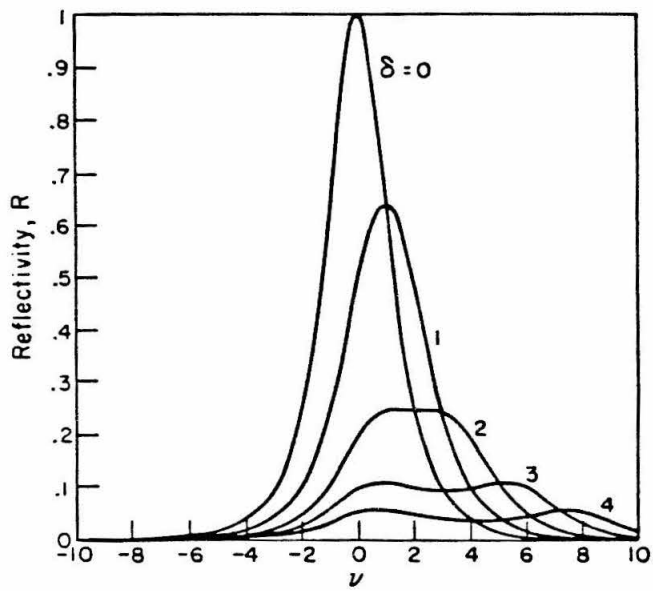

Fig. 3.6 Reflectivity versus signal detuning ν for several values of the pump detuning δ. The curves are normalized to $\delta = \nu = 0$.

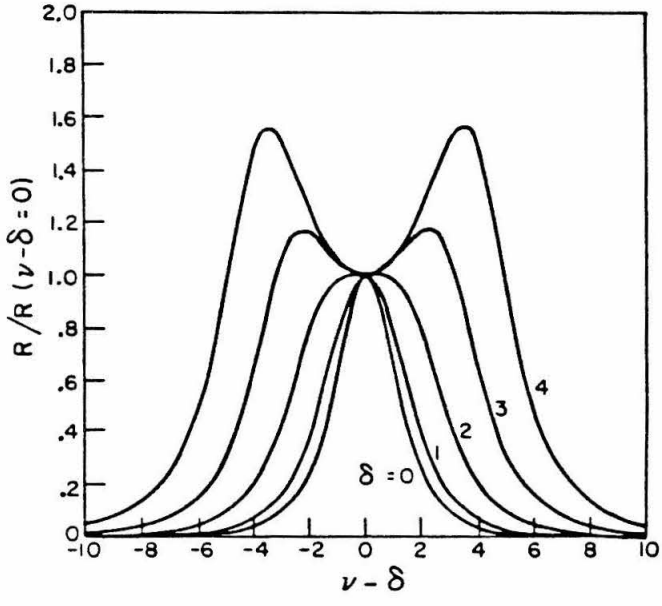

Fig. 3.7 Reflectivity versus the detuning $\nu - \delta$ for several values of the pump detuning δ. All curves are normalized to unity at $\nu - \delta = 0$.

homogeneous linewidth and monotonically increases with pump detuning δ.

We will now consider the effect of letting the pump waves be nondegenerate with each other as well as with the signal wave. We'll still consider a collinear geometry. Fig. 3.8 shows the normalized reflectivity versus signal detuning ν for several values of the pump detuning ε with $\delta = 0$. The important feature to notice is that the peak reflectivity is only slightly diminished as ε increases, with the peak occuring at $\nu = \varepsilon$. This corresponds to $\omega_4 = \omega_1$. Physically this situation represents the case where the pump waves and signal wave are all resonant with a class of atoms moving with velocity $\mathbf{v}_N = \varepsilon\, \mathbf{n}_4$ so in a frame moving with $\mathbf{v}_N = \varepsilon\, \mathbf{n}_4$ the situation is identical to that of degenerate pump waves with $\omega_1 = \omega_2 = \omega_0$. The decrease in reflectivity as ε increases is due to the decreased probability of an atom having velocity $\mathbf{v}_N = \varepsilon\, \mathbf{n}_4$. By comparison, Fig. 3.9 shows the normalized reflectivity versus $\nu - \delta$ for several values of the pump detuning δ with $\varepsilon = 0$. In this case, the pump frequencies are degenerate and the filter efficiency decreases very rapidly as δ is increased and the filter bandwidth also increases quite dramatically with δ. A comparison of these two figures shows how the use of nondegenerate pump frequencies can yield a narrow bandwidth optical filter which can be tuned over the Doppler profile without significant loss in efficiency.

In the non-collinear geometry, Fig. 3.10 shows the normalized reflectivity versus signal detuning ν for several values of $\sin\varphi$ with both pump waves tuned to line center, $\delta = \varepsilon = 0$. The bandwith increases as $u_N \sin(\varphi/2)$, as is evident from Eq. (3.3-6). The absolute value of the reflectivity decreases by a factor of ten from the collinear case for $\sin\varphi = .03$. This indicates that the field of view of the filter is very limited because of the Doppler broadening.[6,7] For $\sin\varphi = .03$, Fig. 3.11 plots the normalized reflectivity versus signal detuning ν for several values of pump detuning ε with $\delta = 0$. Comparison with Fig. 3.8 shows that the peak reflectivity also occurs at $\nu = \varepsilon$ with the bandwidth remaining a function of $\sin(\varphi/2)$ but being independent of

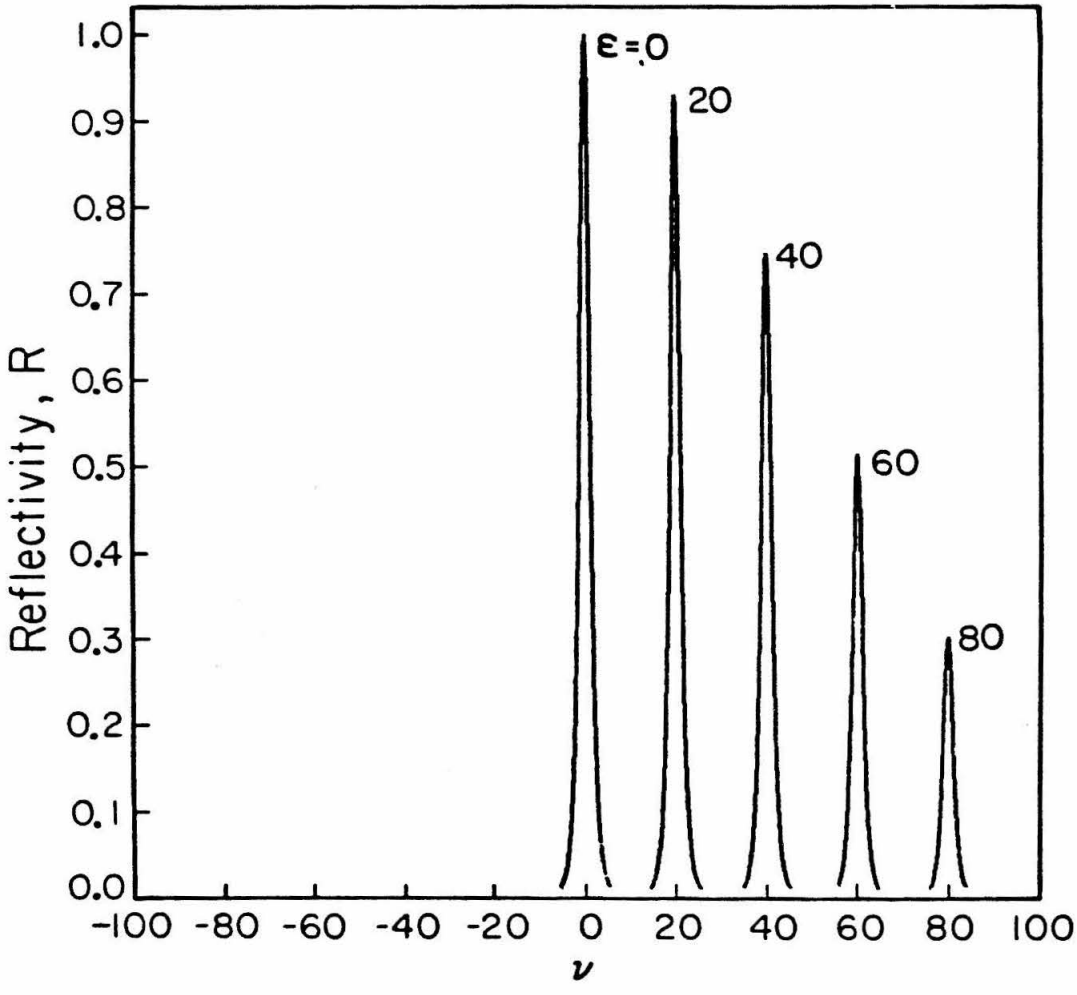

Fig. 3.8 Reflectivity versus signal detuning ν for several values of the pump detuning ε with $\delta = 0$ for the collinear case $\varphi = 0°$. All curves are normalized to $\varepsilon = \nu = 0$.

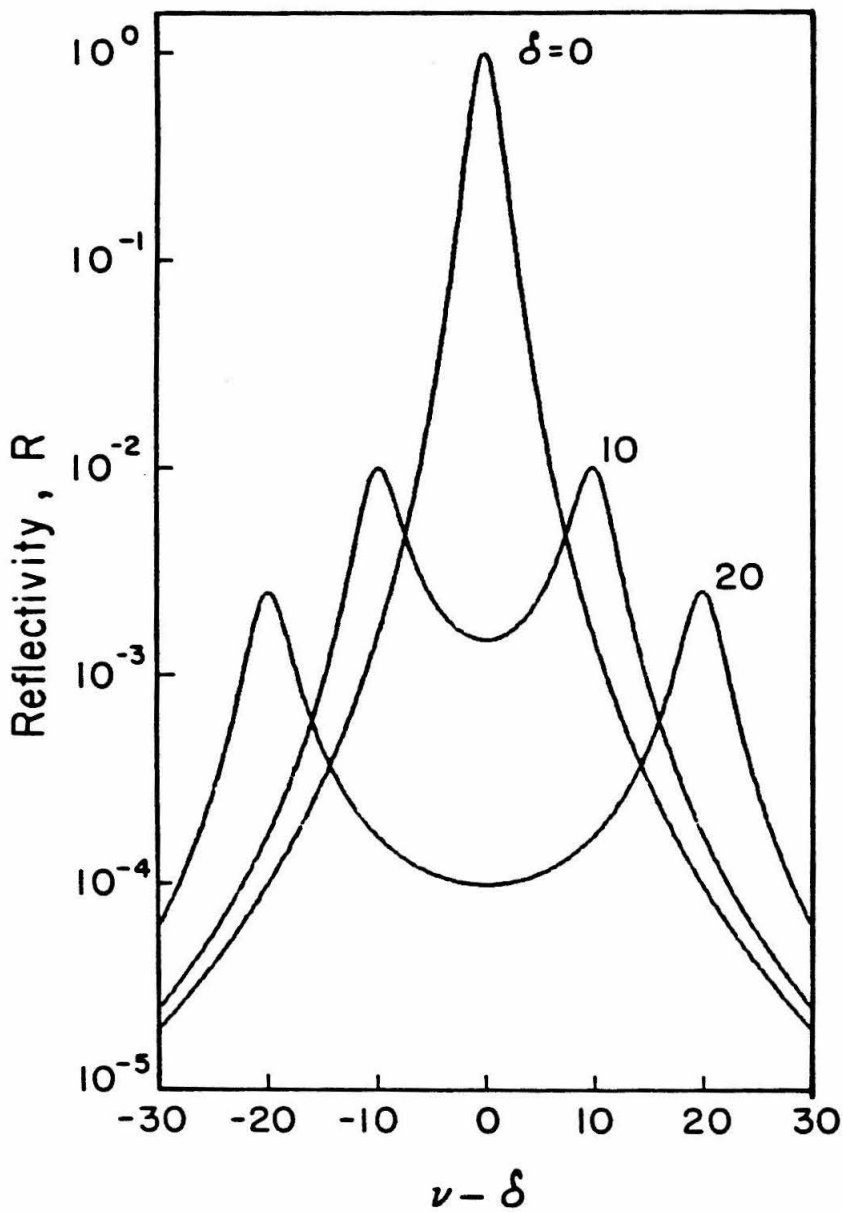

Fig. 3.9 Reflectivity versus the detuning $\nu - \delta$ for several values of the pump detuning δ with $\varepsilon = 0$ for the collinear case $\varphi = 0°$. The curves are normalized to $\nu = \delta = 0$.

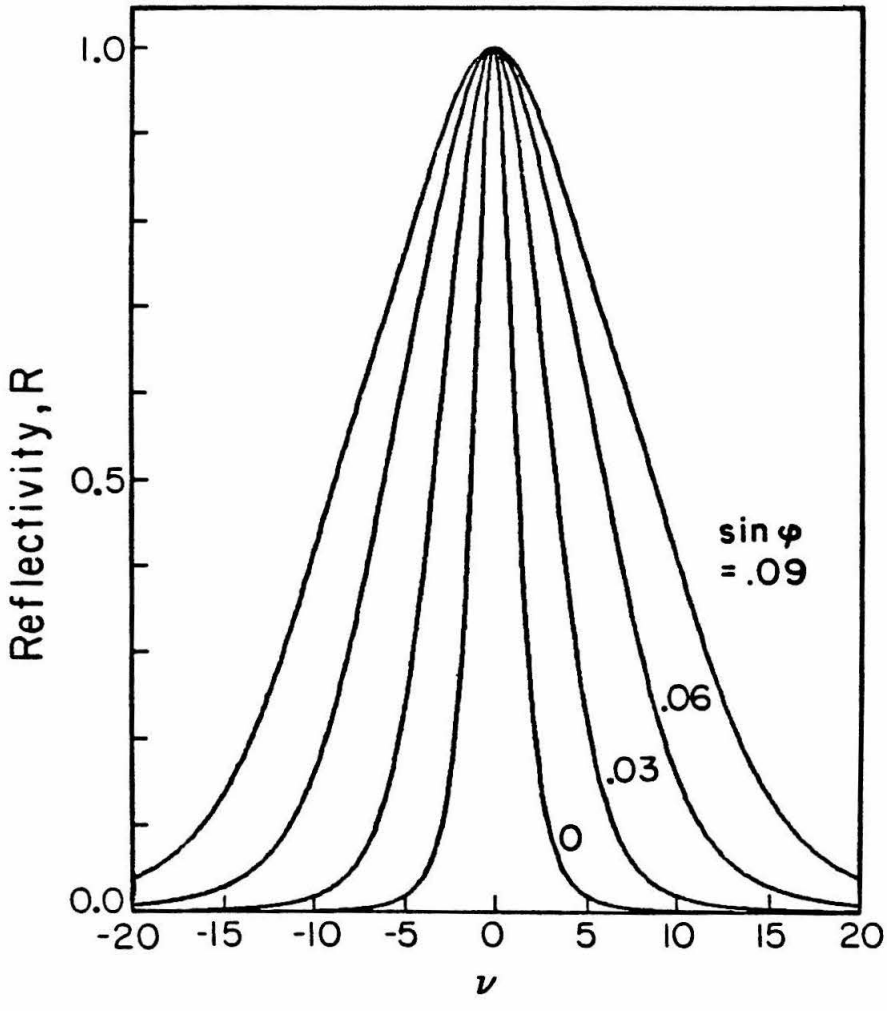

Fig. 3.10 Reflectivity versus signal detuning ν for several values of $\sin\varphi$. Both pump waves are tuned to line center, $\delta = \varepsilon = 0$. All curves are normalized to unity at $\nu = 0$.

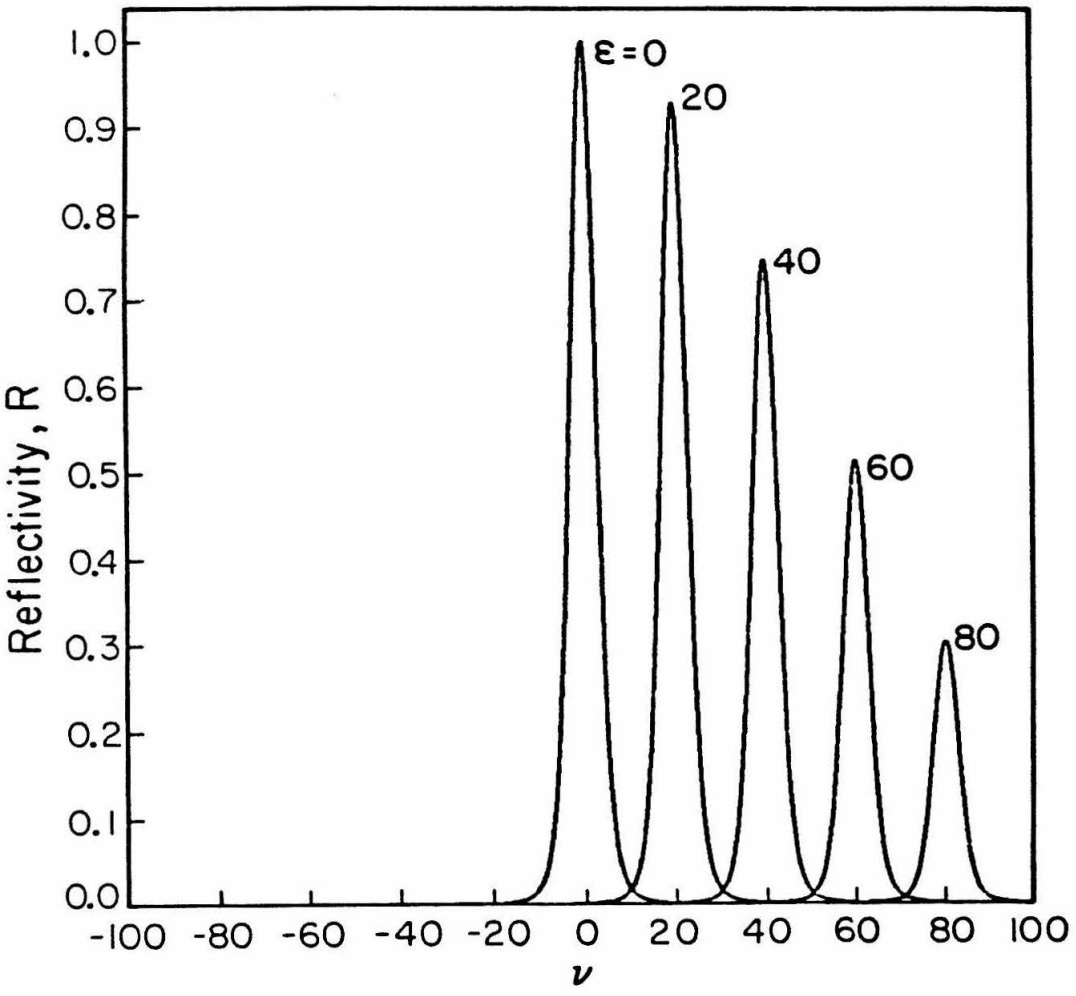

Fig. 3.11 Reflectivity versus signal detuning ν for several values of the pump detuning ε with $\delta = 0$ and $\sin\varphi = 0.03$. All curves are normalized to $\varepsilon = \nu = 0$.

ε.

3.5 A Modified Filter

Another interesting situation to consider is when one pump wave A_1 and the signal wave A_4 are fixed in frequency while the second pump wave A_2 is varied in frequency. As before, the phase conjugate signal A_3 will be counterpropagating to A_4 since we assume the two pump waves A_1 and A_2 are counterpropagating.

We will define $\delta_1 = (\omega_1 - \omega_0)T_2$, $\delta_2 = (\omega_2 - \omega_0)T_2$ and $\nu_1 = (\omega_4 - \omega_1)T_2$. All the previous definitions remain the same.

Only the collinear geometry will be considered since this has the greatest phase conjugate efficiency. The solutions for κ_i are given by

$$\kappa_4 = \alpha_0 \frac{A_1^* A_2^*}{E_s^2} \frac{\sqrt{\pi}}{u_N} \frac{1}{(1 - ia\nu_1)(\delta_1 + \delta_2 + \nu_1 + 2i)} \exp[-(\delta_2/u_N)^2],$$

$$\kappa_3^* = \alpha_0 \frac{A_1 A_2}{E_s^2} \frac{\sqrt{\pi}}{u_N} \frac{1}{(1 - ia\nu_1)(\delta_1 + \delta_2 - \nu_1 - 2i)} \exp[-(\delta_1/u_N)^2], \qquad (3.5\text{-}1)$$

For the case of a single input $A_4^*(0)$, with $A_3(L) = 0$, and using the parameters of the previous section, Fig. 3.12 shows the normalized reflectivity versus the pump detuning δ_2 for several values of δ_1 with $\nu_1 = 0$. This condition, $\nu_1 = 0$, corresponds to waves A_1 and A_4 being degenerate in frequency. The important observation to make is that the reflectivity has a peak at $\delta_2 = -\delta_1$. In a frame moving with $\mathbf{v}_N = \delta_1 \mathbf{n}_4$ the situation is identical to that of degenerate pump and signal waves with $\omega_1 = \omega_2 = \omega_3 = \omega_4 = \omega_0$.

In Fig. 3.13, $\delta_1 = 0$ and the normalized reflectivity is shown versus the pump detuning δ_2 for several values of ν_1. A peak occurs for $\delta_2 = \nu_1$ but the peak amplitude decreases rapidly with increased ν_1 and the bandwidth broadens considerably.

This filter arrangement has the advantage that one laser can provide the pump wave A_1 and the signal wave A_4. The second pump wave A_2 can be an external signal

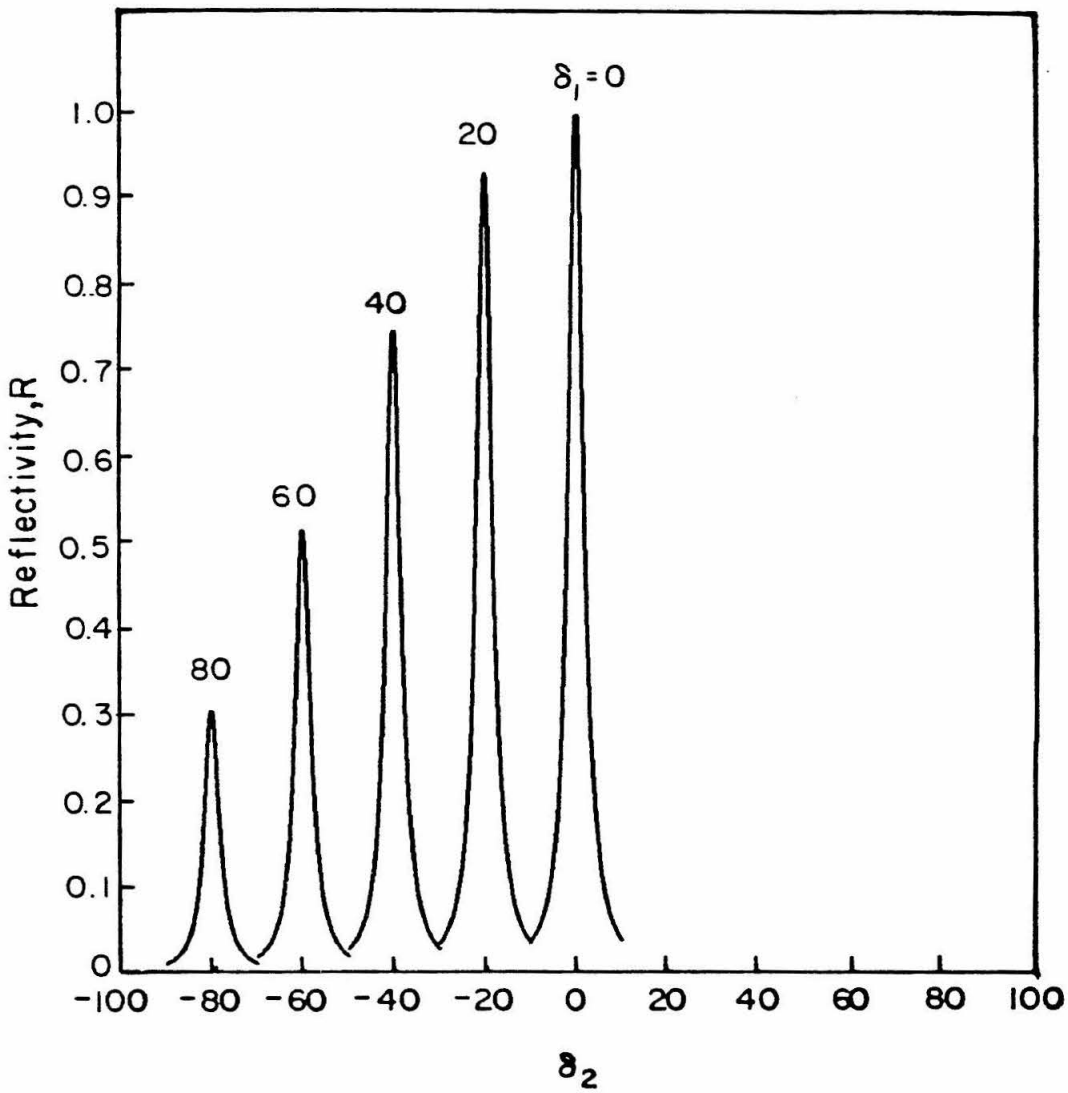

Fig. 3.12 Reflectivity versus pump detuning δ_2 for several values of the pump detuning δ_1 with $\nu_1 = 0$ for the collinear case $\varphi = 0°$. All curves are normalized to $\delta_1 = \delta_2 = 0$.

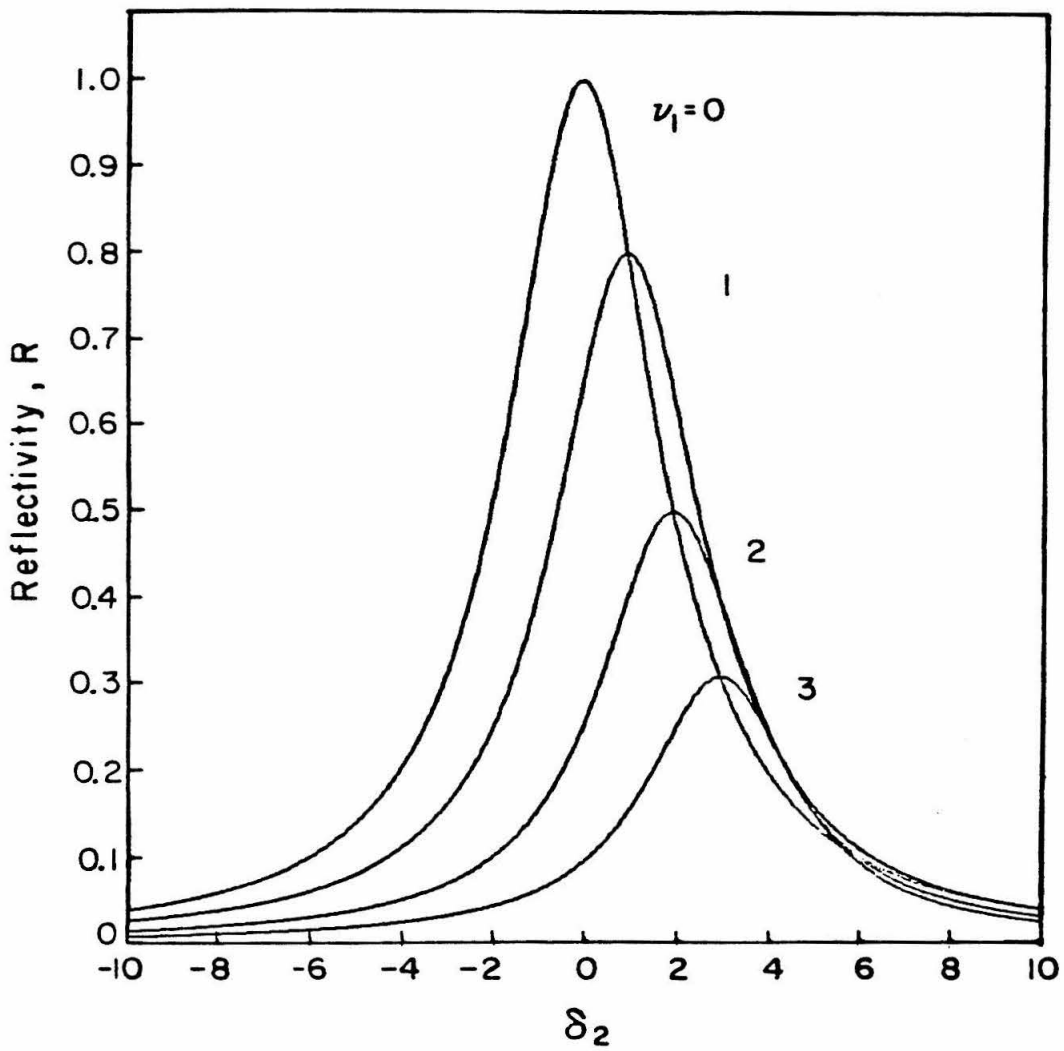

Fig. 3.13 Reflectivity versus the pump detuning δ_2 for several values of the signal detuning ν_1 with $\delta_1 = 0$ for the collinear case $\varphi = 0°$. The curves are normalized to $\delta_2 = \nu_1 = 0$.

which we are trying to filter. In an experimental arrangement, the wave A_4 can be at a very small angle to A_1 to provide isolation between the two waves. Spatial filtering of A_4 can help accomplish this. The filter can have an entrance aperture which forces the external signal to be counterpropagating to A_1. The central frequency of the filter's bandpass can be tuned over the Doppler profile with only a small decrease in efficiency as the waves become resonant with planes of atoms having nonzero velocity. We will then have an efficient tunable narrow-bandwidth optical filter which is highly directional.

The filter described in the last section required two lasers to provide the pump waves, or some other means to provide the two frequencies needed by the pump waves, if we desired to tune the central bandpass of the filter over the Doppler profile. However this filter has the advantage of phase conjugating the external signal which is being filtered. This allows the use of optical systems, such as those discussed in section 2.4, to obtain good signal to noise for the filter. The filter discussed in this section would not have that property.

3.6 Conclusion

The primary effects of Doppler broadening are to reduce the effective absorption cross section and to impart an angular dependence to the reflection coefficient. The angular dependence would severely limit the field of view of devices based on this system. However, it is important to note that the linewidth of the reflection coefficient approaches the homogeneous linewidth at small angles.

The frequency response of the Doppler-broadened system in the nondegenerate case demonstrates how four-wave mixing can yield an active narrow-bandwidth optical filter. In the case of degenerate pump waves, the filter has a bandpass which is centered at the line-center frequency of the two-level system and whose bandwidth is limited by the homogeneous linewidth. However, by using pump waves of different

frequencies the optical filter demonstrated has a tuning range which extends over the whole Doppler profile while still maintaining the same narrow linewidth and with only a small reduction in efficiency as compared to line center operation.

References for Chapter III

1. J. Nilsen, N. S. Gluck, and A. Yariv, "Narrowband optical filter via phase conjugation by nondegenerate four-wave mixing in sodium vapor," Opt. Lett. 6,380 (1981).

2. L. M. Humphrey, J. P. Gordon, and P. F. Liao, "Angular dependence of line shape and strength of degenerate four-wave mixing in a Doppler-broadened system with optical pumping," Opt. Lett. 5,56 (1980)

3. P. F. Liao, D. M. Bloom, and N. P. Economou, "CW optical wave-front conjugation by saturated absorption in atomic sodium vapor," Appl. Phys. Lett. 32,813 (1978)

4. D. Grischkowsky, N. S. Shiren, and R. J. Bennett, "Generation of time-reversed wave fronts using a resonantly enhanced electronic nonlinearity," Appl. Phys. Lett. 33,805 (1978).

5. R. C. Lind, D. G. Steel, M. B. Klein, R. L. Abrams, C. R. Giuliano, and R. K. Jain, "Phase conjugation at 10.6μm by resonantly enhanced degenerate four-wave mixing," Appl. Phys. Lett. 34,457 (1979).

6. J. Nilsen and A. Yariv, "Nondegenerate four-wave mixing in a Doppler-broadened resonant medium," J.Opt.Soc.Am. 71,180 (1981).

7. Joseph Nilsen and Amnon Yariv, "A tunable narrowband optical filter via phase conjugation by nondegenerate four-wave mixing in a Doppler-broadened resonant medium," Opt. Comm. 39,199 (1981).

8. A. Yariv, **Quantum Electronics** (Wiley, New York, 1975), pp. 149-155, 418-421, 553-558.

9. A. Yariv and D. M. Pepper, "Amplified reflection, phase conjugation, and oscillation in degenerate four-wave mixing," Opt. Lett. 1,16 (1977).

10. B. D. Fried and S. D. Conte, **The Plasma Dispersion Function** (Academic Press, New York, 1961)

11. M. Abramowitz and I. A. Stegun, **Handbook of Mathematical Functions** (Dover, New York, 1965), pp. 931,932.

12. J. Nilsen, N. S. Gluck, and A. Yariv, 'Narrowband optical filter via phase conjugation by nondegenerate four-wave mixing in sodium vapor," Opt. Lett.,to be published.

13. S. M. Wandzura, 'Effects of atomic motion on wavefront conjugation by resonantly enhanced degenerate four-wave mixing," Opt. Lett. 4,208 (1979).

14. A. Elci and D. Rogovin, 'Phase conjugation in an inhomogeneously broadened medium," Opt. Lett. 5,255 (1980).

15. D. G. Steel and R. C. Lind, 'Multiresonant behavior in nearly degenerate four-wave mixing: the ac Stark effect," Opt. Lett. 6,587 (1981).

Chapter IV

NONDEGENERATE FOUR-WAVE MIXING IN A HOMOGENEOUSLY BROADENED TWO-LEVEL SYSTEM WITH SATURATING PUMP WAVES

4.1 Introduction

The last two chapters have dealt with phase conjugation via nondegenerate four-wave mixing in a homogeneously broadened two-level system and then extended this treatment to include an inhomogeneously broadened system. In both cases the solutions to the density matrix equations have been obtained by perturbation theory carried out to third-order[1-3]. In this chapter we will again consider the homogeneously broadened system but will generalize the solution to include all orders of the amplitudes of the strong pump fields and first-order in the amplitudes of the weak signal fields. As discussed briefly in section 1.5, Abrams and Lind[4,5] have considered this problem for degenerate four-wave mixing. Several other authors[6,7] have considered various aspects of the solution for the nondegenerate case.

4.2 Solving the Density Matrix Equations

As before the mixing involves two intense counterpropagating pump waves E_1 and E_2 of the same frequency ω and two weak counterpropagating waves E_3 and E_4 with frequencies ω_3 and ω_4. The geometry of Yariv and Pepper[8] shown in Figure 2.2 is used.

The fields are taken as plane waves:

$$E_i(r_i,t) = \tfrac{1}{2}A_i(r_i)\exp[i(\omega_i t - \mathbf{k}_i\cdot\mathbf{r})] + \text{c.c.}, \tag{4.2-1}$$

where r_i is the distance along $\mathbf{k}_i$. We have

$$\mathbf{k}_1 + \mathbf{k}_2 = 0, \quad \omega_3 + \omega_4 = 2\omega. \tag{4.2-2}$$

The density matrix equations are then solved to all orders in the amplitudes of the pump waves and first-order in the amplitudes of the weak signal fields. The solution is found by taking the Fourier transform of the density matrix equations

$$\frac{d\rho_{21}}{dt} = -i\omega_0\rho_{21} + i\frac{\mu}{\hbar}E(\mathbf{r},t)(\rho_{11} - \rho_{22}) - \frac{\rho_{21}}{T_2}$$

$$\frac{d}{dt}(\rho_{11} - \rho_{22}) = 2i\frac{\mu}{\hbar}E(\mathbf{r},t)\,(\rho_{21} - \rho_{21}^*) - \frac{(\rho_{11} - \rho_{22}) - (\rho_{11} - \rho_{22})_0}{T_1}. \qquad (4.2\text{-}3)$$

This is done by letting

$$\rho_{11} - \rho_{22} = \rho_0 + \rho_A e^{i(\omega - \omega_4)t} + \rho_A^* e^{-i(\omega - \omega_4)t}$$

$$+ \rho_B e^{i(\omega - \omega_3)t} + \rho_B^* e^{-i(\omega - \omega_3)t}$$

$$\rho_{21} = \sigma_A e^{-i\omega t} + \sigma_B e^{-i\omega_4 t} + \sigma_C e^{-i\omega_3 t} \qquad (4.2\text{-}4)$$

Substituting in Eqs. (4.2-3),equating the coefficients of the Fourier components, and neglecting higher order terms in the signal waves A_3 and A_4 we can determine the induced polarizations at ω_3 and ω_4.

$$P(\omega_3 = 2\omega - \omega_4, \mathbf{k}_1\cdot\mathbf{r}) = \frac{c}{4\pi\omega_3}\{-i\alpha_3(\mathbf{k}_1\cdot\mathbf{r})A_3 + \kappa_3^*(\mathbf{k}_1\cdot\mathbf{r})A_4^* exp[i(\Delta k)z]\}$$

$$\times exp[i(\omega_3 t - \mathbf{k}_3\cdot\mathbf{r})].$$

$$P(\omega_4 = 2\omega - \omega_3, \mathbf{k}_1\cdot\mathbf{r}) = \frac{c}{4\pi\omega_4}\{-i\alpha_4(\mathbf{k}_1\cdot\mathbf{r})A_4 + \kappa_4^*(\mathbf{k}_1\cdot\mathbf{r})A_3^* exp[i(\Delta k)z]\}$$

$$\times exp[i(\omega_4 t - \mathbf{k}_4\cdot\mathbf{r})]. \qquad (4.2\text{-}5)$$

The coupling constants appearing in Eqs. (4.2-5) are given by

$$\alpha_3(\mathbf{k}_1\cdot\mathbf{r}) = \frac{-i\alpha_0}{(\delta - \nu - i)\left[1 + \frac{A^*A}{E_s^2(1 + \delta^2)}\right]}$$

$$\times \left[1 - \frac{\dfrac{A^*A(2 - i\nu)}{2E_s^2(1 - ia\nu)(1 - i\delta)[1 + i(\delta - \nu)]}}{\left[1 + \dfrac{A^*A(1 - i\nu)}{E_s^2(1 - ia\nu)[1 + i(\delta - \nu)][1 - i(\delta + \nu)]}\right]} \right]$$

$$\alpha_4^*(\mathbf{k}_1 \cdot \mathbf{r}) = \frac{i\alpha_0}{(\delta + \nu + i)\left[1 + \dfrac{A^*A}{E_s^2(1 + \delta^2)}\right]}$$

$$\times \left[1 - \frac{\dfrac{A^*A(2 - i\nu)}{2E_s^2(1 - ia\nu)(1 + i\delta)[1 - i(\delta + \nu)]}}{\left[1 + \dfrac{A^*A(1 - i\nu)}{E_s^2(1 - ia\nu)[1 + i(\delta - \nu)][1 - i(\delta + \nu)]}\right]} \right]$$

$$\kappa_3^*(\mathbf{k}_1 \cdot \mathbf{r}) = 2\alpha_0 \left[\frac{[1 - (i\nu)/2]}{(\delta - i)(1 - ia\nu)(\delta - \nu - i)(\delta + \nu + i)} \right] \cdot \frac{A_1 A_2}{E_s^2} \cdot \frac{1}{S}$$

$$\kappa_4(\mathbf{k}_1 \cdot \mathbf{r}) = 2\alpha_0 \left[\frac{[1 - (i\nu)/2]}{(\delta + i)(1 - ia\nu)(\delta - \nu - i)(\delta + \nu + i)} \right] \cdot \frac{A_1^* A_2^*}{E_s^2} \cdot \frac{1}{S}$$

$$S = \left[1 + \frac{A^*A}{E_s^2(1 + \delta^2)} \right]$$

$$\times \left[1 + \frac{A^*A(1 - i\nu)}{E_s^2(1 - ia\nu)[1 - i(\delta + \nu)][1 + i(\delta - \nu)]} \right] \qquad (4.2\text{-}6)$$

with

$$A = A_1 e^{-i\mathbf{k}_1 \cdot \mathbf{r}} + A_2 e^{-i\mathbf{k}_2 \cdot \mathbf{r}} \qquad (4.2\text{-}7)$$

and where $\delta = (\omega - \omega_0)T_2$ is the normalized detuning of the pump frequency from line center, $\nu = (\omega_4 - \omega)T_2$ is the normalized detuning of the signal frequency from the pump frequency, $a = T_1/T_2$, $E_s^2 = \hbar^2/T_1T_2\mu^2$ is the line-center saturation intensity, $\alpha_0 = 4\pi\mu^2\Delta N_0 T_2 k_0/2\hbar$ is the line-center homogeneous-broadening absorption coefficient of the subject gas, k_0 is the magnitude of the wave number at frequency ω_0, and $\Delta k = 2(\omega_4 - \omega)/c$.

The coupling coefficients have a DC spatial component as well as high frequency spatial components due to the A^*A term in each coupling coefficient. Only the DC

component of the coupling coefficients is phase matched and therefore of any importance in the coupled mode equations. Defining

$$A_1 = |A_1|e^{i\vartheta_1} \qquad A_2 = |A_2|e^{i\vartheta_2}$$

$$I_1 = \frac{|A_1|^2}{E_s^2} \qquad I_2 = \frac{|A_2|^2}{E_s^2} \tag{4.2-8}$$

we obtain

$$\frac{A^*A}{E_s^2} = I_1 + I_2 + 2\sqrt{I_1 I_2}\cos(x + \vartheta) \tag{4.2-9}$$

with $x = 2\mathbf{k}_1 \cdot \mathbf{r}$ and $\vartheta = \vartheta_2 - \vartheta_1$.

We can now determine the DC spatial component of α_i, κ_i by integrating over x.

$$\alpha_3 = \frac{1}{2\pi}\int_0^{2\pi} \alpha_3(x)\,dx$$

$$\alpha_4^* = \frac{1}{2\pi}\int_0^{2\pi} \alpha_4^*(x)\,dx$$

$$\kappa_3^* = \frac{1}{2\pi}\int_0^{2\pi} \kappa_3^*(x)\,dx$$

$$\kappa_4 = \frac{1}{2\pi}\int_0^{2\pi} \kappa_4(x)\,dx \tag{4.2-10}$$

4.3 Coupled Mode Equations

The values of α_i and κ_i calculated in Eqs. (4.2-10) can now be used in the coupled mode equations

$$\frac{dA_3}{dz} = \alpha_3 A_3 + i\kappa_3^* A_4^* \exp[i(\Delta k)z],$$

$$\frac{dA_4^*}{dz} = -\alpha_4^* A_4^* + i\kappa_4 A_3 \exp[-i(\Delta k)z]\,. \tag{4.3-1}$$

The solutions to the above equations, given in Chapter II by Eqs. (2.4-13), describe the evolution of waves A_3 and A_4^*.

We will study the dependence of the reflected signal on the various parameters such as frequency, linear absorption and pump intensity for the case of a single input wave $A_4^*(0)$. As defined previously in Eq. (2.4-16) the reflectivity R is

$$R = |A_3(0)|^2 / |A_4(0)|^2. \tag{4.3-2}$$

with its solution given by Eq. (2.4-17).

First we will investigate the degenerate case and discuss several new phenomena which are predicted by our solution for R. This will be followed by an analysis of the nondegenerate case and a discussion of a variety of interesting phenomena associated with it.

4.4 Degenerate Four-Wave Mixing

In the degenerate case, $\nu = 0$, Eqs. (4.2-6) are greatly simplified. These solutions for κ_i and α_i reduce to those of Abrams and Lind[4,5] for the degenerate case of two equal intensity pump waves. The first part of the discussion will deal with maximizing the efficiency of the phase conjugate process. Then we will discuss several new phenomena which are predicted by our solution for R.

Let us initially consider the case of equal intensity pump waves with $I_1 = I_2 = I$. Using Eqs. (4.2-10) to calculate κ^* we obtain

$$\kappa^* = 2\alpha_0 \frac{\delta + i}{(1 + \delta^2)^{1/2}} \frac{I}{(1 + \delta^2 + 4I)^{3/2}} \tag{4.4-1}$$

For $\nu = 0$, we also note that $\kappa_3 = \kappa_4 = \kappa$ and $\alpha_3 = \alpha_4 = \alpha$. Using Eq. (4.4-1), $|\kappa|$ can be maximized as a function of I for various values of δ. Taking the derivative of κ with respect to I and setting this equal to zero we obtain a value of $I = \frac{1 + \delta^2}{2} \equiv I_{max}$ as the value of I which maximizes $|\kappa|$. For small $\alpha_R L$, $R \approx |\kappa L|^2$ and we expect R to achieve a maximum value when $|\kappa|$ does. For large $\alpha_R L$, R has a more complicated dependence and may not have its peak exactly at $I = I_{max}$.

In Fig. 4.1 we show the I dependence of the reflectivity R by plotting R versus I for $\delta = 8$ and several values of $\beta_0 L$. β_0 is the unsaturated off resonance absorption coefficient and is defined by

$$\beta_0 = \frac{\alpha_0}{1 + \delta^2}. \tag{4.4-2}$$

For $\delta = 8$, we can calculate $I_{max} = 32.5$. Looking at Fig. 4.1, we observe that the reflectivity peaks near I_{max} and the value of I at the peak increases slightly with increasing $\beta_0 L$. For $\beta_0 L = 1$, the reflectivity has a peak value of R = 11, which indicates that we are in the gain regime.

To further consider the requirements for achieving gain in this system, Fig. 4.2 shows the reflectivity R plotted versus $\beta_0 L$ for several values of δ. For each value of δ, I is chosen equal to I_{max}. The interesting thing to observe is that there is no gain for $\delta = 0$ but as δ increases we observe gain and then oscillation. The oscillation becomes periodic as shown for $\delta = 8$. The important conclusion to draw is that the pump waves should be detuned from line center to achieve maximum efficiency.

To demonstrate power broadening of the reflectivity, Fig 4.3 has R plotted versus δ for several values of I with $\alpha_0 L = 1$. The curves are all normalized to unity at $\delta = 0$. As I increases we observe that the bandwidth of R increases as the square root of I. This is for the case $R < 1$ and demonstrates the power broadening of κ.

The first new phenomenon we have observed is a dip in the reflectivity at $\delta = 0$ when R is plotted versus δ. This is shown in Fig. 4.4 where we have a series of plots of R versus δ for I = 100 and six different values of $\alpha_0 L$. All the curves are normalized to unity at their maximum. The magnitude of the dip increases for increasing α_0.

To explain this phenomenon recall that the reflectivity R can be approximated by

$$R \approx |\kappa_3 L|^2 (1 - e^{-2\alpha_R L})^2 / 4\alpha_R^2 L^2 \tag{4.4-3}$$

with $2\alpha_R = \mathrm{Re}(\alpha_3 + \alpha_4^*)$ for $R < 1$. For small $\alpha_R L < 1$, $R \approx |\kappa L|^2$ but for large $\alpha_R L > 1$,

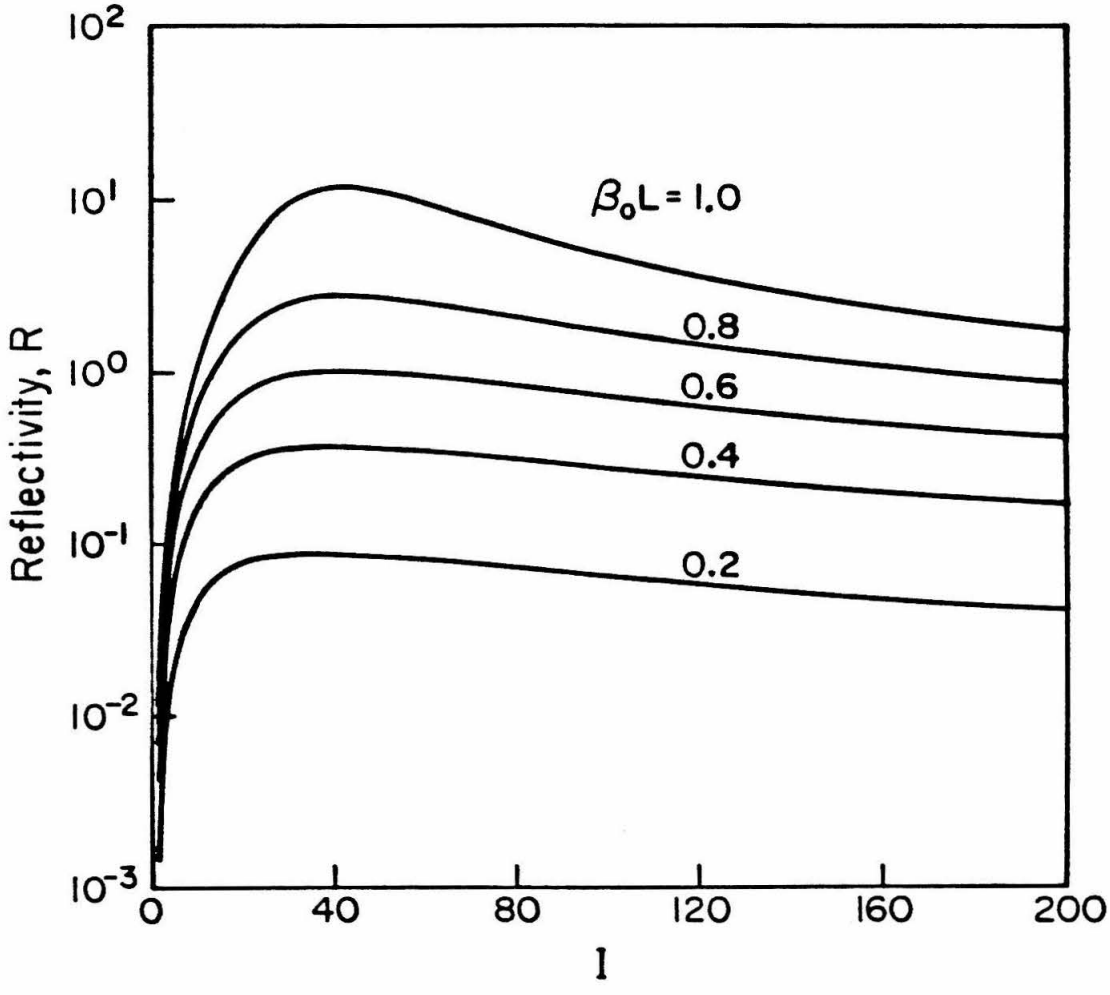

Fig. 4.1 Reflectivity versus the pump intensity I for $\delta = 8$ and several values of $\beta_0 L$.

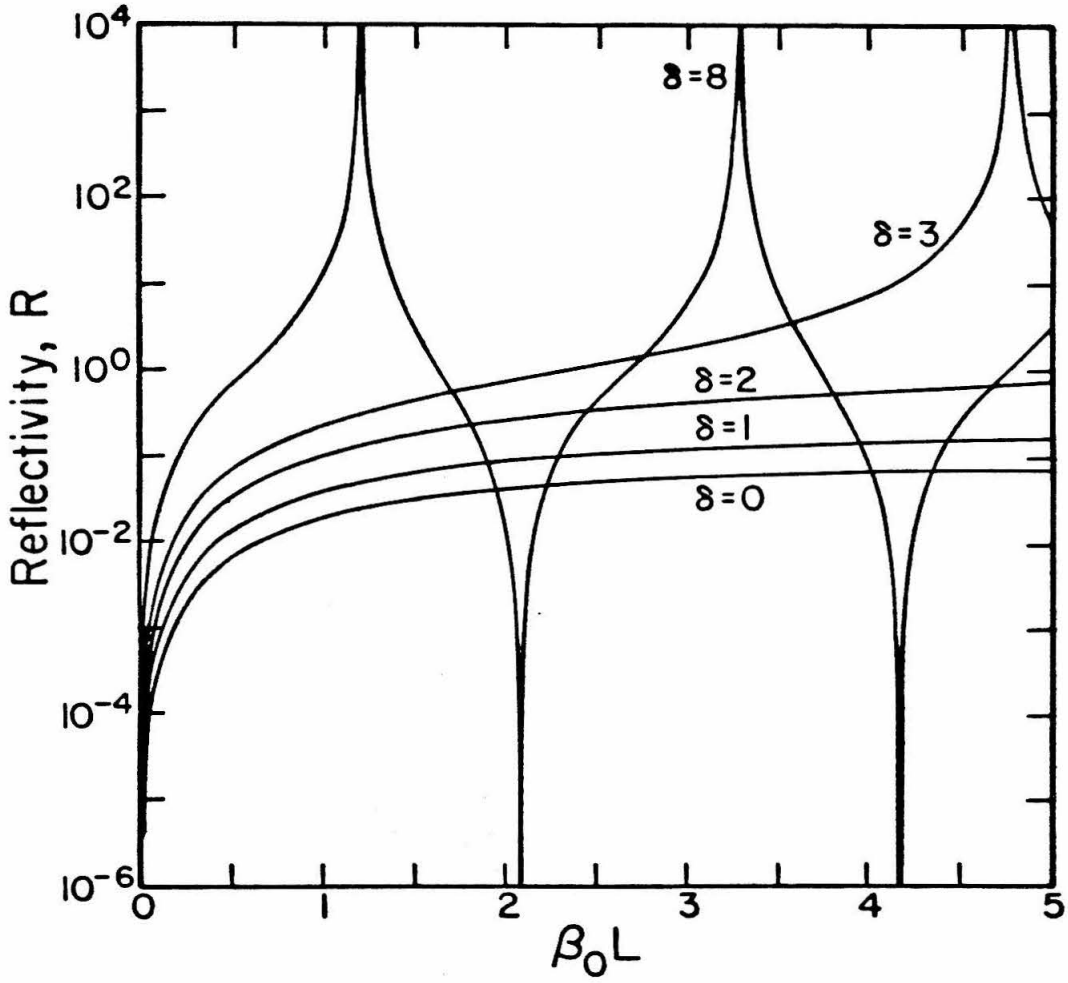

Fig. 4.2 Reflectivity versus the absorption coefficient $\beta_0 L$ for several values of δ. I is chosen equal to I_{max} for each δ.

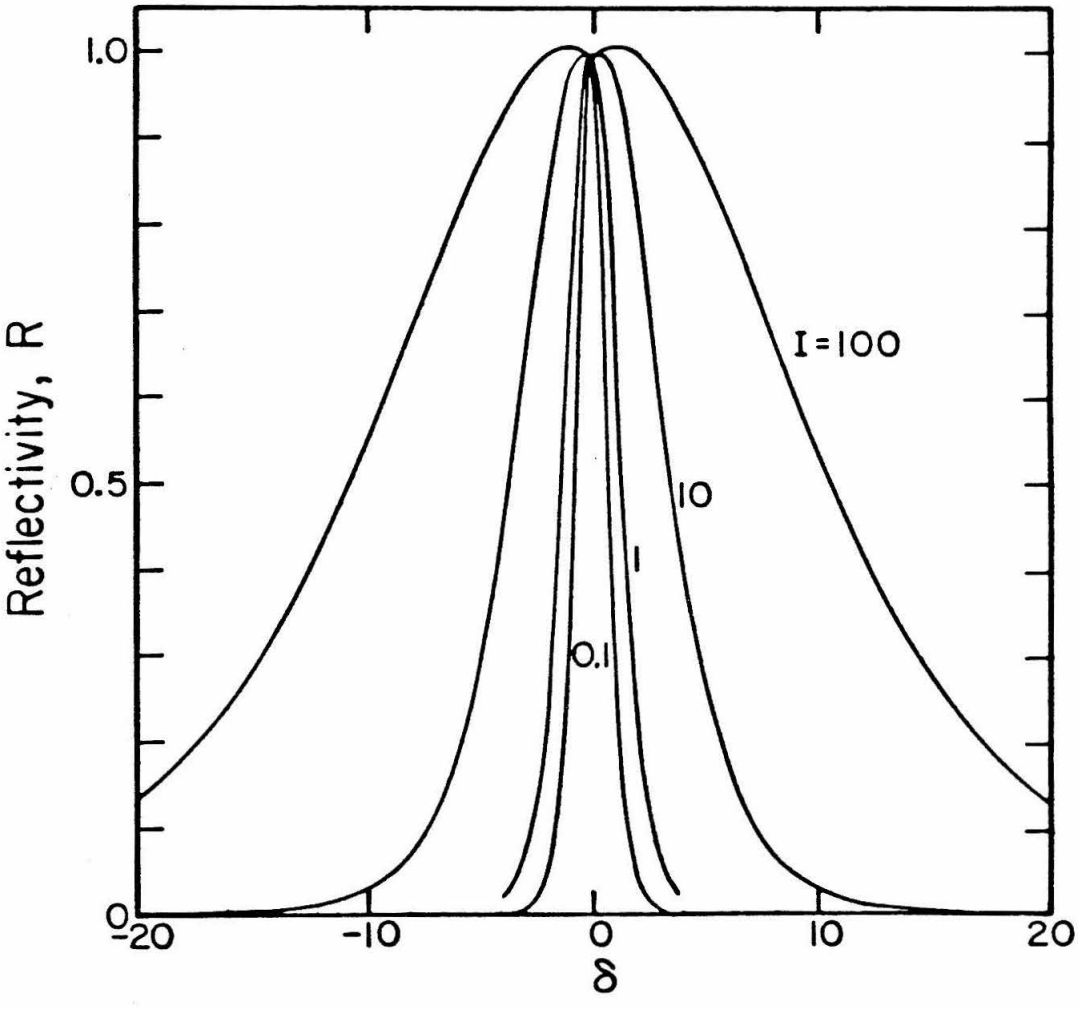

Fig. 4.3 Reflectivity versus the pump detuning δ for several values of I. All the curves are normalized to unity at $\delta = 0$.

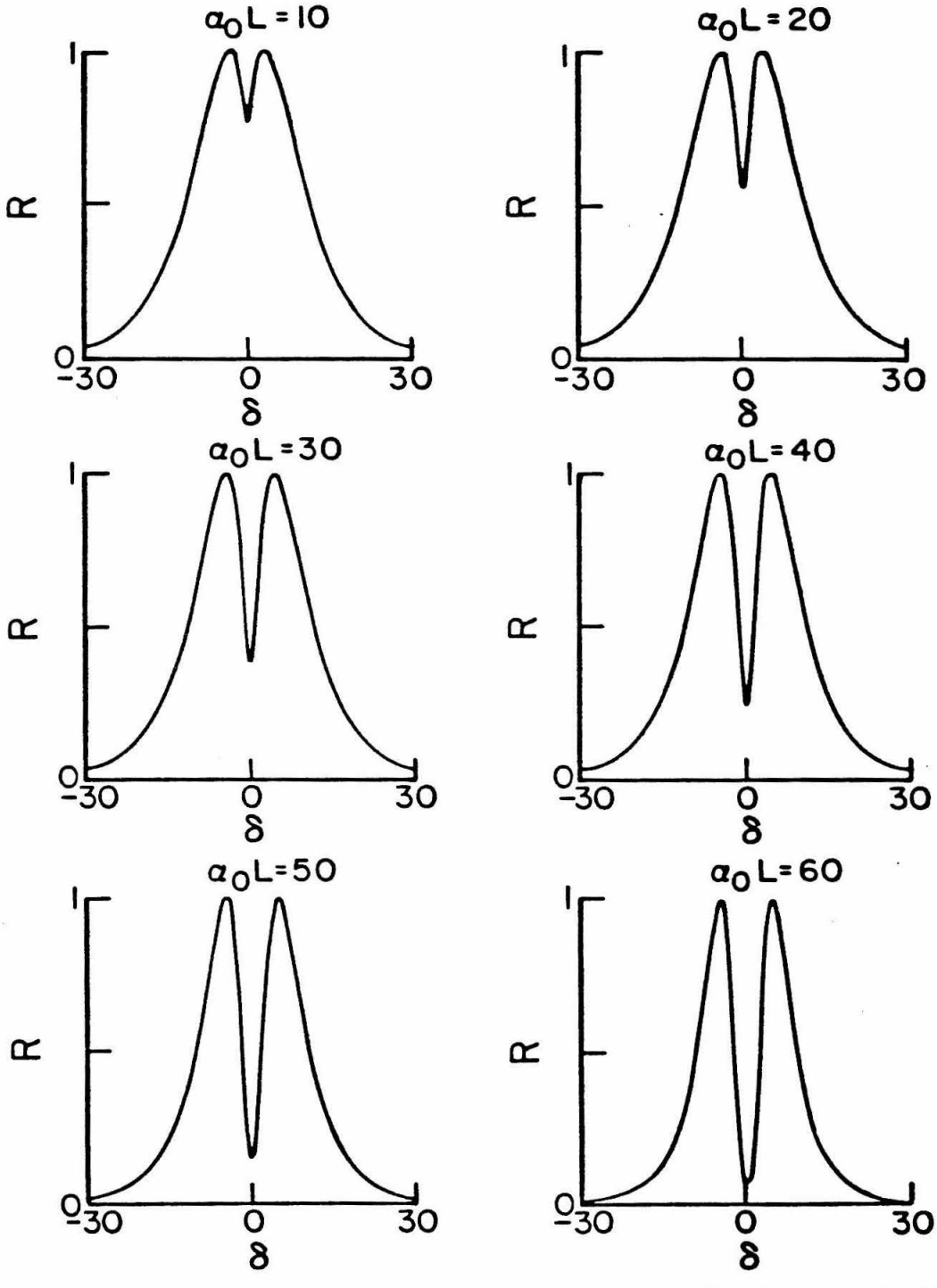

Fig. 4.4 Reflectivity versus the pump detuning δ for several values of $\alpha_0 L$. All the curves are normalized to unity at their maxima.

$R \approx |\frac{\kappa}{2\alpha_R}|^2$. Now $|\kappa|$ and α_R both peak at $\delta = 0$, but suppose α_R is a more sharply peaked function than $|\kappa|$. If at $\delta = 0$, $\alpha_R L$ is larger than unity then $R \approx |\frac{\kappa}{2\alpha_R}|^2$. As $|\delta|$ is increased the reflectivity will initially increase because α_R will decrease faster than $|\kappa|$. Eventually $|\delta|$ will increase to the point that $\alpha_R L < 1$, implying $R \approx |\kappa L|^2$ and R will then decrease with increasing $|\delta|$. The net result will be a dip at $\delta = 0$ whose magnitude depends both on the relative dependences of κ and α_R on δ and the value of $\alpha_R L$ at $\delta = 0$. The important criterion for observing a dip is that α_R be more sharply peaked than κ around $\delta = 0$.

In Fig. 4.5, $|\kappa|$ and α_R are both plotted versus δ for various values of I. The curves are all normalized to unity at $\delta = 0$. In the unsaturated regime, $I < 1$, α_R is broader than $|\kappa|$ in its response. However, for $I = 1$ the responses are roughly the same and as we go into the saturated regime, $I > 1$, α_R becomes more sharply peaked than $|\kappa|$ and the differences in the responses increases with I. Therefore, in the saturated regime we would expect to see the dips shown in Fig. 4.4.

The second new phenomenon we have observed is a dip in the reflectivity at $\delta = 0$ due to an asymmetry in the pump wave intensities. This is shown in Fig. 4.6 where the reflectivity R is plotted versus δ for various values of I_1. The product $I_1 \cdot I_2 = 10^4$ is kept constant and $\alpha_0 L = 1$. The curves are normalized to unity for $I_1 = 100$, $\delta = 0$. As the asymmetry in the amplitudes of the pump waves increases we observe a decrease in the amplitude of R and a dip at $\delta = 0$. We have chosen $\alpha_0 L = 1$ to distinguish this phenomenon from the previous one by insuring that we are in the regime where $R \approx |\kappa L|^2$. To better demonstrate this, Fig. 4.7 shows $|\kappa|$ plotted versus δ for the same values of I_1. Again, the curves are normalized to unity at $I_1 = 100$ and $\delta = 0$. The response of $|\kappa|$ is quite similar to R as we would expect. We can conclude that this phenomenon results from the manner in which the asymmetric pump waves affect κ.

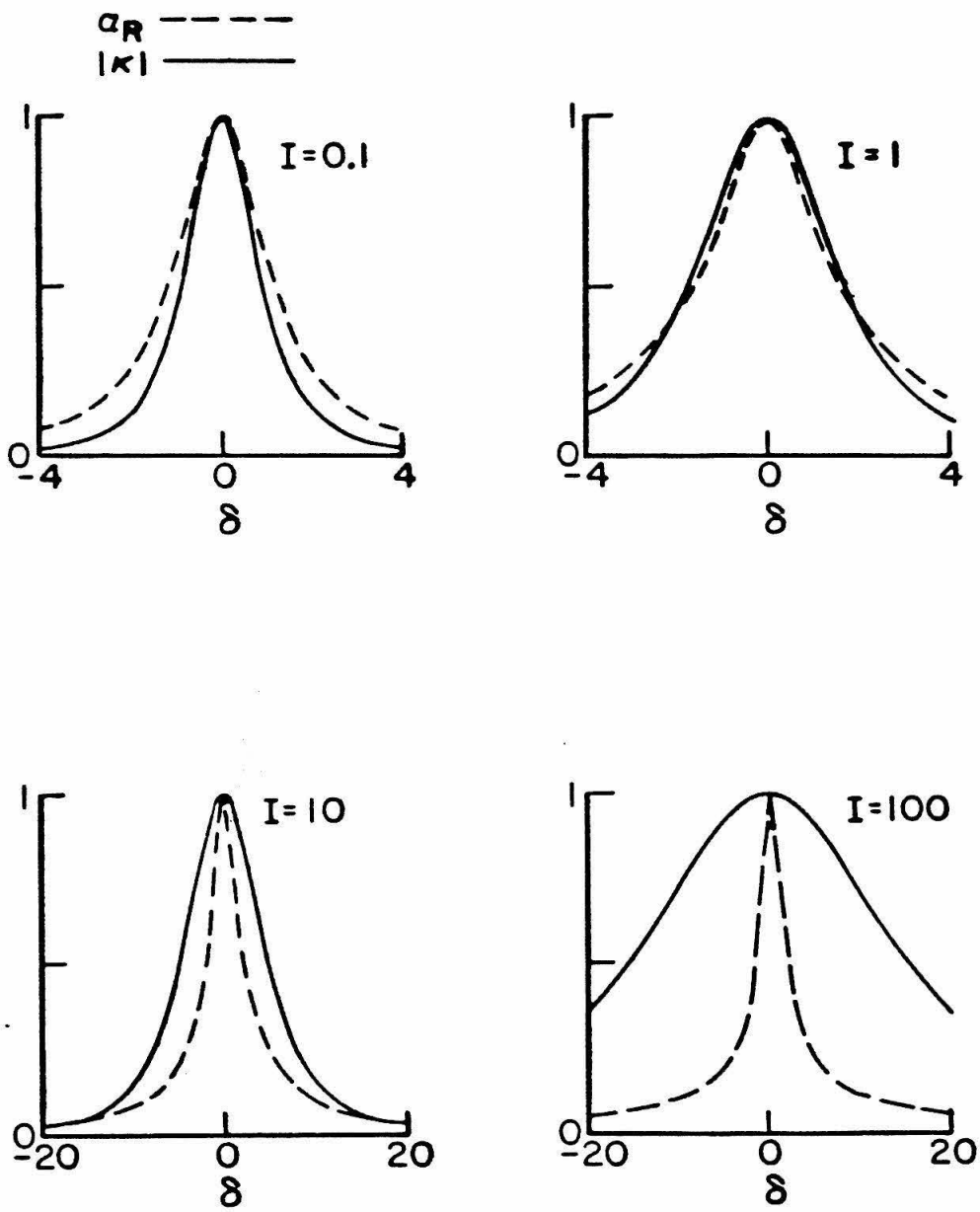

Fig. 4.5 α_R and $|\kappa|$ plotted versus the pump detuning δ for several values of I. All the curves are normalized to unity at $\delta = 0$.

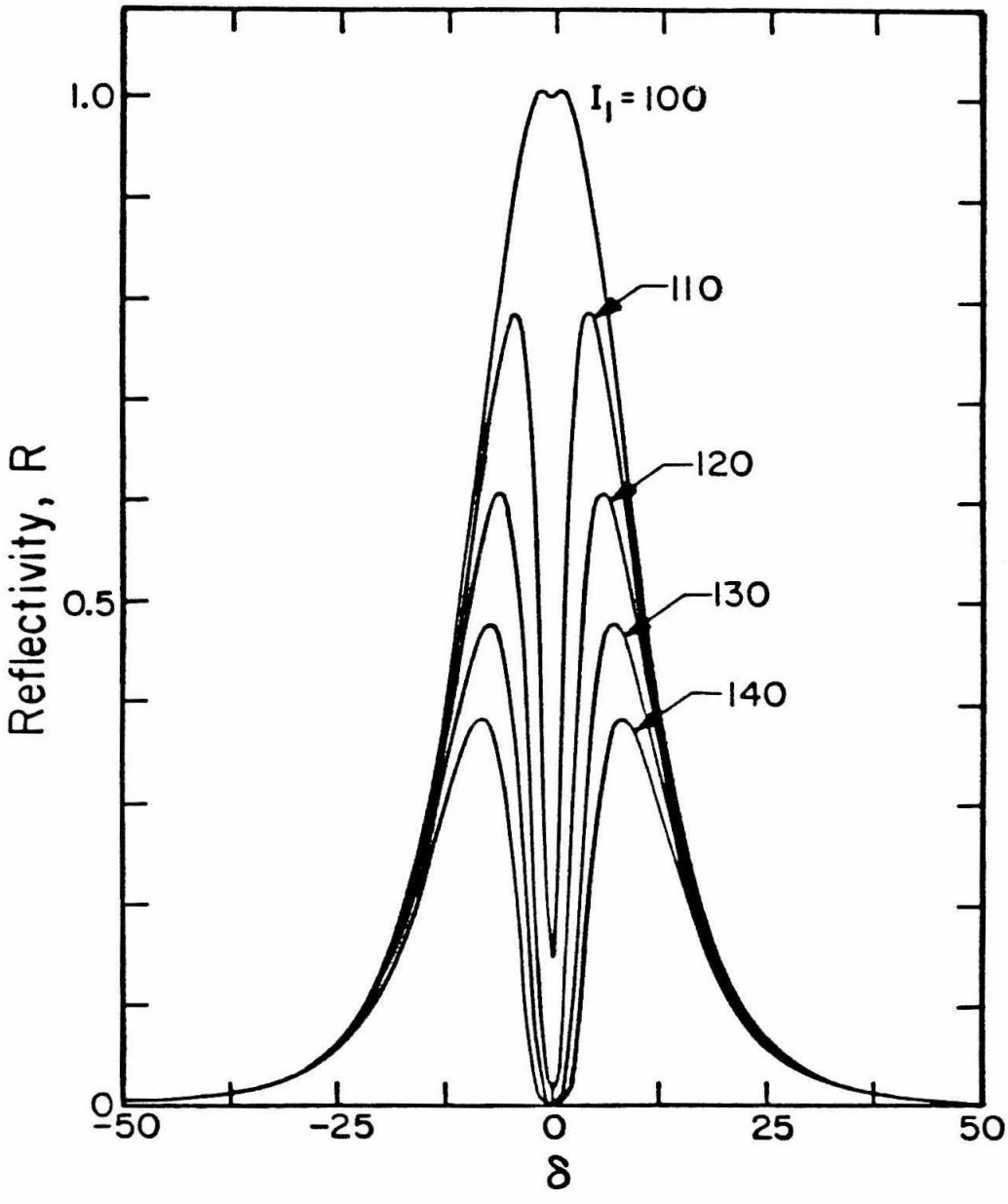

Fig. 4.6 Reflectivity versus the pump detuning δ for several values of I_1 with the product $I_1 \cdot I_2$ constant. The curves are normalized to $\delta = 0$ and $I_1 = 100$.

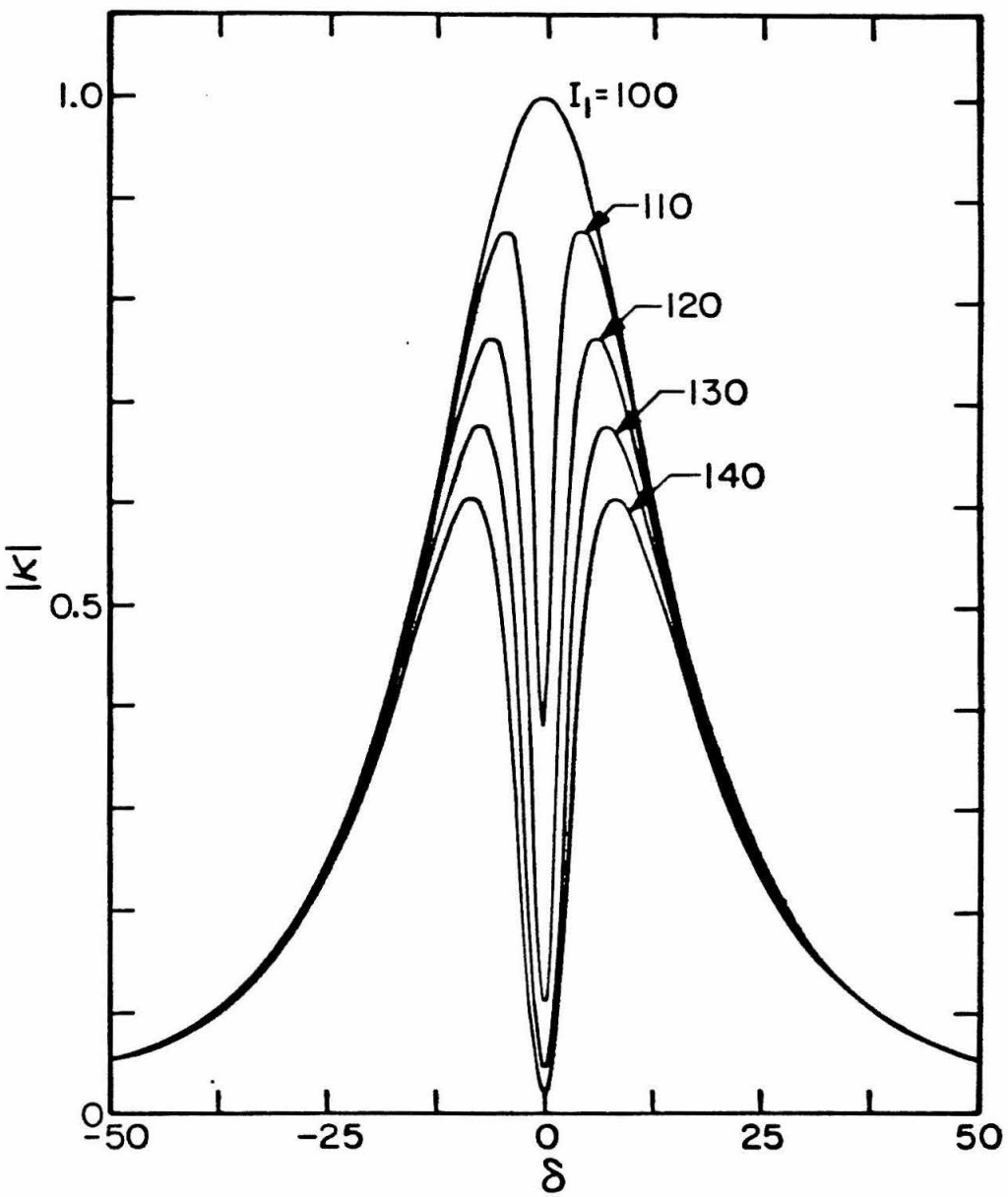

Fig. 4.7 $|\kappa|$ versus the pump detuning δ for several values of I_1 with the product $I_1 \cdot I_2$ constant. The curves are normalized to $\delta = 0$ and $I_1 = 100$.

4.5 Nondegenerate Four-Wave Mixing

Having considered the degenerate case, we will now study the nondegenerate case, $\nu \neq 0$. The main phenomenon we observe is the generation of Rabi sidebands which are a result of the ac Stark effect. Some aspects of this phenomenon have been discussed by Harter and Boyd[7] in their recent work. Our general solution agrees with their solution in the limit of equal intensity pump fields. However, as in the degenerate case, asymmetry in the pump waves has an important effect on the response of the system and is discussed in this chapter.

Before we discuss the Stark effect let us first demonstrate that a narrow bandwidth optical filter can be constructed using nondegenerate four-wave mixing. Using some of the parameters from Fig. 4.1, $\beta_0 L = 1$ and $\delta = 8$, Fig. 4.8 shows the reflectivity plotted versus ν for several values of I. All the curves are normalized to unity at $\nu = 0$. As I increases, the bandwidth narrows and achieves its minimum value for I = 36. If we recall Fig. 4.1, we see that I = 36 results in R reaching its maximum value of 11. Fig. 4.8 demonstrates that this process can yield an optical filter whose bandwidth depends on the inverse of the lifetime T_2 and which can be narrowed even more by operating in the gain regime and taking advantage of the exponential dependence of R on κ_i. Having discussed the filter concept, we will spend the remainder of the chapter discussing the Stark effect.

To understand the ac Stark effect consider a two-level system in the presence of an electromagnetic field, as discussed in section 2.2. The total wavefunction of the system is

$$\Psi = a_1(t)\,\psi_1 e^{-iE_1 t/\hbar} + a_2(t)\,\psi_2 e^{-iE_2 t/\hbar} \qquad (4.5\text{-}1)$$

where ψ_n are eigenfunctions of the unperturbed Hamiltoniar. H_0 such that

$$H_0\psi_1 = E_1\psi_1$$

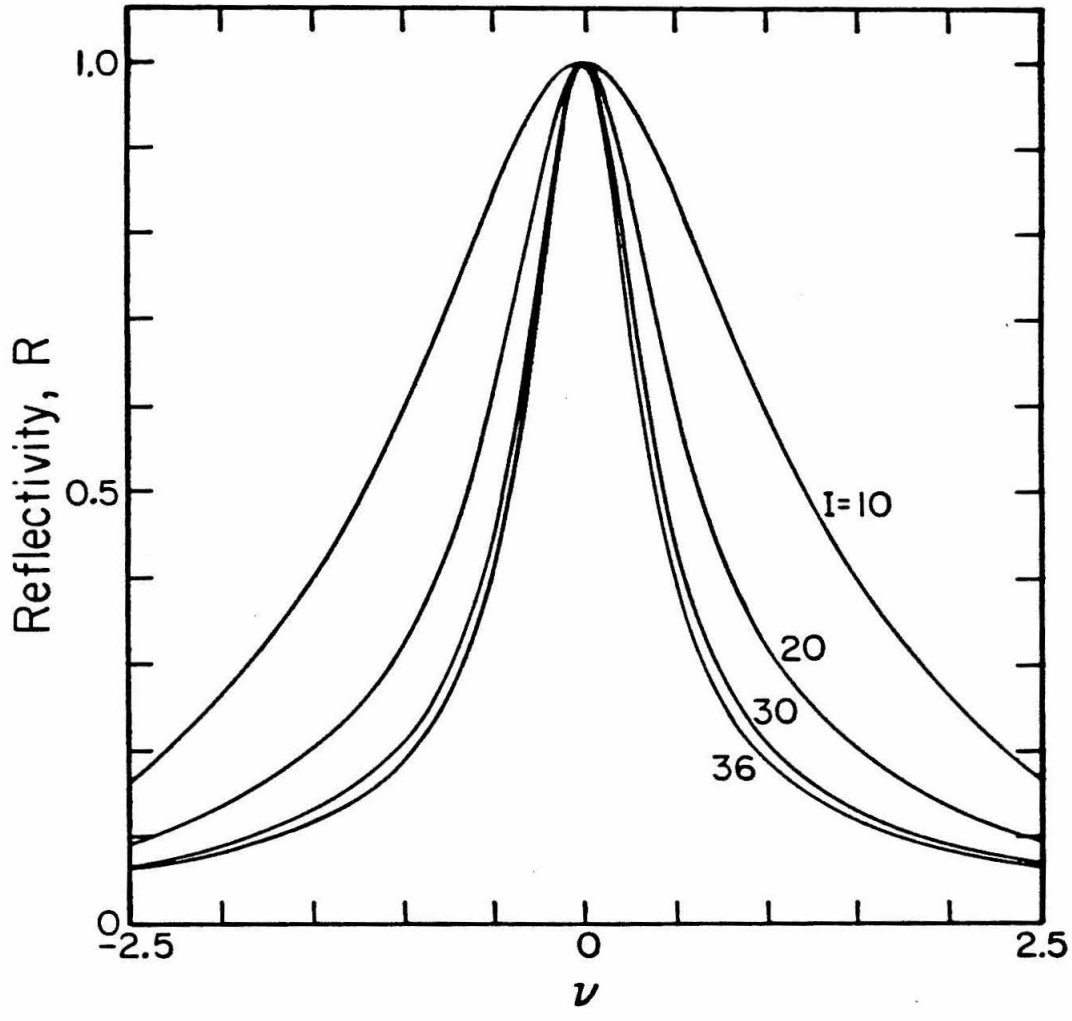

Fig. 4.8 Reflectivity versus the signal detuning ν for several values of I with $\delta = 8$ and $\beta_0 L = 1$. The curves are normalized to unity at $\nu = 0$.

$$H_0\psi_2 = E_2\psi_2 \tag{4.5-2}$$

The total Hamiltonian of the two-level system is

$$H = H_0 + H' \tag{4.5-3}$$

where the interaction Hamiltonian H' is assumed to be of the dipole type

$$H' = -\hat{\mu}E(t) \tag{4.5-4}$$

with $\hat{\mu}$ the component of the dipole operator along the direction of the electric field E(t).

The functions $a_1(t)$ and $a_2(t)$ represent the amplitude for the atom to occupy energy levels E_1 and E_2, respectively, at time t.

The electric field E(t) is given by

$$E(t) = \tfrac{1}{2}Ae^{i\omega t} + c.c. \tag{4.5-5}$$

For simplicity we will assume that A is real and represents the amplitude of the electric field at the location of an atom which is fixed in space.

The Schrodinger equation is given by

$$i\hbar\frac{\partial\Psi}{\partial t} = H\Psi \ . \tag{4.5-6}$$

Substituting the total wavefunction, Eq. (4.5-1), into the Schrodinger equation, we then multiply both sides of the equation by ψ_1^* and integrate over the atomic coordinates. Neglecting nonresonant terms we obtain

$$i\hbar\frac{da_1}{dt} = -a_2\frac{\mu A}{2}e^{i\Delta\omega t} \tag{4.5-7}$$

with $\Delta\omega \equiv \omega - \omega_0 << \omega_0$ and $\mu \equiv \langle\psi_1|\hat{\mu}|\psi_2\rangle = \langle\psi_2|\hat{\mu}|\psi_1\rangle$. A similar procedure yields

$$i\hbar\frac{da_2}{dt} = -a_1\frac{\mu A}{2}e^{-i\Delta\omega t} \tag{4.5-8}$$

The Rabi frequency Ω is defined as

$$\Omega = \frac{\mu A}{\hbar}. \tag{4.5-9}$$

The coupled equations for $a_1(t)$ and $a_2(t)$ can now be written as

$$\frac{da_1}{dt} = \frac{i\Omega}{2} a_2 e^{i\Delta\omega t}$$

$$\frac{da_2}{dt} = \frac{i\Omega}{2} a_1 e^{-i\Delta\omega t} \tag{4.5-10}$$

We will assume that the atom is initially in the ground state, $a_1(0) = 1$, $a_2(0) = 0$, and solve for the subsequent behavior of the atom. The solutions for a_1 and a_2 are

$$a_1(t) = \frac{\sqrt{(\Delta\omega)^2 + \Omega^2} - \Delta\omega}{2\sqrt{(\Delta\omega)^2 + \Omega^2}} e^{-i[-\frac{\Delta\omega}{2} - \frac{1}{2}\sqrt{(\Delta\omega)^2 + \Omega^2}]t}$$

$$+ \frac{\sqrt{(\Delta\omega)^2 + \Omega^2} + \Delta\omega}{2\sqrt{(\Delta\omega)^2 + \Omega^2}} e^{-i[-\frac{\Delta\omega}{2} + \frac{1}{2}\sqrt{(\Delta\omega)^2 + \Omega^2}]t}$$

$$a_2(t) = \frac{\Omega}{2\sqrt{(\Delta\omega)^2 + \Omega^2}} e^{-i[\frac{\Delta\omega}{2} - \frac{1}{2}\sqrt{(\Delta\omega)^2 + \Omega^2}]t}$$

$$- \frac{\Omega}{2\sqrt{(\Delta\omega)^2 + \Omega^2}} e^{-i[\frac{\Delta\omega}{2} + \frac{1}{2}\sqrt{(\Delta\omega)^2 + \Omega^2}]t}. \tag{4.5-11}$$

We can define a generalized Rabi frequency Ω_g

$$\Omega_g = \sqrt{(\Delta\omega)^2 + \Omega^2}. \tag{4.5-12}$$

Using Ω_g in the expressions for a_1 and a_2, the total wavefunction Ψ can be written as

$$\Psi = \frac{\Omega_g - \Delta\omega}{2\Omega_g} \psi_1 e^{-i[\frac{E_1}{\hbar} - \frac{\Delta\omega}{2} - \frac{\Omega_g}{2}]t}$$

$$+ \frac{\Omega_g + \Delta\omega}{2\Omega_g} \psi_1 e^{-i[\frac{E_1}{\hbar} - \frac{\Delta\omega}{2} + \frac{\Omega_g}{2}]t}$$

$$+ \frac{\Omega}{2\Omega_g} \psi_2 e^{-i[\frac{E_2}{\hbar} + \frac{\Delta\omega}{2} - \frac{\Omega_g}{2}]t}$$

$$- \frac{\Omega}{2\Omega_g} \psi_2 e^{-i[\frac{E_g}{\hbar} + \frac{\Delta\omega}{2} + \frac{\Omega_g}{2}]t} . \qquad (4.5\text{-}13)$$

Looking at the time dependence of Ψ we can interpret the results as meaning the ground state is split into two energy levels E_1^+ and E_1^- with

$$E_1^+ = E_1 + \tfrac{1}{2}\hbar(\Omega_g - \Delta\omega)$$

$$E_1^- = E_1 - \tfrac{1}{2}\hbar(\Omega_g + \Delta\omega) . \qquad (4.5\text{-}14)$$

The ground state splitting, $E_1^+ - E_1^- = \hbar\Omega_g$. The excited state is split into two energy levels E_2^+ and E_2^- with

$$E_2^+ = E_2 + \tfrac{1}{2}\hbar(\Omega_g + \Delta\omega)$$

$$E_2^- = E_2 - \tfrac{1}{2}\hbar(\Omega_g - \Delta\omega) . \qquad (4.5\text{-}15)$$

The excited state splitting, $E_2^+ - E_2^- = \hbar\Omega_g$. The coefficients of ψ_n can be interpreted as the amplitudes to be in each of these four states.

There are four possible dipole transitions with energy separations given by

$$E_2^+ - E_1^+ = \hbar\omega$$

$$E_2^+ - E_1^- = \hbar(\omega + \Omega_g)$$

$$E_2^- - E_1^+ = \hbar(\omega - \Omega_g)$$

$$E_2^- - E_1^- = \hbar\omega \qquad (4.5\text{-}16)$$

To simplify the discussion we can define a normalized Rabi frequency

$$\nu_R = \Omega_g T_2 . \qquad (4.5\text{-}17)$$

Now, let us consider nondegenerate four-wave mixing. We will assume that the strong pump waves at frequency ω cause the ac Stark effect. Then we would expect a resonance in the reflectivity R when $\nu = 0, \pm\nu_R$ as well as the usual resonances at $\pm\delta$ which have been discussed in Chapter II. The case $\nu = 0$ corresponds to the signal waves and pump waves all being resonant with one transition, while the cases

$\nu = \pm \nu_R$ correspond to the situation in which each of the four waves is resonant with a different transition. This is better illustrated in Fig. 4.9 where we show the energy levels of the two-level system in the presence of strong pump waves which cause a splitting $\hbar\Omega_g$ in both the ground state and the excited state. This figure shows the case $\omega_4 = \omega + \Omega_g$, $\omega_3 = \omega - \Omega_g$, which implies a resonance at $\nu = \nu_R$.

To relate the Rabi frequency to the pump wave amplitude in the case of four-wave mixing, we will consider equal amplitude pump waves such that A is given by Eqs. (4.2-7). From Eq. (4.2-9) and the definition of E_g^2 we have

$$\left| \frac{\mu A T_2}{\hbar} \right|^2 = \frac{2I}{a} [\, 1 + \cos(x + \vartheta) \,] . \tag{4.5-18}$$

Now, the most probable value of a cosine is at its maximum or minimum so we can expect the right side of Eq. (4.5-18) to have either 0 or 4I/a as its most probable value. Since 0 results in no Stark splitting we expect the Stark splitting to be such that

$$\nu_R = \sqrt{\frac{4I}{a} + \delta^2} . \tag{4.5-19}$$

Having described the Stark effect we will now consider the calculated reflectivity and compare it with our model.

Considering the case of equal intensity pump waves first, we chose the parameters to be $\alpha_0 L = 1$, $I = 100$, $T_1/T_2 = 1/2$. Figs. 4.10 (a) - (d) show the reflectivity R versus ν for various values of δ. In this series of plots we observe a peak at $\nu = 0$ and side peaks at $\nu = \pm 28.06$ which grow in amplitude and shift slightly as δ is increased. These are the side bands due to the ac Stark effect. In addition, we have peaks at $\nu = \pm \delta$. This five peak structure has been observed recently[9].

From Eq. (4.5-19) we expect the side peaks to occur at $\nu_R = 28.28$. Fig. 4.11 shows the value of ν, at the side peaks, plotted versus I. The solid line is the calculated

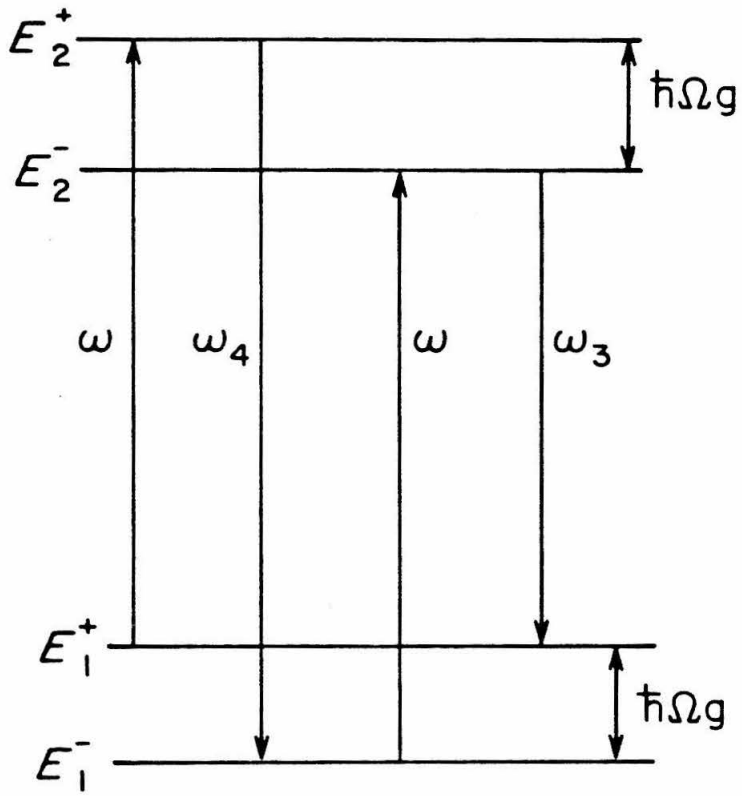

Fig. 4.9 Energy levels of the two-level system in the presence of a strong applied electromagnetic field.

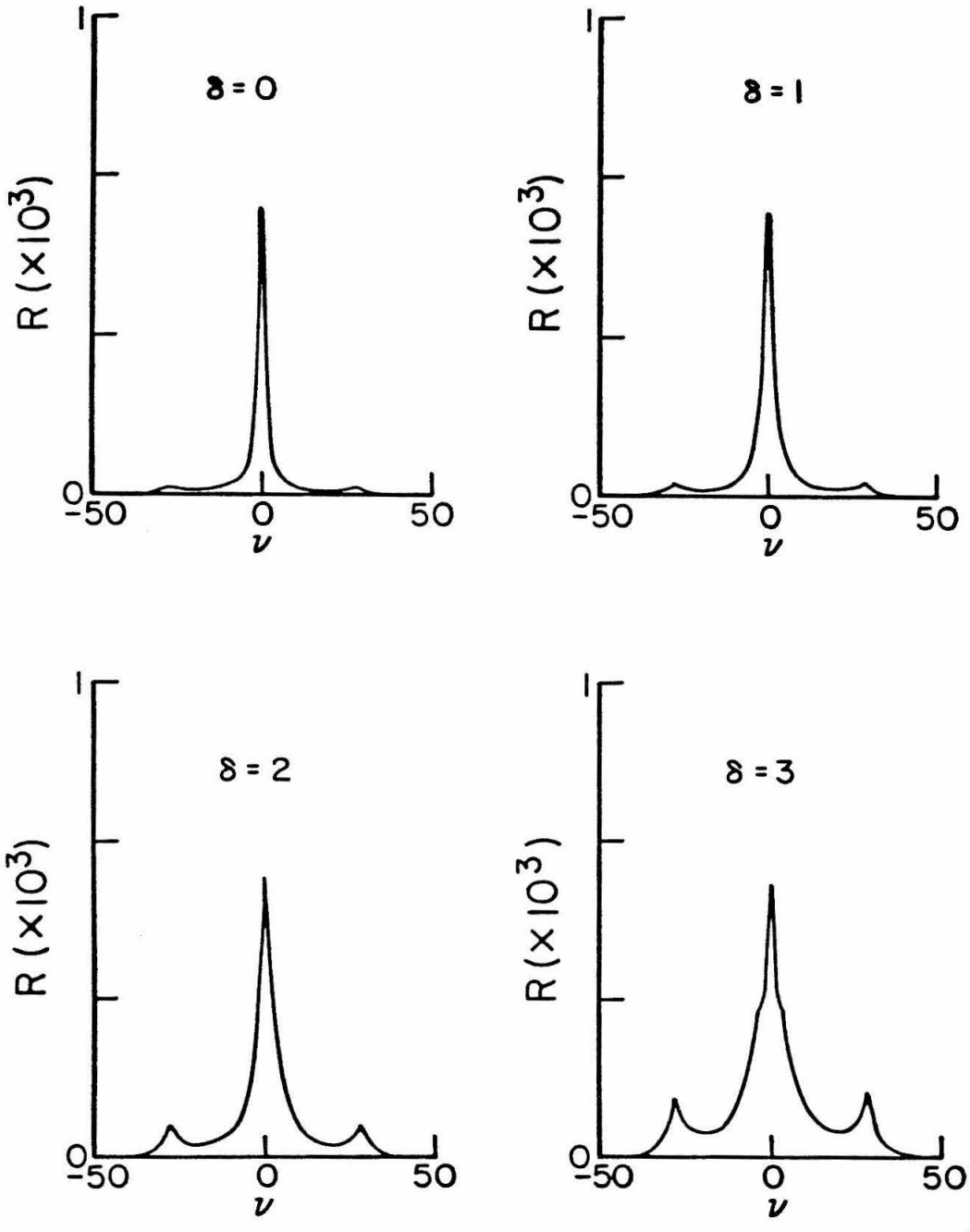

Fig. 4.10 (a) Reflectivity versus signal detuning ν for various values of δ.

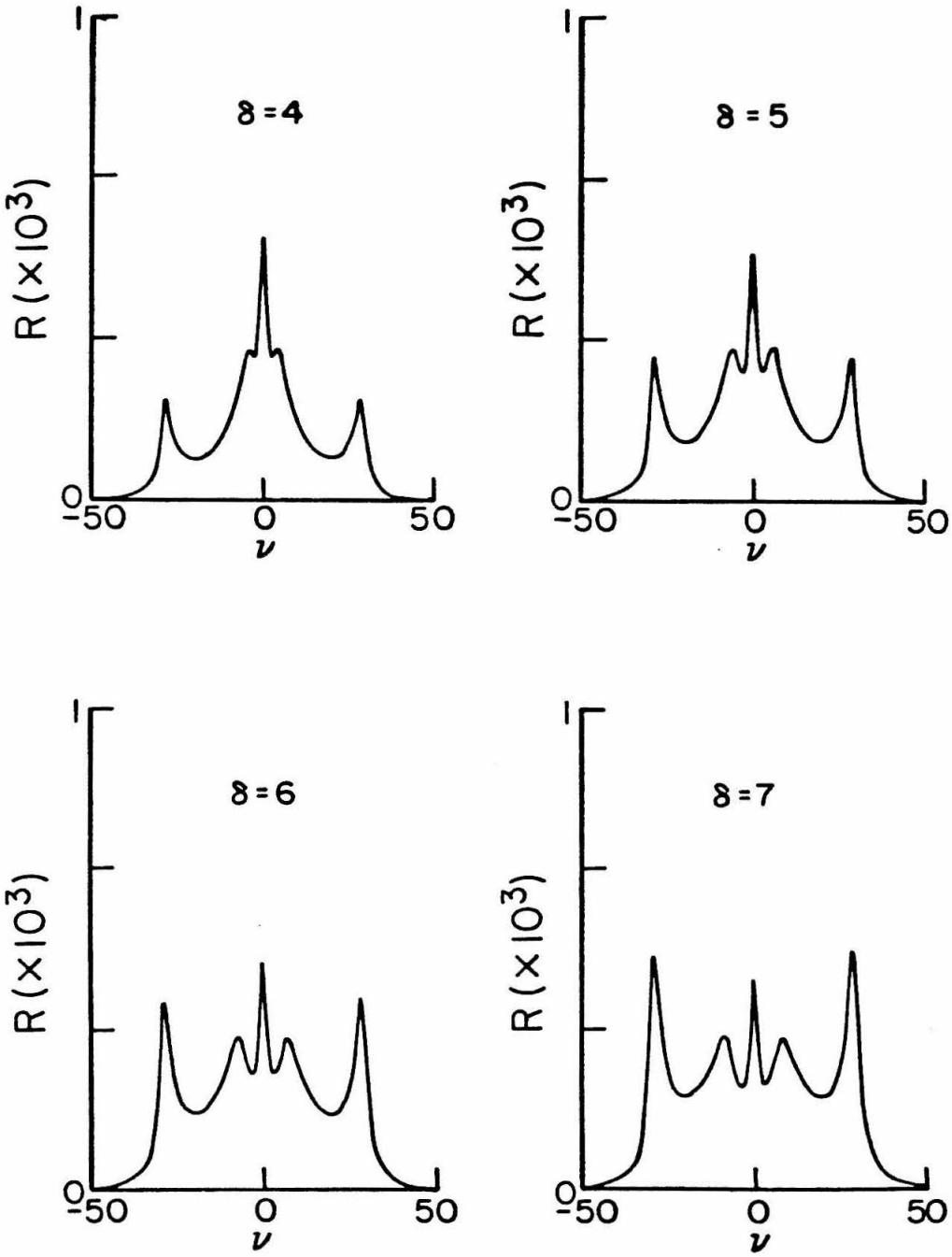

Fig. 4.10 (b) Reflectivity versus signal detuning ν for various values of δ.

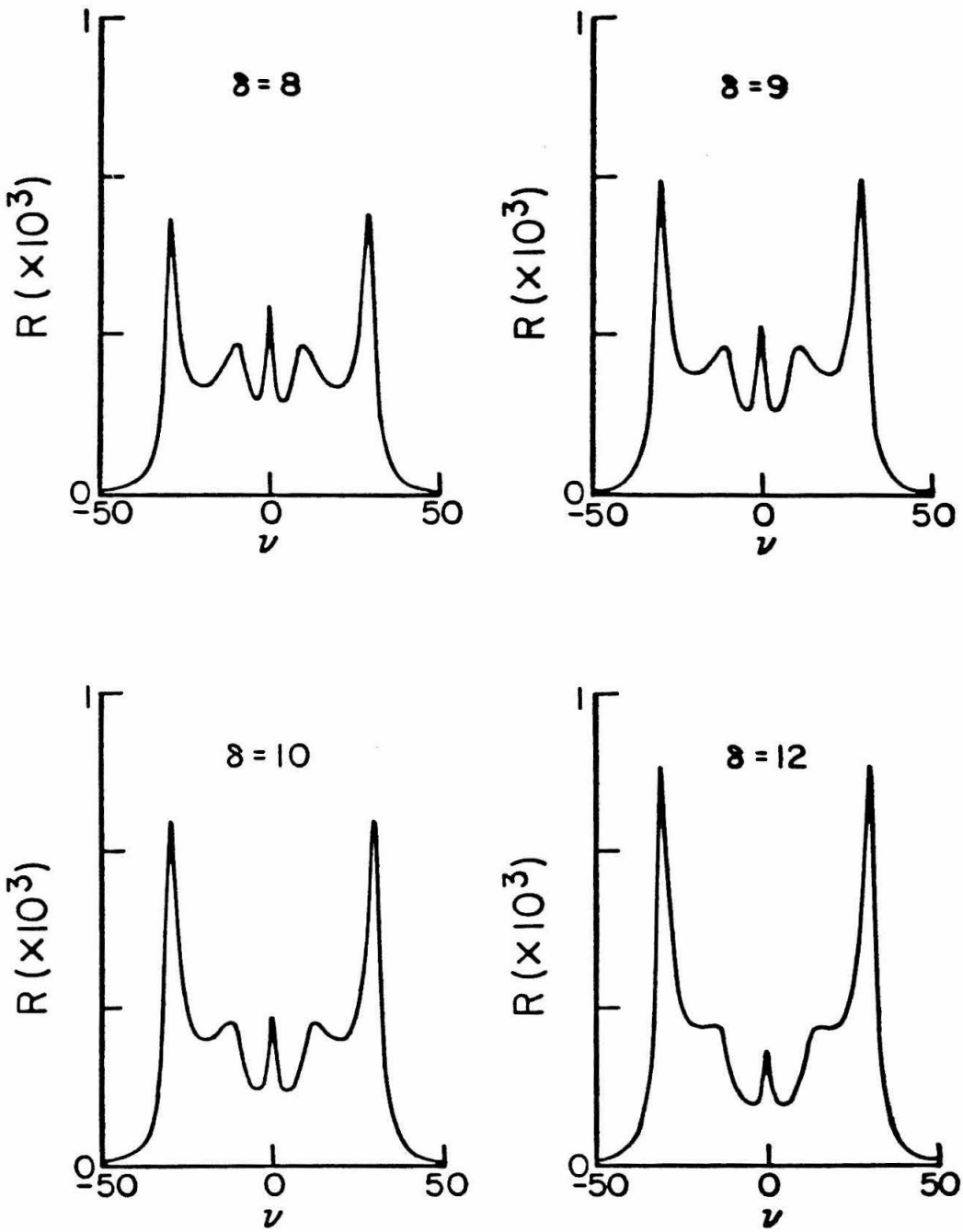

Fig. 4.10 (c) Reflectivity versus signal detuning ν for various values of δ.

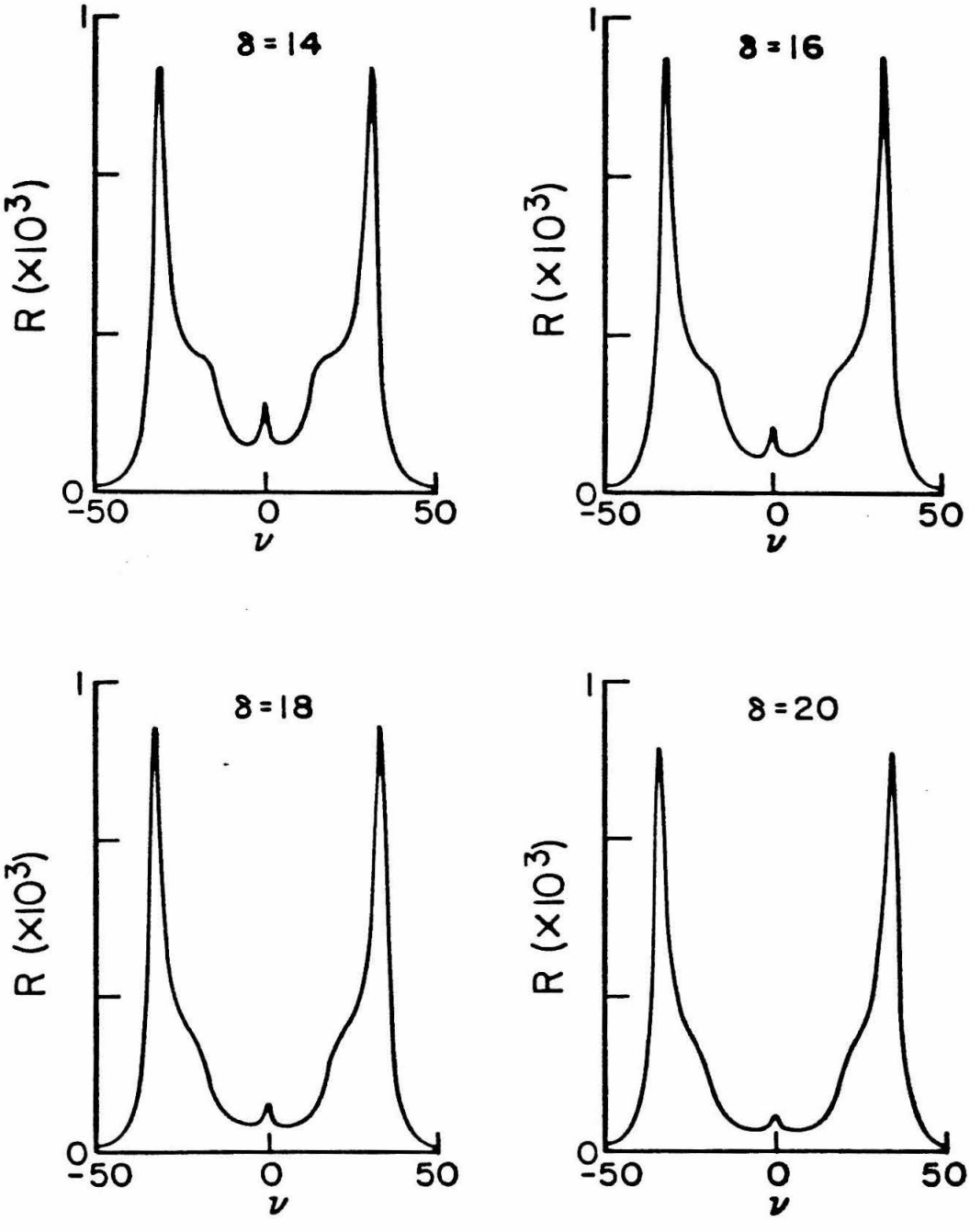

Fig. 4.10 (d) Reflectivity versus signal detuning ν for various values of δ.

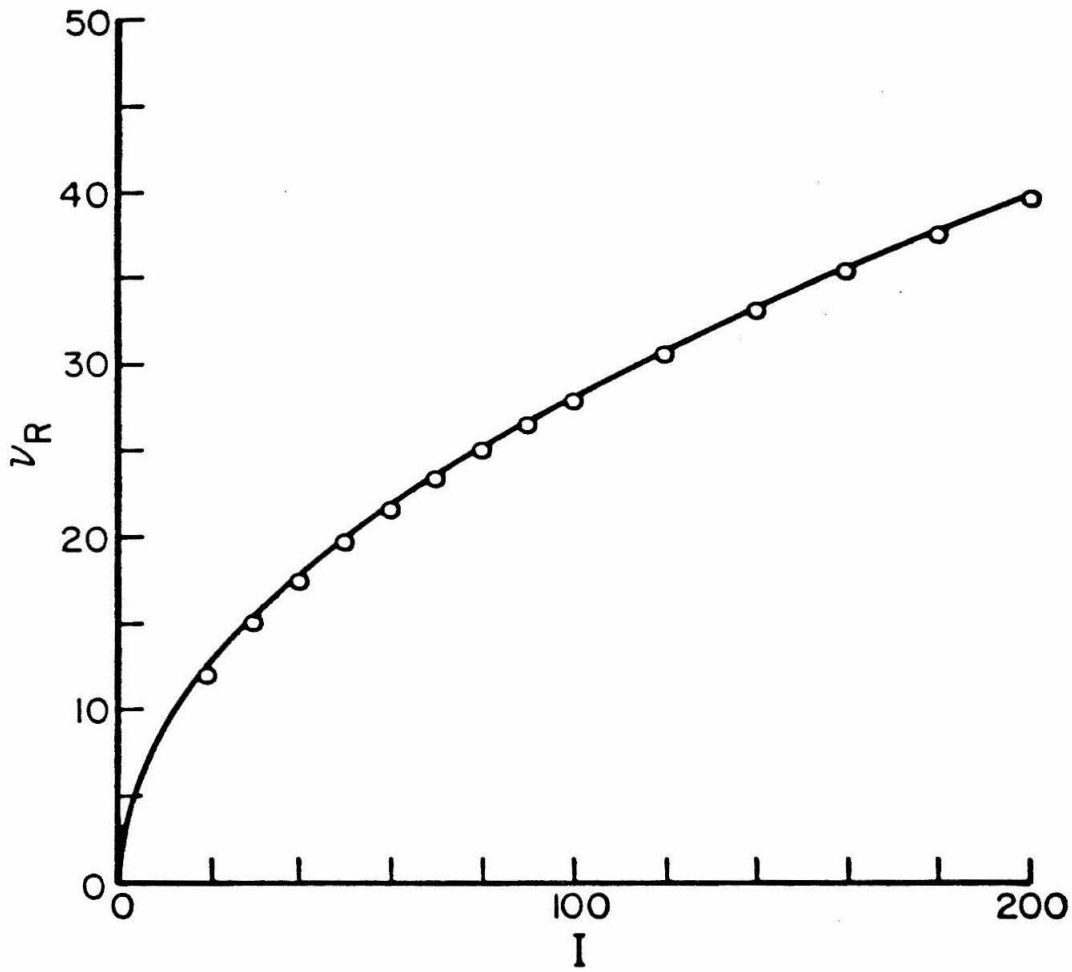

Fig. 4.11 Calculated Rabi frequency ν_R, solid line, and measured sideband ν_{sp}, open circles, plotted versus I.

value ν_R, while the open circles gives the value of ν at the side peaks which is determined by calculating R versus ν and measuring where R has a local maximum. We will define this measured value of ν as ν_{sp}. The agreement between ν_{sp} and ν_R is excellent. We have also compared ν_{sp} with ν_R as a function of δ and T_1/T_2 and also obtain excellent agreement.

Figs. 4.12 (a) - (c) show R plotted versus ν for several values of I_1 with $I_1 \cdot I_2 = 10^4$ and the other parameters unchanged from the previous figure. As I_1 increases, the amplitude of the central peak diminishes. This peak then splits into two peaks whose separation increases with I_1.

We can understand this double peaked structure in each sideband by recalling Eq. (4.2-9), which gives the standing wave pattern for the pump wave intensity. In the case of asymmetric pump wave amplitudes, this equation results in a modification of Eq. (4.5-18) to

$$\left| \frac{\mu A T_2}{\hbar} \right|^2 = \frac{1}{a} [\, I_1 + I_2 + 2\sqrt{I_1 I_2} \cos(x + \vartheta) \,] \qquad (4.5\text{-}20)$$

Again using the fact that the cosine function has ± 1 as its most probable value, we expect that the normalized Rabi frequency ν_R will be given by

$$\nu_R^2 = \frac{1}{a} [\, I_1 + I_2 \pm 2\sqrt{I_1 I_2} \,] + \delta^2 \qquad (4.5\text{-}21)$$

Defining ν_R to be the positive root, the resonances occur at $\nu = \pm \nu_R$ with ν_R being double valued. Taking the case $I_1 = 400$, $I_2 = 25$; this gives $\nu_R = 21.21$ and 35.36, which agrees very well with the position of the peaks at $\nu_{sp} = 22.23$ and 34.72, which are observed in Fig. 4.12 (c). For the values shown in Figs. 4.12 (a) - (c), the observed peaks coincide quite closely with the resonances expected from the calculated values of ν_R.

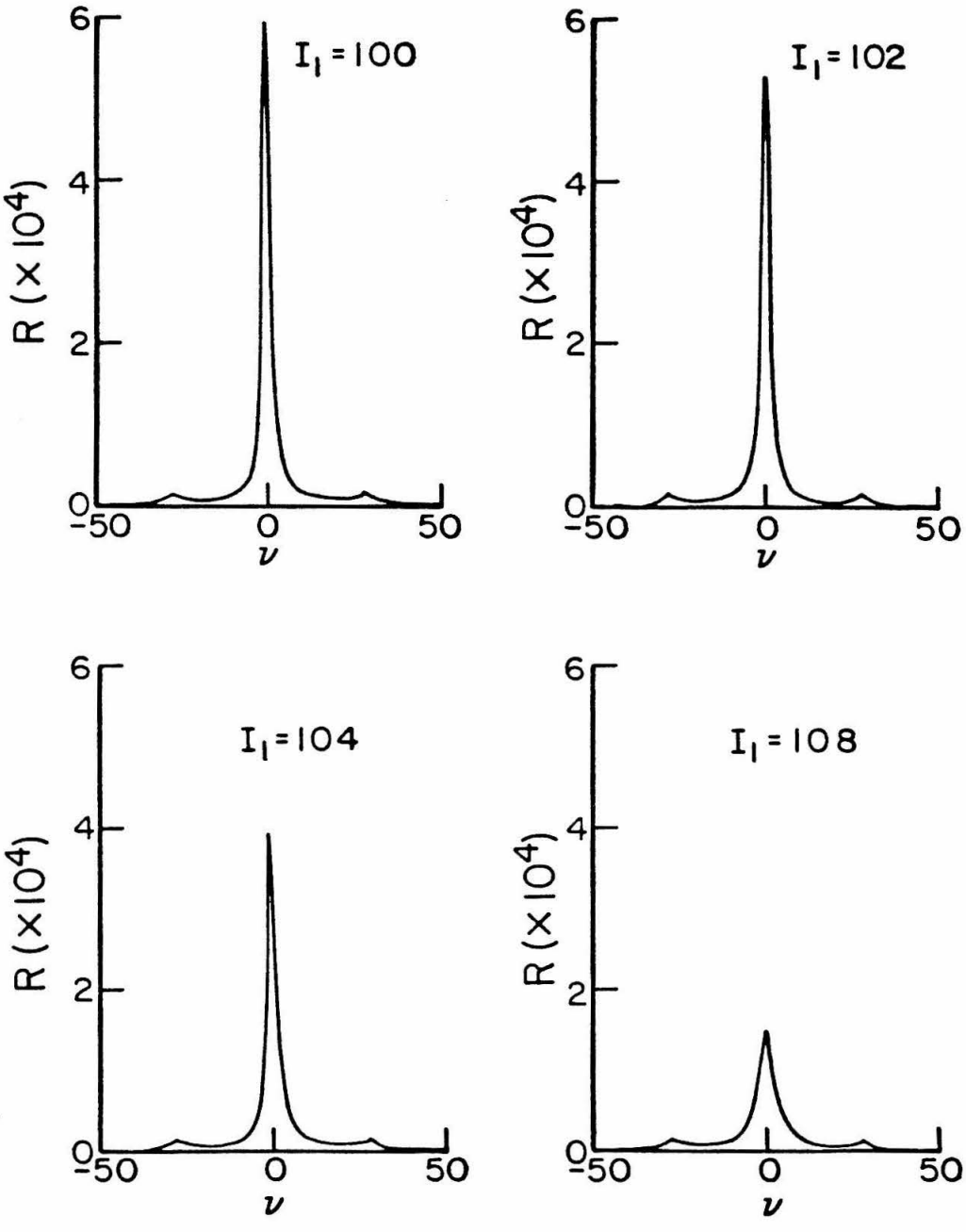

Fig. 4.12 (a) Reflectivity versus signal detuning ν for several values of I_1 with $\delta = 0$.

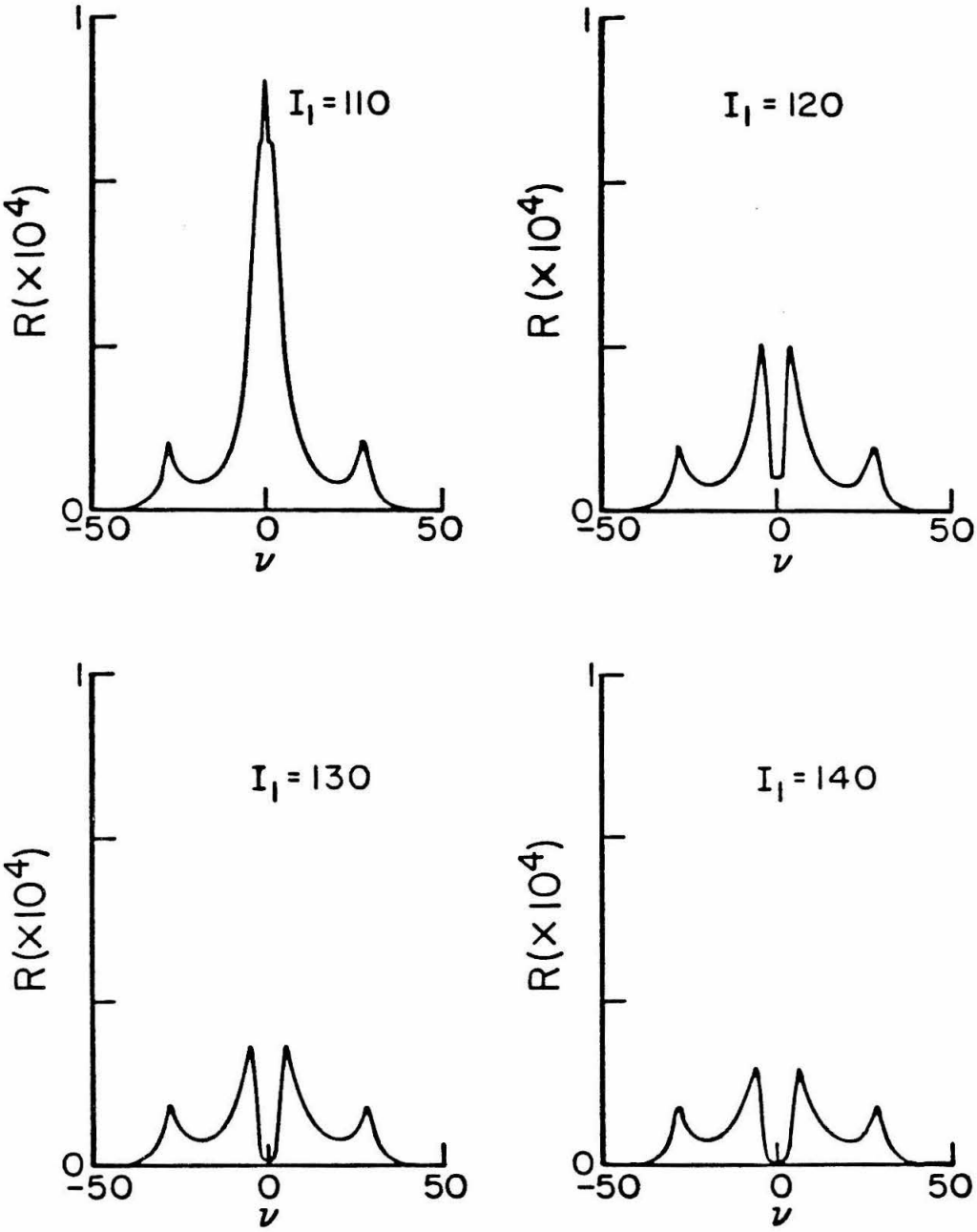

Fig. 4.12 (b) Reflectivity versus signal detuning ν for several values of I_1 with $\delta = 0$.

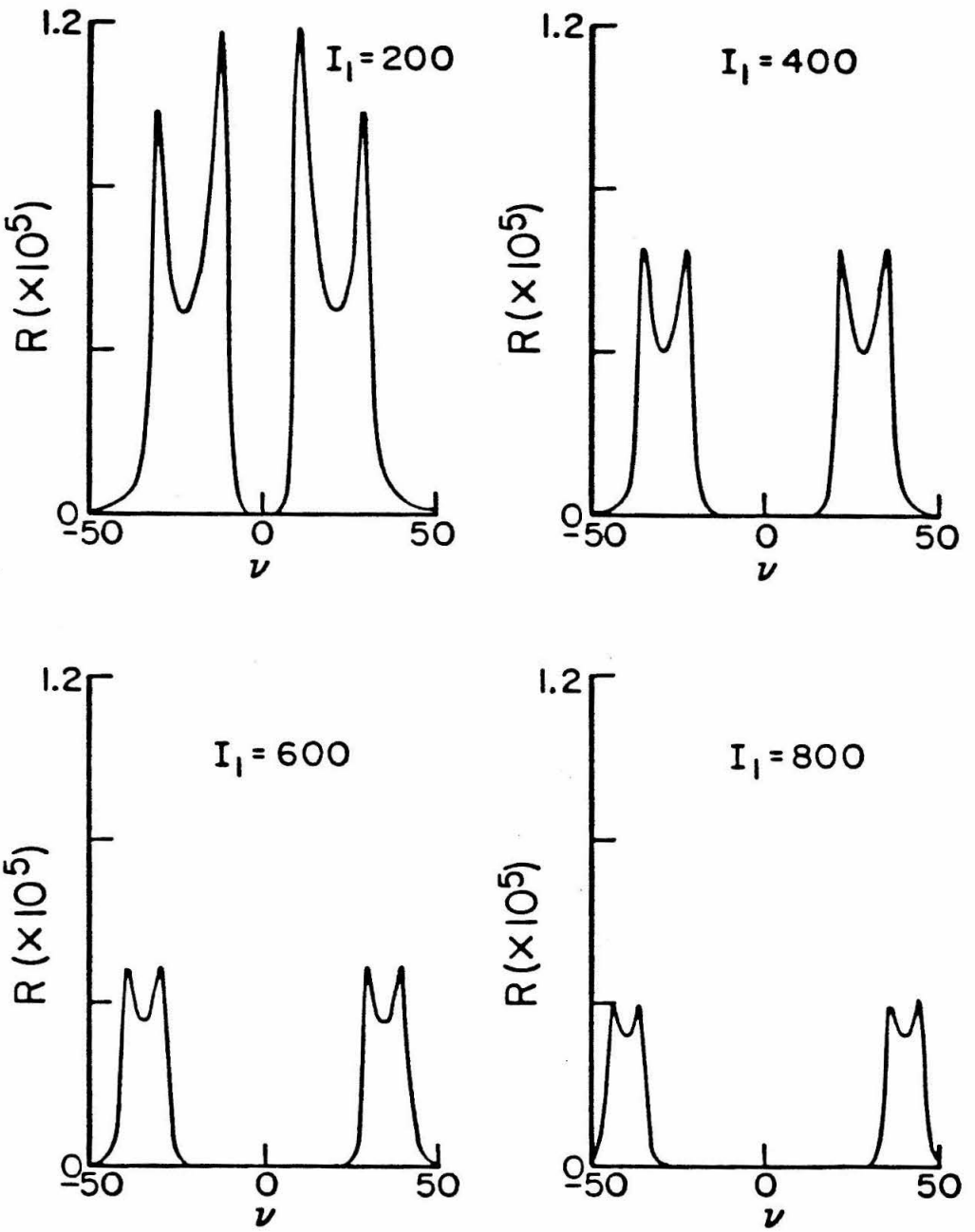

Fig. 4.12 (c) Reflectivity versus signal detuning ν for several values of I_1 with $\delta = 0$.

4.6 Conclusion

This chapter has presented a very general solution, which includes the effect of saturating pump waves, for nondegenerate four-wave mixing in a homogeneously broadened two-level system. In the degenerate case, we have presented several new phenomena. The first phenomenon is a dip in the reflectivity at line-center due to the relative power-broadened linewidths of the linear absorption coefficient and the nonlinear(third order) susceptibility. The second interesting phenomenon also manifested itself as a dip in the reflectivity at line-center, but was a result of using pump waves of different amplitude. In the latter situation, the reflection coefficient depends primarily on κ, the nonlinear coupling coefficient, and it is κ's dependence on the asymmetric pump fields that results in the dip.

In the nondegenerate case, we presented the dependence of the reflection coefficient on ν, the signal detuning, and demonstrated a narrow bandwidth optical filter which has an efficiency greater than unity. We then considered in greater detail the ac Stark effect and how it generates sidebands in the filter response whose location depends on the pump wave intensities. These could be used to construct a tunable filter which utilizes this effect to control the frequency of the central bandpass of the filter. As a spectroscopic tool we could use the location of the Rabi sidebands as a measure of the dipole moment of the atom. Regardless of the actual application, we have explained quite thoroughly the ac Stark effect and its importance in nondegenerate four-wave mixing.

References for Chapter IV

1. J. Nilsen and A. Yariv, "Nearly degenerate four-wave mixing applied to optical filters," Appl. Opt. 18,143 (1979).

2. J. Nilsen and A. Yariv, "Nondegenerate four-wave mixing in a Doppler-broadened resonant medium," J.Opt.Soc.Am. 71,180 (1981).

3. Joseph Nilsen and Amnon Yariv, "A tunable narrowband optical filter via phase conjugation by nondegenerate four-wave mixing in a Doppler-broadened resonant medium," Opt. Comm. 39,199 (1981).

4. R. L. Abrams and R. C. Lind, "Degenerate four-wave mixing in absorbing media," Opt. Lett. 2,94 (1978).

5. R. L. Abrams and R. C. Lind, "Degenerate four-wave mixing in absorbing media: errata," Opt. Lett. 3,205 (1978).

6. Fu Tao-Yi and M. Sargent III, "Effects of signal detuning on phase conjugation," Opt. Lett. 4,366 (1979).

7. D. J. Harter and R. W. Boyd, "Nearly degenerate four-wave mixing enhanced by the ac Stark effect," IEEE J. Quantum Electron. QE-16,1126 (1980).

8. A. Yariv and D. M. Pepper, "Amplified reflection, phase conjugation, and oscillation in degenerate four-wave mixing," Opt. Lett. 1,16 (1977).

9. D. G. Steel and R. C. Lind, "Multiresonant behavior in nearly degenerate four-wave mixing: the ac Stark effect," Opt. Lett. 6,587 (1981).

Chapter V

SODIUM AS A NONLINEAR MEDIUM

5.1 Introduction

The last several chapters have discussed the theoretical solutions to phase conjugation in a two level system which is both homogeneously broadened[1] and inhomogeneously broadened[2,3]. In this chapter we will look at sodium vapor and see how it models a two level system and examine some of the differences between a real atomic system and the theoretical model. We are considering sodium because that is the material used as the nonlinear medium in our experiments. At the end of the chapter we will discuss other materials which better model a two level system and which may be more suitable to use as the nonlinear medium.

5.2 Energy Levels of Sodium

First we will look at the energy levels for the 3S - 3P transition with which the lasers will be resonant. Spin-orbit coupling splits the 3P energy level into two levels; $3P_{1/2}$ and $3P_{3/2}$. The resulting transitions, $3S_{1/2} - 3P_{1/2}$ and $3S_{1/2} - 3P_{3/2}$, are at 5896 Å and 5890 Å, respectively[4].

Sodium has one naturally occuring isotope[5], Na^{23}, which has a nuclear spin $I = 3/2$. The nuclear spin causes a hyperfine splitting[6,7] of the ground state $3S_{1/2}$ into levels $3S_{1/2}(F = 2)$ and $3S_{1/2}(F = 1)$. In addition these levels are divided into $2F + 1$ Zeeman sublevels with $m_F = F, F - 1, \ldots, -F$ where m_F is the eigenvalue of the z component of the total spin operator F. This makes a total of eight levels for the ground state.

The excited state $3P_{1/2}$ is split into two hyperfine levels[8] $3P_{1/2}(F = 2)$ and $3P_{1/2}(F = 1)$ while the other excited state $3P_{3/2}$ is split into four hyperfine levels[9] $3P_{3/2}(F = 3)$, $3P_{3/2}(F = 2)$, $3P_{3/2}(F = 1)$, and $3P_{3/2}(F = 0)$. Taking the Zeeman

structure into account, the 3P excited state is split into twenty four excited states. Figure 5.1 shows the relevant energy levels of the sodium atom.

5.3 Wavefunctions for Sodium

In order to calculate the transition rates between the various ground states and excited states of sodium we need to know the wavefunctions for these various states. We will assume that I, I_z, L, L_z, S, S_z are all good operators to express the wavefunctions in terms of. I is the nuclear spin operator, L is the total angular momentum operator, S is the electron spin operator, I_z,etc.,are the operators for the z components of the various spin operators.

For the S ground state

$$I = 3/2 \quad L = 0 \quad S = 1/2 \quad J = 1/2$$

First we will consider the F = 2 hyperfine state.

$$| F = 2 \;\; M = 2 >_S = | M_I = 3/2 \;\; M_L = 0 \;\; M_S = 1/2 >_S$$

$$| F = 2 \;\; M = 1 >_S = \frac{1}{2}(\sqrt{3} \, | 1/2 \;\; 0 \;\; 1/2 >_S + | 3/2 \;\; 0 \;\; -1/2 >_S)$$

$$| F = 2 \;\; M = 0 >_S = \frac{1}{\sqrt{2}}(| -1/2 \;\; 0 \;\; 1/2 >_S + | 1/2 \;\; 0 \;\; -1/2 >_S)$$

$$| F = 2 \;\; M = -1 >_S = \frac{1}{2}(\sqrt{3} \, | -1/2 \;\; 0 \;\; -1/2 >_S + | -3/2 \;\; 0 \;\; 1/2 >_S)$$

$$| F = 2 \;\; M = -2 >_S = | -3/2 \;\; 0 \;\; -1/2 >_S$$

For the F = 1 hyperfine level we have

$$| F = 1 \;\; M = 1 >_S = \frac{1}{2}(| 1/2 \;\; 0 \;\; 1/2 >_S - \sqrt{3} \, | 3/2 \;\; 0 \;\; -1/2 >_S)$$

$$| F = 1 \;\; M = 0 >_S = \frac{1}{\sqrt{2}}(| -1/2 \;\; 0 \;\; 1/2 >_S - | 1/2 \;\; 0 \;\; -1/2 >_S)$$

$$| F = 1 \;\; M = -1 >_S = \frac{1}{2}(\sqrt{3} \, | 3/2 \;\; 0 \;\; -1/2 >_S - | 1/2 \;\; 0 \;\; 1/2 >_S)$$

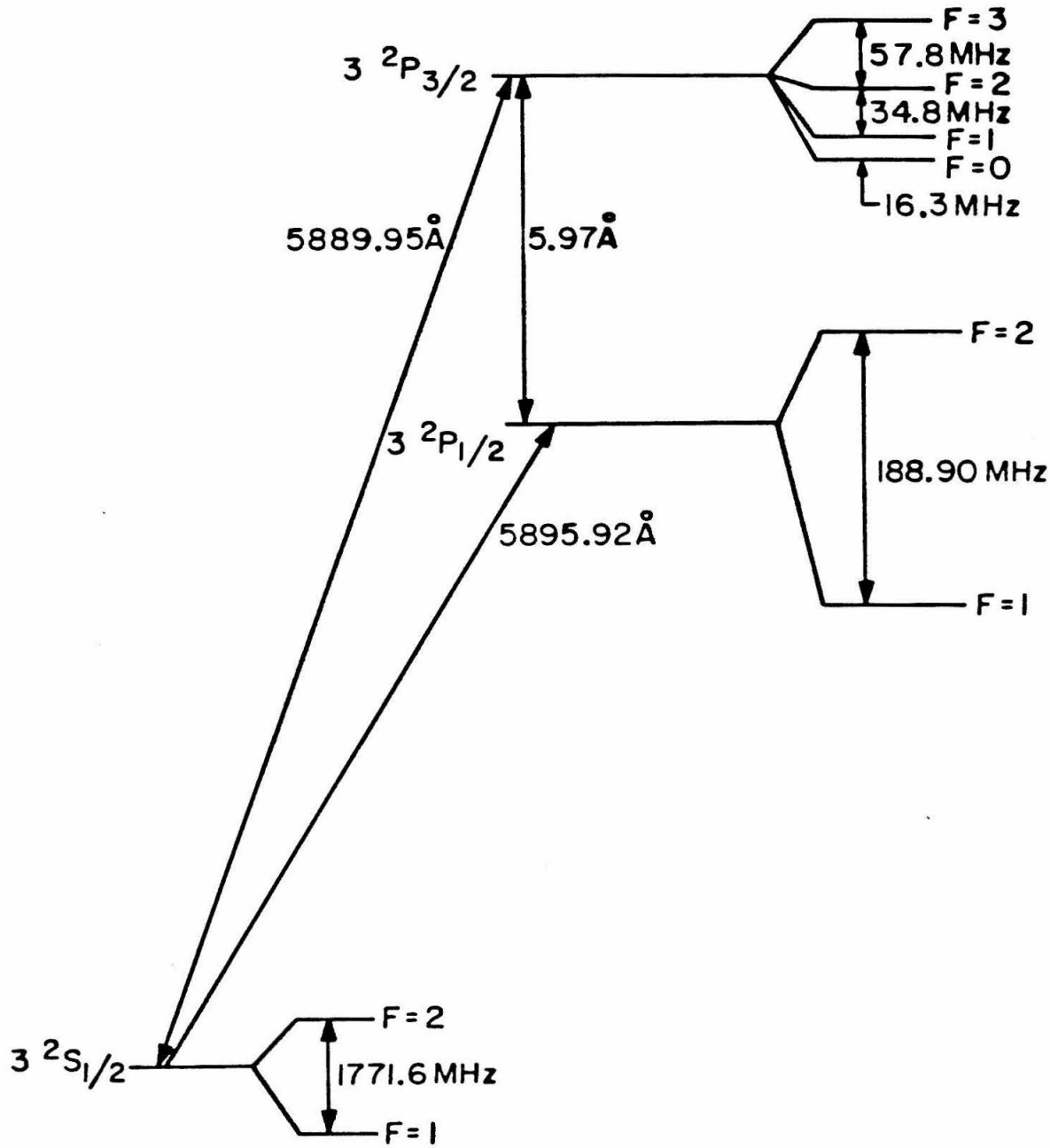

Fig. 5.1 Energy levels of sodium

For the $P_{3/2}$ excited state

$$L = 3/2 \quad L = 1 \quad S = 1/2 \quad J = 3/2$$

We will first consider the F = 3 hyperfine level

$$| F = 3 \;\; M = 3 >_{P_{3/2}} = | 3/2 \;\; 1 \;\; 1/2 >_{P_{3/2}}$$

$$| F = 3 \;\; M = 2 >_{P_{3/2}} = \frac{1}{\sqrt{6}} (\sqrt{3} \; | 1/2 \;\; 1 \;\; 1/2 >_{P_{3/2}} + \sqrt{2} \; | 3/2 \;\; 0 \;\; 1/2 >_{P_{3/2}}$$

$$+ | 3/2 \;\; 1 \;\; -1/2 >_{P_{3/2}})$$

$$| F = 3 \;\; M = 1 >_{P_{3/2}} = \frac{1}{\sqrt{5}} (| -1/2 \;\; 1 \;\; 1/2 >_{P_{3/2}} + \frac{1}{\sqrt{3}} | 3/2 \;\; -1 \;\; 1/2 >_{P_{3/2}}$$

$$+ \sqrt{\frac{2}{3}} | 3/2 \;\; 0 \;\; -1/2 >_{P_{3/2}} + \sqrt{2} \; | 1/2 \;\; 0 \;\; 1/2 >_{P_{3/2}}$$

$$+ |1/2 \;\; 1 \;\; -1/2 >_{P_{3/2}})$$

$$| F = 3 \;\; M = 0 >_{P_{3/2}} = \frac{1}{2\sqrt{5}} (| -3/2 \;\; 1 \;\; 1/2 >_{P_{3/2}} + \sqrt{6} \; | -1/2 \;\; 0 \;\; 1/2 >_{P_{3/2}}$$

$$+ \sqrt{3} \; | -1/2 \;\; 1 \;\; -1/2 >_{P_{3/2}} + \sqrt{3} \; | 1/2 \;\; -1 \;\; 1/2 >_{P_{3/2}}$$

$$+ \sqrt{6} \; | 1/2 \;\; 0 \;\; -1/2 >_{P_{3/2}} + | 3/2 \;\; -1 \;\; -1/2 >_{P_{3/2}})$$

$$| F = 3 \;\; M = -1 >_{P_{3/2}} = \frac{1}{\sqrt{5}} (| 1/2 \;\; -1 \;\; -1/2 >_{P_{3/2}}$$

$$+ \frac{1}{\sqrt{3}} | -3/2 \;\; 1 \;\; -1/2 >_{P_{3/2}} + \sqrt{\frac{2}{3}} | -3/2 \;\; 0 \;\; 1/2 >_{P_{3/2}}$$

$$+ \sqrt{2} \; | -1/2 \;\; 0 \;\; -1/2 >_{P_{3/2}} + |-1/2 \;\; -1 \;\; 1/2 >_{P_{3/2}})$$

$$| F = 3 \;\; M = -2 >_{P_{3/2}} = \frac{1}{\sqrt{6}} (\sqrt{3} \; | -1/2 \;\; -1 \;\; -1/2 >_{P_{3/2}}$$

$$+ \sqrt{2} \; | -3/2 \;\; 0 \;\; -1/2 >_{P_{3/2}} + | -3/2 \;\; -1 \;\; 1/2 >_{P_{3/2}})$$

$$| F = 3 \;\; M = -3 >_{P_{3/2}} = | -3/2 \;\; -1 \;\; -1/2 >_{P_{3/2}}$$

For the F = 2 hyperfine level we have

$$|\, F=2\ \ M=2 \rangle_{P_{3/2}} = \frac{1}{\sqrt{6}} \left(\sqrt{3} \,|\, 1/2\ \ 1\ \ 1/2 \rangle_{P_{3/2}} - \sqrt{2} \,|\, 3/2\ \ 0\ \ 1/2 \rangle_{P_{3/2}} \right.$$

$$\left. - \,|\, 3/2\ \ 1\ \ -1/2 \rangle_{P_{3/2}} \right)$$

$$|\, F=2\ \ M=1 \rangle_{P_{3/2}} = \frac{1}{\sqrt{6}} \left(\sqrt{3} \,|\, -1/2\ \ 1\ \ 1/2 \rangle_{P_{3/2}} - \,|\, 3/2\ \ -1\ \ 1/2 \rangle_{P_{3/2}} \right.$$

$$\left. - \sqrt{2} \,|\, 3/2\ \ 0\ \ -1/2 \rangle_{P_{3/2}} \right)$$

$$|\, F=2\ \ M=0 \rangle_{P_{3/2}} = \frac{1}{2} \left(\,|\, -3/2\ \ 1\ \ 1/2 \rangle_{P_{3/2}} + \sqrt{\frac{2}{3}} \,|\, -1/2\ \ 0\ \ 1/2 \rangle_{P_{3/2}} \right.$$

$$+ \frac{1}{\sqrt{3}} \,|\, -1/2\ \ 1\ \ -1/2 \rangle_{P_{3/2}} - \frac{1}{\sqrt{3}} \,|\, 1/2\ \ -1\ \ 1/2 \rangle_{P_{3/2}}$$

$$\left. - \sqrt{\frac{2}{3}} \,|\, 1/2\ \ 0\ \ -1/2 \rangle_{P_{3/2}} - \,|\, 3/2\ \ -1\ \ -1/2 \rangle_{P_{3/2}} \right)$$

$$|\, F=2\ \ M=-1 \rangle_{P_{3/2}} = \frac{1}{\sqrt{6}} \left(-\sqrt{3} \,|\, 1/2\ \ -1\ \ -1/2 \rangle_{P_{3/2}} \right.$$

$$\left. + \,|\, -3/2\ \ 1\ \ -1/2 \rangle_{P_{3/2}} + \sqrt{2} \,|\, -3/2\ \ 0\ \ 1/2 \rangle_{P_{3/2}} \right)$$

$$|\, F=2\ \ M=-2 \rangle_{P_{3/2}} = \frac{1}{\sqrt{6}} \left(-\sqrt{3} \,|\, -1/2\ \ -1\ \ -1/2 \rangle_{P_{3/2}} \right.$$

$$\left. + \sqrt{2} \,|\, -3/2\ \ 0\ \ -1/2 \rangle_{P_{3/2}} + \,|\, -3/2\ \ -1\ \ 1/2 \rangle_{P_{3/2}} \right)$$

For the F = 1 hyperfine level we have

$$|\, F=1\ \ M=1 \rangle_{P_{3/2}} = \frac{1}{\sqrt{10}} \left(\sqrt{3} \,|\, -1/2\ \ 1\ \ 1/2 \rangle_{P_{3/2}} + \,|\, 3/2\ \ -1\ \ 1/2 \rangle_{P_{3/2}} \right.$$

$$+ \sqrt{2} \,|\, 3/2\ \ 0\ \ -1/2 \rangle_{P_{3/2}} - \frac{2\sqrt{2}}{\sqrt{3}} \,|\, 1/2\ \ 0\ \ 1/2 \rangle_{P_{3/2}}$$

$$\left. - \frac{2}{\sqrt{3}} \,|\, 1/2\ \ 1\ \ -1/2 \rangle_{P_{3/2}} \right)$$

$$|\, F=1\ \ M=0 \rangle_{P_{3/2}} = \frac{1}{2\sqrt{5}} \left(3 \,|\, -3/2\ \ 1\ \ 1/2 \rangle_{P_{3/2}} - \sqrt{\frac{2}{3}} \,|\, -1/2\ \ 0\ \ 1/2 \rangle_{P_{3/2}} \right.$$

$$\left. - \frac{1}{\sqrt{3}} \,|\, -1/2\ \ 1\ \ -1/2 \rangle_{P_{3/2}} - \frac{1}{\sqrt{3}} \,|\, 1/2\ \ -1\ \ 1/2 \rangle_{P_{3/2}} \right)$$

$$- \sqrt{\frac{2}{3}} \mid 1/2 \;\; 0 \;\; -1/2 >_{P_{3/2}} + 3 \mid 3/2 \;\; -1 \;\; -1/2 >_{P_{3/2}})$$

$$\mid F = 1 \;\; M = -1 >_{P_{3/2}} = \frac{1}{\sqrt{10}} (\sqrt{3} \mid 1/2 \;\; -1 \;\; -1/2 >_{P_{3/2}}$$

$$+ \mid -3/2 \;\; 1 \;\; -1/2 >_{P_{3/2}} + \sqrt{2} \mid -3/2 \;\; 0 \;\; 1/2 >_{P_{3/2}}$$

$$- \frac{2\sqrt{2}}{\sqrt{3}} \mid -1/2 \;\; 0 \;\; -1/2 >_{P_{3/2}} - \frac{2}{\sqrt{3}} \mid -1/2 \;\; -1 \;\; 1/2 >_{P_{3/2}})$$

For the F = 0 hyperfine level we have

$$\mid F = 0 \;\; M = 0 >_{P_{3/2}} = \frac{1}{2} (\mid -3/2 \;\; 1 \;\; 1/2 >_{P_{3/2}} - \sqrt{\frac{2}{3}} \mid -1/2 \;\; 0 \;\; 1/2 >_{P_{3/2}}$$

$$- \frac{1}{\sqrt{3}} \mid -1/2 \;\; 1 \;\; -1/2 >_{P_{3/2}} + \frac{1}{\sqrt{3}} \mid 1/2 \;\; -1 \;\; 1/2 >_{P_{3/2}}$$

$$+ \sqrt{\frac{2}{3}} \mid 1/2 \;\; 0 \;\; -1/2 >_{P_{3/2}} - \mid 3/2 \;\; -1 \;\; -1/2 >_{P_{3/2}})$$

5.4 Spontaneous Emission Rates for Sodium

Now that we have the wavefunctions for the 3S ground states and 3P excited states we will look at the various paths by which an excited state can decay to the ground state and the various probabilities for that to happen.

Let us write the position vector for the outer electron of the sodium atom as

$$\mathbf{r} = r_0 \mathbf{e}_z + r_+ \mathbf{e}_- + r_- \mathbf{e}_+ \qquad (5.4\text{-}1)$$

where

$$r_0 = z \qquad r_+ = \frac{1}{\sqrt{2}} (x + iy) \qquad r_- = \frac{1}{\sqrt{2}} (x - iy) \qquad (5.4\text{-}2)$$

and

$$\mathbf{e}_- = \frac{1}{\sqrt{2}} (\mathbf{e}_x - i\mathbf{e}_y) \qquad \mathbf{e}_+ = \frac{1}{\sqrt{2}} (\mathbf{e}_x + i\mathbf{e}_y) \qquad (5.4\text{-}3)$$

with $\mathbf{e}_i$ being unit vectors in the i direction.

For sodium the matrix element[18]

$$| < 3P, m = 0 | r_0 | 3S > | = 2.51a_0 \equiv z_0 \qquad (5.4\text{-}4)$$

where a_0 is the Bohr radius and we are looking only at the spatial part of the wavefunction and neglecting the electron spin and the nuclear spin. Likewise

$$| < 3P, m = 1 | r_+ | 3S > | = z_0 = | < 3P, m = -1 | r_- | 3S > | \qquad (5.4\text{-}5)$$

Let us define

$$\mu_{12}^2 = e^2 | < r >_{12} |^2 \qquad (5.4\text{-}6)$$

where e is the electron charge and

$$| < r >_{12} |^2 = | r_0 |_{12}^2 + | r_+ |_{12}^2 + | r_- |_{12}^2 \qquad (5.4\text{-}7)$$

The branching ratio BR can be defined as $\mu_{12}^2 / e^2 z_0^2$.

We can now calculate the branching ratios for the various excited states using the wavefunctions of the previous section and the above matrix elements.

TRANSITION			BR
$3P_{3/2}(F = 3, m = 3)$	→	$3S_{1/2}(F = 2, m = 2)$	1
$3P_{3/2}(F = 3, m = 2)$	→	$3S_{1/2}(F = 2, m = 2)$	1/3
	→	$3S_{1/2}(F = 2, m = 1)$	2/3
$3P_{3/2}(F = 3, m = 1)$	→	$3S_{1/2}(F = 2, m = 2)$	1/15
	→	$3S_{1/2}(F = 2, m = 1)$	8/15
	→	$3S_{1/2}(F = 2, m = 0)$	6/15
$3P_{3/2}(F = 3, m = 0)$	→	$3S_{1/2}(F = 2, m = 1)$	1/5
	→	$3S_{1/2}(F = 2, m = 0)$	3/5
	→	$3S_{1/2}(F = 2, m = -1)$	1/5
$3P_{3/2}(F = 2, m = 2)$	→	$3S_{1/2}(F = 2, m = 2)$	1/3
	→	$3S_{1/2}(F = 2, m = 1)$	1/6
	→	$3S_{1/2}(F = 1, m = 1)$	1/2

$3P_{3/2}(F = 2, m = 1)$	$\rightarrow 3S_{1/2}(F = 2, m = 2)$	1/6
	$\rightarrow 3S_{1/2}(F = 2, m = 1)$	1/12
	$\rightarrow 3S_{1/2}(F = 2, m = 0)$	1/4
	$\rightarrow 3S_{1/2}(F = 1, m = 1)$	1/4
	$\rightarrow 3S_{1/2}(F = 1, m = 0)$	1/4
$3P_{3/2}(F = 2, m = 0)$	$\rightarrow 3S_{1/2}(F = 2, m = 1)$	1/4
	$\rightarrow 3S_{1/2}(F = 2, m = 0)$	0
	$\rightarrow 3S_{1/2}(F = 2, m = -1)$	1/4
	$\rightarrow 3S_{1/2}(F = 1, m = 1)$	1/12
	$\rightarrow 3S_{1/2}(F = 1, m = 0)$	1/3
	$\rightarrow 3S_{1/2}(F = 1, m = -1)$	1/12
$3P_{3/2}(F = 1, m = 1)$	$\rightarrow 3S_{1/2}(F = 2, m = 2)$	1/10
	$\rightarrow 3S_{1/2}(F = 2, m = 1)$	1/20
	$\rightarrow 3S_{1/2}(F = 2, m = 0)$	1/60
	$\rightarrow 3S_{1/2}(F = 1, m = 1)$	5/12
	$\rightarrow 3S_{1/2}(F = 1, m = 0)$	5/12
$3P_{3/2}(F = 1, m = 0)$	$\rightarrow 3S_{1/2}(F = 2, m = 1)$	1/20
	$\rightarrow 3S_{1/2}(F = 2, m = 0)$	1/15
	$\rightarrow 3S_{1/2}(F = 2, m = -1)$	1/20
	$\rightarrow 3S_{1/2}(F = 1, m = 1)$	5/12
	$\rightarrow 3S_{1/2}(F = 1, m = 0)$	0
	$\rightarrow 3S_{1/2}(F = 1, m = -1)$	5/12
$3P_{3/2}(F = 0, m = 0)$	$\rightarrow 3S_{1/2}(F = 1, m = 1)$	1/3
	$\rightarrow 3S_{1/2}(F = 1, m = 0)$	1/3
	$\rightarrow 3S_{1/2}(F = 1, m = -1)$	1/3

$3P_{1/2}(F = 2, m = 2)$	$\rightarrow 3S_{1/2}(F = 2, m = 2)$	1/3
	$\rightarrow 3S_{1/2}(F = 2, m = 1)$	1/6
	$\rightarrow 3S_{1/2}(F = 1, m = 1)$	1/2
$3P_{1/2}(F = 2, m = 1)$	$\rightarrow 3S_{1/2}(F = 2, m = 2)$	1/6
	$\rightarrow 3S_{1/2}(F = 2, m = 1)$	1/12
	$\rightarrow 3S_{1/2}(F = 2, m = 0)$	1/4
	$\rightarrow 3S_{1/2}(F = 1, m = 1)$	1/4
	$\rightarrow 3S_{1/2}(F = 1, m = 0)$	1/4
$3P_{1/2}(F = 2, m = 0)$	$\rightarrow 3S_{1/2}(F = 2, m = 1)$	1/4
	$\rightarrow 3S_{1/2}(F = 2, m = 0)$	0
	$\rightarrow 3S_{1/2}(F = 2, m = -1)$	1/4
	$\rightarrow 3S_{1/2}(F = 1, m = 1)$	1/12
	$\rightarrow 3S_{1/2}(F = 1, m = 0)$	1/3
	$\rightarrow 3S_{1/2}(F = 1, m = -1)$	1/12
$3P_{1/2}(F = 1, m = 1)$	$\rightarrow 3S_{1/2}(F = 2, m = 2)$	1/2
	$\rightarrow 3S_{1/2}(F = 2, m = 1)$	1/4
	$\rightarrow 3S_{1/2}(F = 2, m = 0)$	1/12
	$\rightarrow 3S_{1/2}(F = 1, m = 1)$	1/12
	$\rightarrow 3S_{1/2}(F = 1, m = 0)$	1/12
$3P_{1/2}(F = 1, m = 0)$	$\rightarrow 3S_{1/2}(F = 2, m = 1)$	1/4
	$\rightarrow 3S_{1/2}(F = 2, m = 0)$	1/3
	$\rightarrow 3S_{1/2}(F = 2, m = -1)$	1/4
	$\rightarrow 3S_{1/2}(F = 1, m = 1)$	1/12
	$\rightarrow 3S_{1/2}(F = 1, m = 0)$	0
	$\rightarrow 3S_{1/2}(F = 1, m = -1)$	1/12

5.5 Absorption Cross Section for Sodium

Now that we know the spontaneous emission rates for the 3P excited state, we need to know the stimulated absorption rates in the presence of an applied electromagnetic field which is either circularly or linearly polarized. Let us define

$$\mu_i^2 = e^2 \mid < \mathbf{r} \cdot \mathbf{e}_i >_{12} \mid^2 \qquad (5.5\text{-}1)$$

The normalized absorption cross section ACS, defined as $\mu_i^2 / e^2 z_0^2$, will now be considered for i = +. Using the wavefunctions previously calculated we obtain

TRANSITION		ACS
$3S_{1/2}(F = 2, m = 2)$	$\rightarrow 3P_{3/2}(F = 3, m = 3)$	1
$3S_{1/2}(F = 2, m = 1)$	$\rightarrow 3P_{3/2}(F = 3, m = 2)$	2/3
	$\rightarrow 3P_{3/2}(F = 2, m = 2)$	1/6
	$\rightarrow 3P_{1/2}(F = 2, m = 2)$	1/6
$3S_{1/2}(F = 2, m = 0)$	$\rightarrow 3P_{3/2}(F = 3, m = 1)$	6/15
	$\rightarrow 3P_{3/2}(F = 2, m = 1)$	1/4
	$\rightarrow 3P_{3/2}(F = 1, m = 1)$	1/60
	$\rightarrow 3P_{1/2}(F = 2, m = 1)$	1/4
	$\rightarrow 3P_{1/2}(F = 1, m = 1)$	1/12
$3S_{1/2}(F = 2, m = -1)$	$\rightarrow 3P_{3/2}(F = 3, m = 0)$	1/5
	$\rightarrow 3P_{3/2}(F = 2, m = 0)$	1/4
	$\rightarrow 3P_{3/2}(F = 1, m = 0)$	1/20
	$\rightarrow 3P_{1/2}(F = 2, m = 0)$	1/4
	$\rightarrow 3P_{1/2}(F = 1, m = 0)$	1/4
$3S_{1/2}(F = 2, m = -2)$	$\rightarrow 3P_{3/2}(F = 3, m = -1)$	1/15
	$\rightarrow 3P_{3/2}(F = 2, m = -1)$	1/6
	$\rightarrow 3P_{3/2}(F = 1, m = -1)$	1/10
	$\rightarrow 3P_{1/2}(F = 2, m = -1)$	1/6

	$\rightarrow 3P_{1/2}(F = 1, m = -1)$	1/2
$3S_{1/2}(F = 1, m = 1)$	$\rightarrow 3P_{3/2}(F = 2, m = 2)$	1/2
	$\rightarrow 3P_{1/2}(F = 2, m = 2)$	1/2
$3S_{1/2}(F = 1, m = 0)$	$\rightarrow 3P_{3/2}(F = 2, m = 1)$	1/4
	$\rightarrow 3P_{3/2}(F = 1, m = 1)$	5/12
	$\rightarrow 3P_{1/2}(F = 2, m = 1)$	1/4
	$\rightarrow 3P_{1/2}(F = 1, m = 1)$	1/12
$3S_{1/2}(F = 1, m = -1)$	$\rightarrow 3P_{3/2}(F = 2, m = 0)$	1/12
	$\rightarrow 3P_{3/2}(F = 1, m = 0)$	5/12
	$\rightarrow 3P_{3/2}(F = 0, m = 0)$	1/3
	$\rightarrow 3P_{1/2}(F = 2, m = 0)$	1/12
	$\rightarrow 3P_{1/2}(F = 1, m = 0)$	1/12

The normalized absorption cross section ACS will now be considered for i = 0. Using the wavefunctions previously calculated we obtain

TRANSITION		ACS
$3S_{1/2}(F = 2, m = 2)$	$\rightarrow 3P_{3/2}(F = 3, m = 2)$	1/3
	$\rightarrow 3P_{3/2}(F = 2, m = 2)$	1/3
	$\rightarrow 3P_{1/2}(F = 2, m = 2)$	1/3
$3S_{1/2}(F = 2, m = 1)$	$\rightarrow 3P_{3/2}(F = 3, m = 1)$	8/15
	$\rightarrow 3P_{3/2}(F = 2, m = 1)$	1/12
	$\rightarrow 3P_{3/2}(F = 1, m = 1)$	1/20
	$\rightarrow 3P_{1/2}(F = 2, m = 1)$	1/12
	$\rightarrow 3P_{1/2}(F = 1, m = 1)$	1/4
$3S_{1/2}(F = 2, m = 0)$	$\rightarrow 3P_{3/2}(F = 3, m = 0)$	3/5
	$\rightarrow 3P_{3/2}(F = 2, m = 0)$	0
	$\rightarrow 3P_{3/2}(F = 1, m = 0)$	1/15

	$\rightarrow 3P_{1/2}(F = 2, m = 0)$	0
	$\rightarrow 3P_{1/2}(F = 1, m = 0)$	1/3
$3S_{1/2}(F = 2, m = -1)$	$\rightarrow 3P_{3/2}(F = 3, m = -1)$	8/15
	$\rightarrow 3P_{3/2}(F = 2, m = -1)$	1/12
	$\rightarrow 3P_{3/2}(F = 1, m = -1)$	1/20
	$\rightarrow 3P_{1/2}(F = 2, m = -1)$	1/12
	$\rightarrow 3P_{1/2}(F = 1, m = -1)$	1/4
$3S_{1/2}(F = 2, m = -2)$	$\rightarrow 3P_{3/2}(F = 3, m = -2)$	1/3
	$\rightarrow 3P_{3/2}(F = 2, m = -2)$	1/3
	$\rightarrow 3P_{1/2}(F = 2, m = -2)$	1/3
$3S_{1/2}(F = 1, m = 1)$	$\rightarrow 3P_{3/2}(F = 2, m = 1)$	1/4
	$\rightarrow 3P_{3/2}(F = 1, m = 1)$	5/12
	$\rightarrow 3P_{1/2}(F = 2, m = 1)$	1/4
	$\rightarrow 3P_{1/2}(F = 1, m = 1)$	1/12
$3S_{1/2}(F = 1, m = 0)$	$\rightarrow 3P_{3/2}(F = 2, m = 0)$	1/3
	$\rightarrow 3P_{3/2}(F = 1, m = 0)$	0
	$\rightarrow 3P_{3/2}(F = 0, m = 0)$	1/3
	$\rightarrow 3P_{1/2}(F = 2, m = 0)$	1/3
	$\rightarrow 3P_{1/2}(F = 1, m = 0)$	0
$3S_{1/2}(F = 1, m = -1)$	$\rightarrow 3P_{3/2}(F = 2, m = -1)$	1/4
	$\rightarrow 3P_{3/2}(F = 1, m = -1)$	5/12
	$\rightarrow 3P_{1/2}(F = 2, m = -1)$	1/4
	$\rightarrow 3P_{1/2}(F = 1, m = -1)$	1/12

For $i = -$, we will now consider the normalized absorption cross section ACS. Using the wavefunctions previously calculated we obtain

TRANSITION			ACS
$3S_{1/2}(F = 2, m = -2)$	→	$3P_{3/2}(F = 3, m = -3)$	1
$3S_{1/2}(F = 2, m = -1)$	→	$3P_{3/2}(F = 3, m = -2)$	2/3
	→	$3P_{3/2}(F = 2, m = -2)$	1/6
	→	$3P_{1/2}(F = 2, m = -2)$	1/6
$3S_{1/2}(F = 2, m = 0)$	→	$3P_{3/2}(F = 3, m = -1)$	6/15
	→	$3P_{3/2}(F = 2, m = -1)$	1/4
	→	$3P_{3/2}(F = 1, m = -1)$	1/60
	→	$3P_{1/2}(F = 2, m = -1)$	1/4
	→	$3P_{1/2}(F = 1, m = -1)$	1/12
$3S_{1/2}(F = 2, m = 1)$	→	$3P_{3/2}(F = 3, m = 0)$	1/5
	→	$3P_{3/2}(F = 2, m = 0)$	1/4
	→	$3P_{3/2}(F = 1, m = 0)$	1/20
	→	$3P_{1/2}(F = 2, m = 0)$	1/4
	→	$3P_{1/2}(F = 1, m = 0)$	1/4
$3S_{1/2}(F = 2, m = 2)$	→	$3P_{3/2}(F = 3, m = 1)$	1/15
	→	$3P_{3/2}(F = 2, m = 1)$	1/6
	→	$3P_{3/2}(F = 1, m = 1)$	1/10
	→	$3P_{1/2}(F = 2, m = 1)$	1/6
	→	$3P_{1/2}(F = 1, m = 1)$	1/2
$3S_{1/2}(F = 1, m = -1)$	→	$3P_{3/2}(F = 2, m = -2)$	1/2
	→	$3P_{1/2}(F = 2, m = -2)$	1/2
$3S_{1/2}(F = 1, m = 0)$	→	$3P_{3/2}(F = 2, m = -1)$	1/4
	→	$3P_{3/2}(F = 1, m = -1)$	5/12
	→	$3P_{1/2}(F = 2, m = -1)$	1/4
	→	$3P_{1/2}(F = 1, m = -1)$	1/12

$3S_{1/2}(F = 1, m = 1)$	$\rightarrow 3P_{3/2}(F = 2, m = 0)$	1/12
	$\rightarrow 3P_{3/2}(F = 1, m = 0)$	5/12
	$\rightarrow 3P_{3/2}(F = 0, m = 0)$	1/3
	$\rightarrow 3P_{1/2}(F = 2, m = 0)$	1/12
	$\rightarrow 3P_{1/2}(F = 1, m = 0)$	1/12

5.6 Vapor Pressure and Density of Sodium

In our experiments, sodium vapor is the nonlinear medium. It is obtained by putting a piece of sodium metal in the sidearm of an evacuated cylindrical quartz cell. The cell is wrapped with heater wire which heats the cell to provide the sodium vapor . Sodium has a melting point of 372° K. The equilibrium between the liquid and vapor phases of sodium is given by

$$\log_{10} p = 10.86423 - \frac{5619.406}{T} - 1.04111 \log_{10} T + 3.45 \times 10^{-6} T \qquad (5.6\text{-}1)$$

where p is in torr and T is in degrees Kelvin[11]. Using this vapor pressure the atomic density is

$$N = 9.66 \times 10^{18} \frac{p}{T}. \qquad (5.6\text{-}2)$$

The table below gives some examples of pressure and density in the temperature range of interest for our experiments.

T(°C)	p(torr)	N(cm^{-3})
100	1.33×10^{-7}	3.43×10^{9}
150	7.03×10^{-6}	1.60×10^{11}
200	1.59×10^{-4}	3.24×10^{12}
250	1.96×10^{-3}	3.61×10^{13}
300	1.54×10^{-2}	2.60×10^{14}
350	8.65×10^{-2}	1.34×10^{15}

400	3.74×10^{-1}	5.36×10^{15}

5.7 Linewidths of Sodium

Using the matrix element μ_{12}^2 defined in section 5.4, the spontaneous transition rate can be calculated from

$$W = \frac{64\pi^4}{3} \frac{\mu_{12}^2}{hc} \frac{(\hbar\omega_0)^3}{(hc)^3} c \tag{5.7-1}$$

Simplifying this formula we obtain

$$W = 2.67 \times \frac{10^9}{\text{sec}} \frac{(z_0)^2}{(a_0)^2} \left(\frac{\hbar\omega_0}{13.6\text{eV}} \right)^3 \tag{5.7-2}$$

For the 3S - 3P transition in sodium, $W = .623 \times 10^8/\text{sec}$, using the value of z_0 from section 5.4. . This gives a natural lifetime of $\tau = 1/W = 16 \times 10^{-9}$ sec.

The natural linewidth, full width half maximum , is

$$\Delta \nu_N = \frac{1}{2\pi\tau} = 10 \text{ MHz} \tag{5.7-3}$$

The other important linewidth to consider is the Doppler linewidth. The full width at half maximum for the Doppler profile in frequency space is given by

$$\Delta \nu_D = 2\nu_0 \sqrt{\frac{2kT}{Mc^2} \ln 2} \tag{5.7-4}$$

with $\nu_0 = \omega_0/2\pi$, T is the temperature of the gas, and M is the mass of one sodium atom. This can be simplified to give

$$\Delta \nu_D = 2\nu_0 \left(3.58 \times 10^{-7} \right) \sqrt{\frac{T}{M}} \tag{5.7-5}$$

with T in °K, M in atomic mass units, and $\Delta \nu_D$ and ν_0 in Hz.

If we consider the gas to have a Maxwell-Boltzman distribution of velocities we can calculate the average speed of an atom which is constrained to a plane. This speed gives us a good indication of the speed at which atoms are moving perpendicu-

lar to a laser beam incident on the gas. The average speed $\bar{v}$ is given by

$$\bar{v} = \sqrt{\frac{\pi kT}{2M}} \tag{5.7-6}$$

This can be simplified to give

$$\bar{v} = 1.143 \times 10^4 \text{ cm/sec} \sqrt{\frac{T}{M}} \tag{5.7-7}$$

where T is in degrees Kelvin and M is in atomic mass units.

Some examples of Doppler linewidths at various temperatures as well as the average speed of an atom in a plane are given below for sodium.

T(°C)	$\Delta \nu_D$ (GHz)	$\bar{v}$ (cm/sec)
100	1.47	4.60×10^4
150	1.56	4.90×10^4
200	1.65	5.18×10^4
250	1.74	5.45×10^4
300	1.82	5.71×10^4
350	1.90	5.95×10^4
400	1.97	6.18×10^4

5.8 Hyperfine Optical Pumping

As is already evident, the 3S - 3P transition in sodium is anything but a two level transition. The major problem in using sodium is that the hyperfine optical pumping transfers the population of the ground state resonant with the laser into the other ground state.

The two ground state hyperfine levels[6,7] are separated by 1.77 GHz, which is much larger than the natural linewidth of sodium and even larger than the Doppler linewidth at the temperatures of interest. This means that a laser can be tuned between only one hyperfine level of the ground state and the excited states. Except

for the case of using circularly polarized light, $\mathbf{e}_+$, to excite the $3S_{1/2}(F = 2, m = 2) \rightarrow 3P_{3/2}(F = 3, m = 3)$ transition or $\mathbf{e}_-$ light to excite the $3S_{1/2}(F = 2, m = -2) \rightarrow 3P_{3/2}(F = 3, m = -3)$ transition, all the Zeeman sublevels of the ground state will be excited to the 3P states which will populate both the F = 2 and F = 1 ground states after several absorptions. Atoms which populate the ground state the laser is not resonant with are lost to any nonlinear interaction such as phase conjugation.

To demonstrate the problems of optical pumping, we will consider the case of a laser linearly polarized with its electric field along the z direction. The laser will be tuned to the $3S_{1/2}(F = 2) \rightarrow 3P_{1/2}(F = 2)$ transition. We will neglect Doppler effects and assume that the laser is resonant only with this transition and all other stimulated transitions have zero probability of occurring.

The laser intensity will be I, the line center absorption cross-section σ, the natural lifetime τ and $h\nu$ will be the energy of a laser photon. The ground state populations are denoted by

$$G_{ij} \equiv 3S_{1/2}(F = i, m = j) \tag{5.8-1}$$

and the excited state populations by

$$E_{ij} \equiv 3P_{1/2}(F = i, m = j) \tag{5.8-2}$$

We will assume an initial population of one atom in each Zeeman sublevel of the ground state. The excited states will be unpopulated. Using the stimulated and spontaneous transition rates derived in earlier sections, the rate equations become

$$\frac{dE_{22}}{dt} = \frac{1}{3}\frac{\sigma I}{h\nu}[G_{22} - E_{22}] - \frac{E_{22}}{\tau}$$

$$\frac{dE_{21}}{dt} = \frac{1}{12}\frac{\sigma I}{h\nu}[G_{21} - E_{21}] - \frac{E_{21}}{\tau}$$

$$\frac{dE_{20}}{dt} = -\frac{E_{20}}{\tau}$$

$$\frac{dE_{2-1}}{dt} = \frac{1}{12}\frac{\sigma I}{h\nu}[G_{2-1} - E_{2-1}] - \frac{E_{2-1}}{\tau}$$

$$\frac{dE_{2-2}}{dt} = \frac{1}{3}\frac{\sigma I}{h\nu}[G_{2-2} - E_{2-2}] - \frac{E_{2-2}}{\tau}$$

$$\frac{dG_{22}}{dt} = \frac{1}{3}\frac{\sigma I}{h\nu}[E_{22} - G_{22}] + \frac{E_{21} + 2E_{22}}{6\tau}$$

$$\frac{dG_{21}}{dt} = \frac{1}{12}\frac{\sigma I}{h\nu}[E_{21} - G_{21}] + \frac{E_{21} + 2E_{22}}{12\tau}$$

$$\frac{dG_{20}}{dt} = \frac{E_{21} + E_{2-1}}{4\tau}$$

$$\frac{dG_{2-1}}{dt} = \frac{1}{12}\frac{\sigma I}{h\nu}[E_{2-1} - G_{2-1}] + \frac{E_{2-1} + 2E_{2-2}}{12\tau}$$

$$\frac{dG_{2-2}}{dt} = \frac{1}{3}\frac{\sigma I}{h\nu}[E_{2-2} - G_{2-2}] + \frac{E_{2-1} + 2E_{2-2}}{6\tau}$$

$$\frac{dG_{11}}{dt} = \frac{6E_{22} + 3E_{21} + E_{20}}{12\tau}$$

$$\frac{dG_{10}}{dt} = \frac{3E_{21} + 4E_{20} + 3E_{2-1}}{12\tau}$$

$$\frac{dG_{1-1}}{dt} = \frac{6E_{2-2} + 3E_{2-1} + E_{20}}{12\tau} \qquad (5.8\text{-}3)$$

We notice immediately that E_{20} must remain a constant. Using the initial conditions gives $E_{20} = 0$. The use of linearly polarized light gives a certain symmetry to the problem such that

$$E_{ij} = E_{i-j} \qquad G_{ij} = G_{i-j} \qquad (5.8\text{-}4)$$

We can simplify the rate equations by defining a normalized time $t_N = t/\tau$ and a normalized intensity $I_N = \sigma I\tau/3h\nu$. I_N is roughly the ratio of laser intensity to the saturation intensity of the system if it were a two level system. This yields the coupled equations

$$\frac{dE_{22}}{dt_N} = I_N(G_{22} - E_{22}) - E_{22}$$

$$\frac{dE_{21}}{dt_N} = \frac{I_N}{4}(G_{21} - E_{21}) - E_{21}$$

$$\frac{dG_{22}}{dt_N} = I_N(E_{22} - G_{22}) + \frac{1}{6}(E_{21} + 2E_{22})$$

$$\frac{dG_{21}}{dt_N} = \frac{I_N}{4}(E_{21} - G_{21}) + \frac{1}{12}(E_{21} + 2E_{22})$$

$$\frac{dG_{20}}{dt_N} = \frac{1}{2}E_{21}$$

$$\frac{dG_{11}}{dt_N} = \frac{1}{4}(2E_{22} + E_{21})$$

$$\frac{dG_{10}}{dt_N} = \frac{1}{2}E_{21} \qquad (5.8\text{-}5)$$

We now solve these equations numerically for various values of I_N. In Figs. 5.2 - 5.7 the populations of the various ground states G_{ij} and the excited states E_{ij} are plotted versus t_N for $I_N = 10, 1, 0.1$. Fig. 5.2 shows the population of G_{22} [$3S_{1/2}(F = 2, m = 2)$] versus t_N. For $I_N < 1$ the atoms absorb the light at a rate I_N, are transferred to state E_{22}, and then spontaneously decay to ground states G_{22}, G_{21}, and G_{11} at a unity rate in our normalized time system. The atoms decaying to G_{21} and G_{11} are lost to G_{22} forever. Since the absorption rate is less than or comparable to the spontaneous decay rate, the population of G_{22} is optically pumped in a time $t_N \approx 1/I_N$ as observed in Fig. 5.2.

For $I_N > 1$ the atoms still absorb the light at a rate I_N and are transferred to the excited state E_{22}. The excited states decays to the ground states G_{22} and G_{21} at a unity rate. However the spontaneous decay rate is less than the absorption rate so an excited state population builds up for $t_N < 1$. The population of G_{22} initially decays at a rate I_N. This rate decreases as the excited state population increases

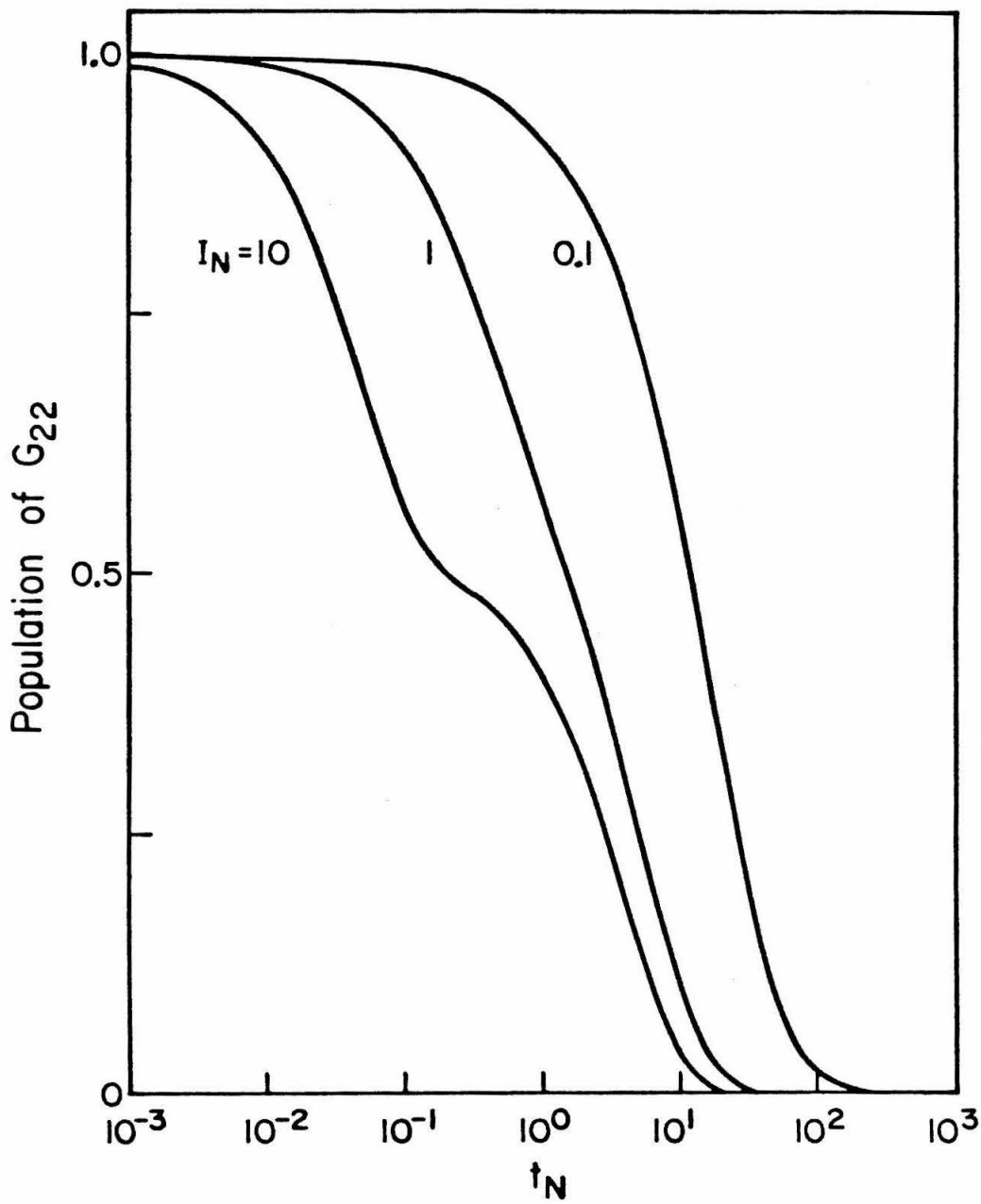

Fig. 5.2 Population of the $3S_{1/2}$ (F = 2, m = 2) ground state versus the normalized time t_N for various values of I_N.

and becomes nearly equal to the ground state population. The spontaneous decay rate then dominates and the population of G_{22} decays at a unity rate. This explains the change in decay rates shown for $I_N = 10$ in Fig. 5.2. The time dependence of the population of E_{22} [$3P_{1/2}(F = 2, m = 2)$] is shown in Fig. 5.3.

We can conclude that, for large I_N, the populations of G_{22} and E_{22} will become nearly equal in a time $t_N \approx 1/I_N$ and both will then decay at the spontaneous decay rate. Therefore $t_N \approx 1$ is the optical pumping time.

Fig. 5.4 shows the population of G_{21} [$3S_{1/2}(F = 2, m = 1)$] versus t_N. From Eqs. (5.8-5) we note that the absorption rate of G_{21} into the excited state E_{21} is $I_N/4$ so the atoms in G_{21} are not optically pumped as quickly as those of G_{22}. Also, the population of G_{21} is being increased by decay from E_{22} while losing atoms through the decay of E_{21} into the ground states G_{20}, G_{11}, and G_{10}. The optical pumping rate is limited by the minimum of $[I_N, 1]$. The population of E_{21} [$3P_{1/2}(F = 2, m = 1)$] is plotted versus t_N in Fig. 5.5. It is quite similar to Fig. 5.3, for the state E_{22}, except for the slower accumulation time due to the reduced absorption rate and the smaller amplitude of the maximum population attained.

In Fig. 5.6, the population of G_{20} [$3S_{1/2}(F = 2, m = 0)$] is shown versus t_N. For our choice of initial conditions, the population of G_{10} [$3S_{1/2}(F = 1, m = 0)$] is identical with the population of G_{20} for all values of t_N. The population of G_{20} is increased by spontaneous decay from E_{21}, it therefore starts at unity and grows at a rate which is the minimum of the absorption rate, $I_N/4$, into E_{21} or the spontaneous decay rate, 1, from E_{21}. The population reaches an equilibrium value of 1.714. G_{20} is resonant with the laser but does not have any allowed transitions to the excited states for the polarized light used. Thus, any atoms which populate this energy level no longer interact with the laser. G_{10} is not resonant with the laser and all atoms which accumulate here are lost to further interactions.

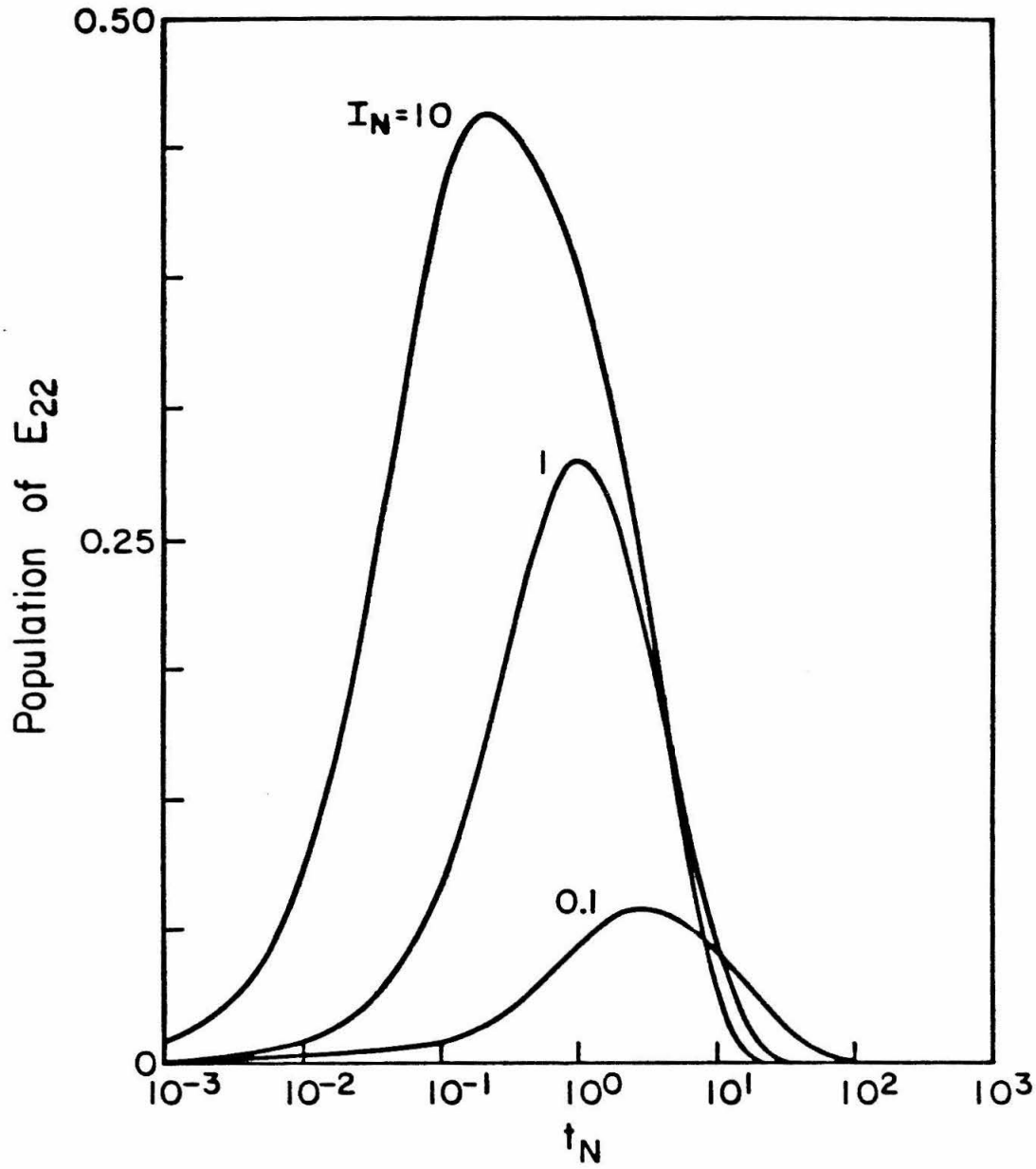

Fig. 5.3 Population of the $3P_{1/2}$ (F = 2, m = 2) excited state versus the normalized time t_N for various values of I_N.

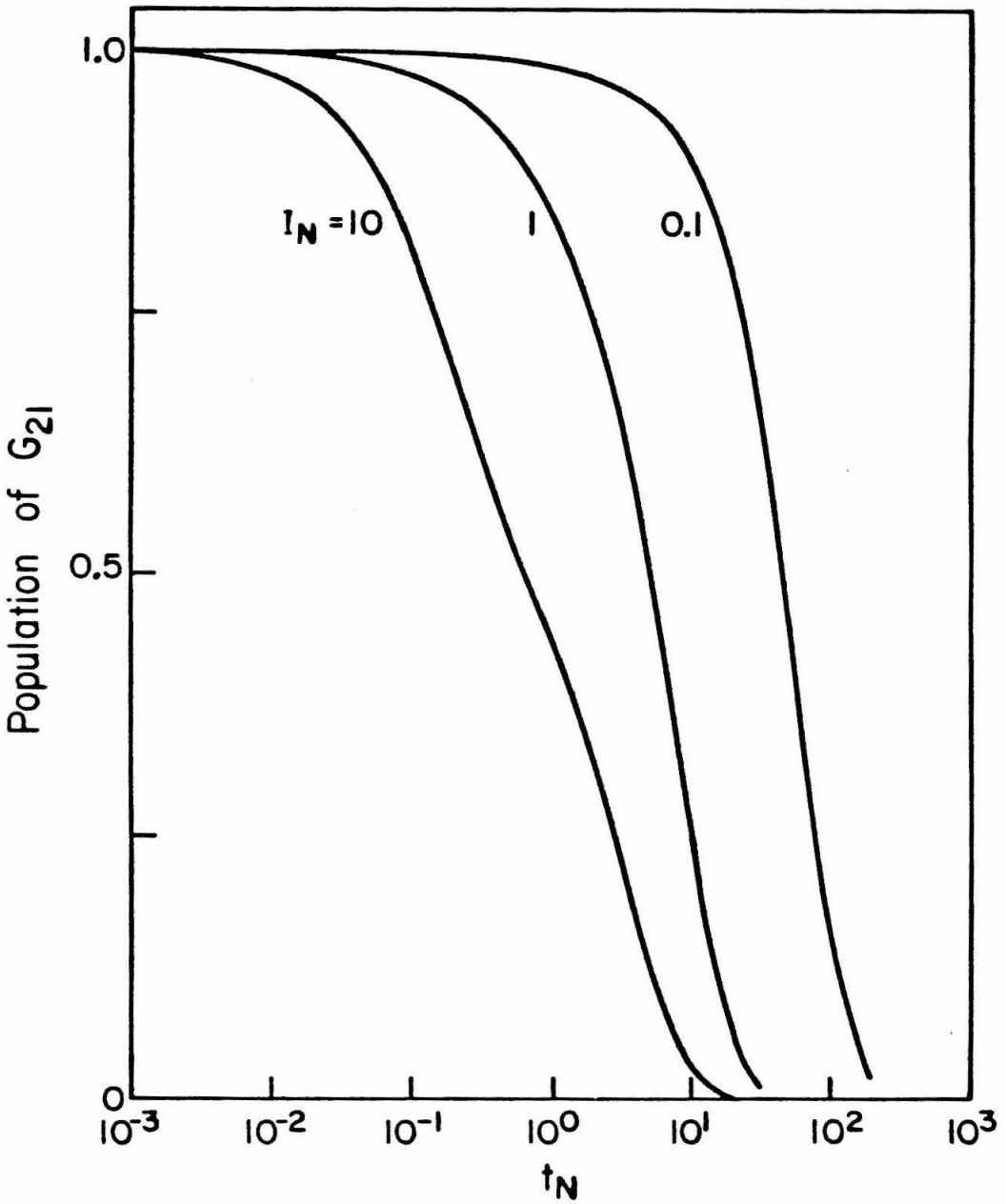

Fig. 5.4 Population of the $3S_{1/2}$ (F = 2, m = 1) ground state versus the normalized time t_N for various values of I_N.

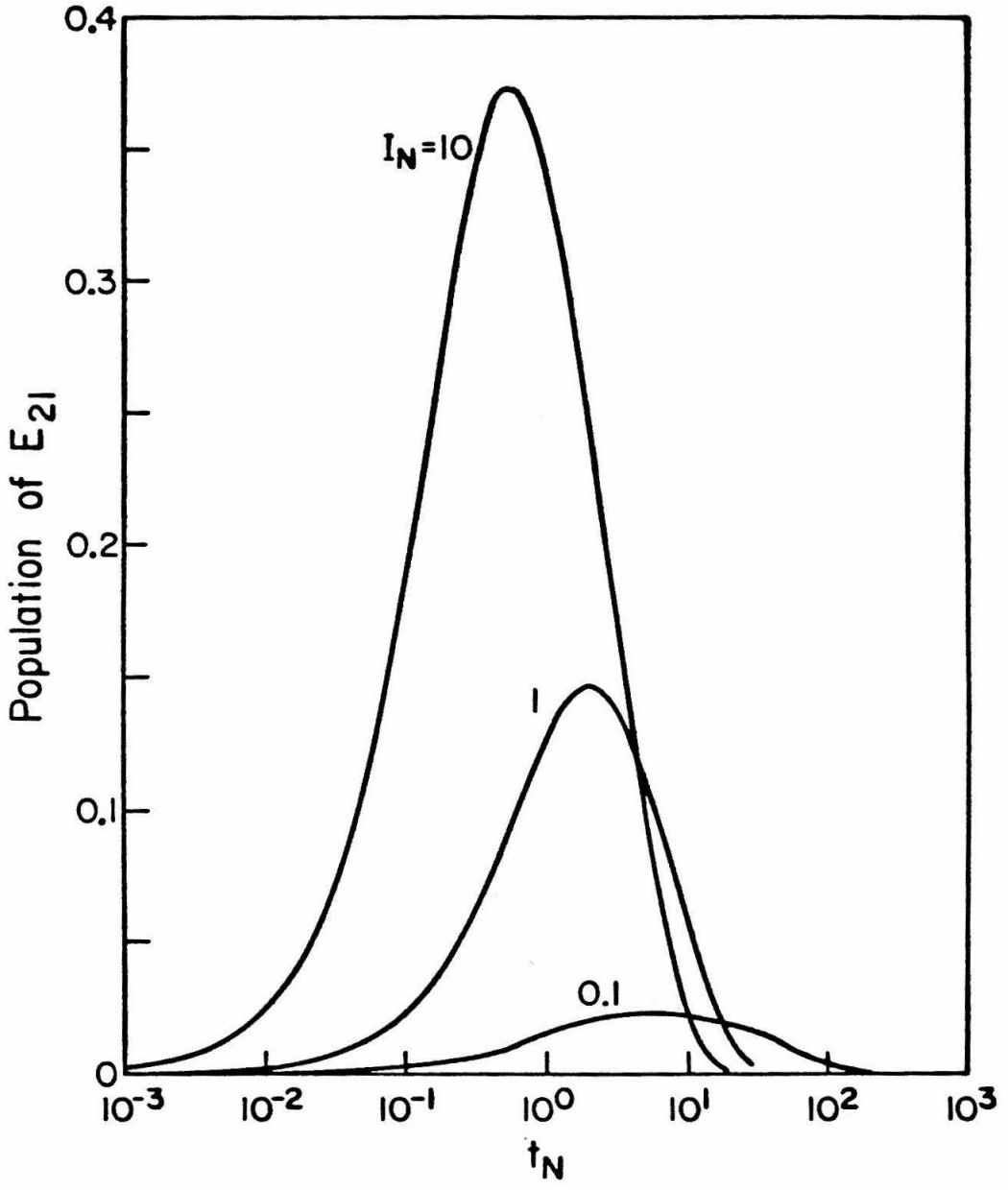

Fig. 5.5 Population of the $3P_{1/2}$ (F = 2, m = 1) excited state versus the normalized time t_N for various values of I_N.

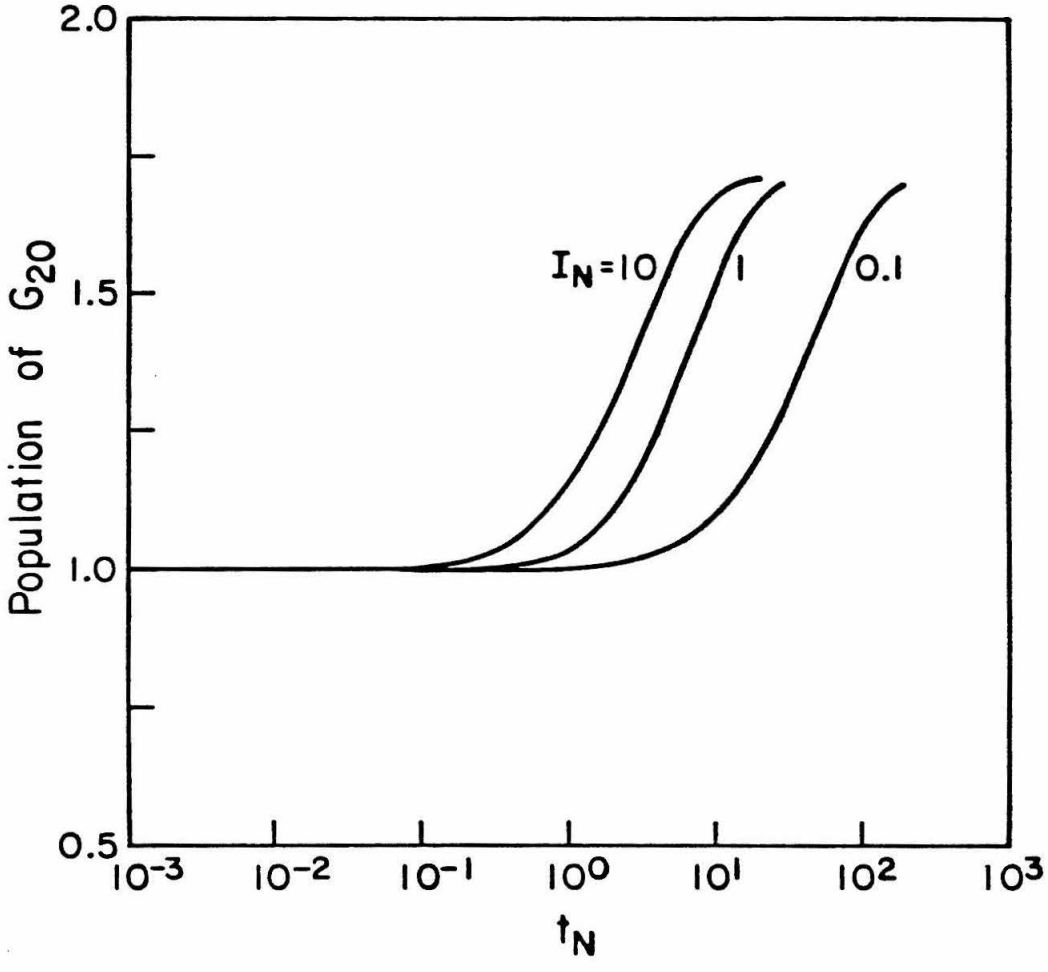

Fig. 5.6 Population of the $3S_{1/2}$ (F = 2, m = 0) ground state versus the normalized time t_N for various values of I_N.

The population of G_{11} [$3S_{1/2}(F = 1, m = 1)$] is plotted in Fig. 5.7 versus the normalized time t_N. This population grows by spontaneous decay from E_{22} and E_{21}. As with G_{20}, the population of G_{11} starts at unity and grows at a rate which is the minimum of the absorption rate, I_N, into E_{22} or the spontaneous decay rate, 1, from E_{22} andE_{21}. The population reaches an equilibrium value of 2.286. Again, G_{21} is not resonant with the laser and these atoms do not undergo any interaction with the laser.

One effect that has been neglected in the rate equations (5.8-3) is that of spin-exchange collisions between sodium atoms. The collisions tend to redistribute the atoms among both hyperfine levels (F = 2 and F =1) of the ground state, thereby allowing some of the atoms to again interact with the laser and participate in the nonlinear interactions. Anderson and Ramsey[12,13] have measured the spin-exchange cross section for sodium and determined it to be between $(1 - 3) \times 10^{-14}$ cm^2 with an average value of 1.3×10^{-14} cm^2. The time between spin exchange collisions $T_{s-p} = 1/N\sigma_0\bar{v}$ where N is the sodium atom density, σ_0 is the spin-exchange cross section, and $\bar{v}$ is the relative velocity of two sodium atoms.

To evaluate the importance of the spin-exchange collisions, let us consider a situation similar to that used in our experiments[14]. Suppose we have a sodium cell, such as that described in section 5.6, which is at a temperature T = 200°C, implying $N = 3.24 \times 10^{12}$ cm^{-3}, with a laser beam of FWHM diameter .1 cm incident on the cell. In a plane perpendicular to the laser, the atoms have an average speed of 5.18×10^4 cm/sec, using Eq. (5.7-7). If we take this as the relative velocity of two sodium atoms, then $T_{s-p} = 4.6 \times 10^{-4}$ sec. This is many orders of magnitude larger than the natural lifetime of sodium, and means that an atom travels 23.7 cm between collisions. At the temperatures and densities used in our experiments, these types of collisions play no significant role in re-equilibrating the population of the ground state hyperfine levels during interactions with the laser.

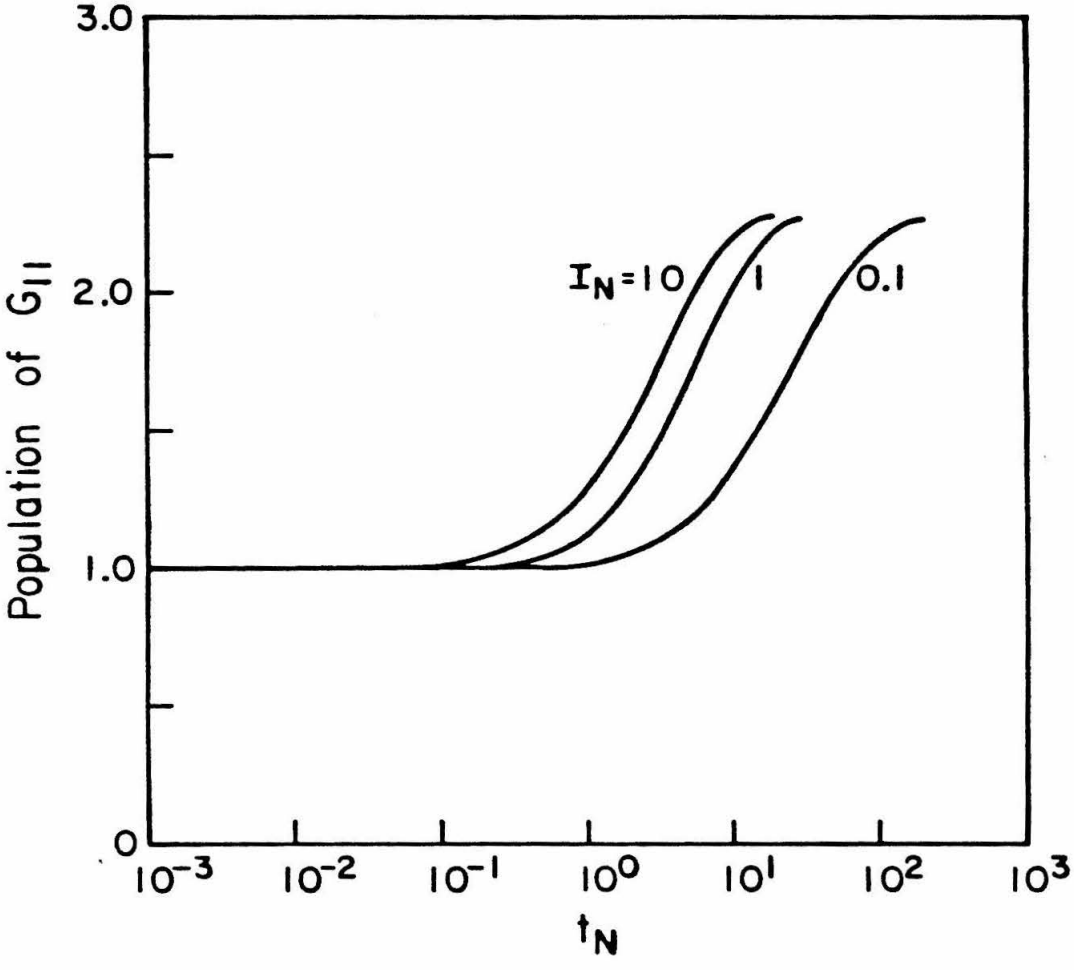

Fig. 5.7 Population of the $3S_{1/2}$ (F = 1, m = 1) ground state versus the normalized time t_N for various values of I_N.

On the other hand, the transit time of an atom through the laser beam is an important limitation on the degree of optical pumping that takes place. Consider an atom located at the center of the laser beam which is traveling perpendicular to the beam at the previously mentioned velocity. The transit time $T_{transit}$ from the center of the beam to the half power point is $T_{transit} = 9.7 \times 10^{-7}$ sec = 61 t_N using the spontaneous lifetime of sodium. The transit time plays an important role in limiting the degree of optical pumping that occurs.

5.9 Barium as a Nonlinear Medium

As discussed earlier in this chapter, sodium is not a true two-level system. The efficiency of the phase conjugate process is seriously degraded by the effects of hyperfine optical pumping. The hyperfine structure is due to the nonzero nuclear spin of the atom. An atom with a zero nuclear spin would not have these problems. Many isotopes have zero nuclear spin but would not be suitable candidates for phase conjugation because of the difficulty in working with them. This can be due to the rarity of the isotope, the high temperatures needed to attain a suitable vapor pressure, or the difficulty of finding a laser which is resonant with the atom, to give just a few examples. Several possible candidates are shown below[15,16].

ISOTOPE	TRANSITION	WAVELENGTH
Mg^{24}	$3\,^1S_0 - 3\,^1P_1$	2852.13Å
Ca^{40}	$4\,^1S_0 - 4\,^1P_1$	4226.73Å
Sr^{88}	$5\,^1S_0 - 5\,^1P_1$	4607Å
Ba^{138}	$6\,^1S_0 - 6\,^1P_1$	5535.7Å

We will consider Ba since it has a resonance in the green wavelength region which is accessible using CW dye lasers which are currently available[16].

5.10 Energy Levels of Barium

The lowest energy levels of barium[17] are shown in Fig. 5.8. The lowest allowed

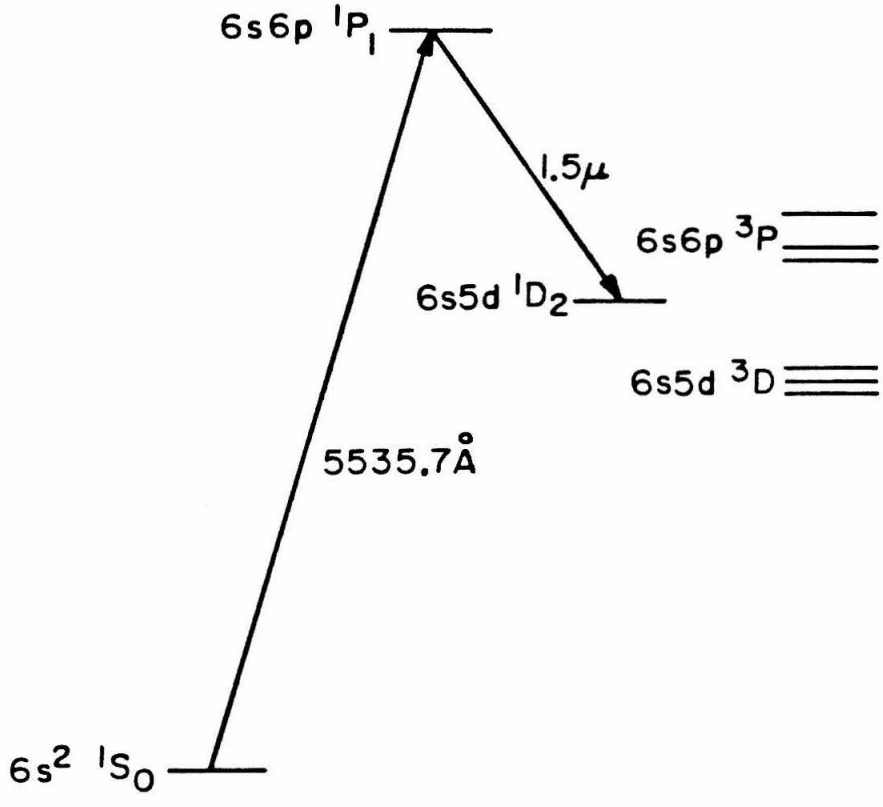

Fig. 5.8 Energy levels of barium.

transition is the $6s^2\ ^1S_0 \rightarrow 6s6p\ ^1P_1$ resonance line which occurs at a wavelength of 5535.7Å. This is the line at which we will consider doing phase conjugation. Barium has seven naturally occurring isotopes. The natural abundance of the isotopes along with their nuclear spin are given below.

Isotope	Natural Abundance(%)	Nuclear Spin I
130	0.10	-
132	0.10	-
134	2.42	0
135	6.59	3/2
136	7.81	0
137	11.32	3/2
138	71.66	0

The difference in the frequency of the $6s^2\ ^1S_0 \rightarrow 6s6p\ ^1P_1$ transitions for the various isotopes are given below relative to the ^{138}Ba transition[18]. We neglect the rare isotopes ^{130}Ba and ^{132}Ba.

Isotope	$F(^1S_0)$	$F(^1P_1)$	Shift(MHz)
138	0	1	0
137	3/2	5/2	56
137	3/2	3/2	280
137	3/2	1/2	530
136	0	1	128
135	3/2	5/2	120
135	3/2	3/2	322
135	3/2	1/2	530
134	0	1	148

5.11 Transition Rates in Barium

The lifetime of the upper 6s6p $^1P_1$ state is 8.37×10^{-9} sec[16]. This implies a natural linewidth of 19 MHz.

Now, barium has a single metastable state, 6s5d $^1D_2$, which the 6s6p $^1P_1$ state can decay to. However decay from the 6s5d $^1D_2$ state to the ground state is parity forbidden. This decay is allowed only via an electric quadrupole transition which has a lifetime roughly $(ka_0)^{-2}$ times the corresponding dipole lifetime. The lifetime of the $^1D_2$ state is approximately .5 sec[16].

The important consideration is the probability that an excited atom decays into the metastable state relative to the probability that it decays back to the ground state. This branching ratio is found from the spontaneous decay rates for the two transitions. We are indebted to the thesis work of Tony Bernhardt for the measurement of this branching ratio. Studying the separation efficiency in his barium isotope separation experiments, Tony determined an upper limit of 1/700 for the branching ratio[16] into the metastable state for ^{138}Ba. This is a much smaller branching ratio then the near unity branching ratio in the the case of sodium for the hyperfine optical pumping.

5.12 Vapor Pressure and Doppler Linewidth of Barium

Barium has a melting point of 725°C. The equilibrium between the solid and vapor phases of barium is given by

$$\log_{10} p = 14.08429 - \frac{9445.27}{T} - 1.90149 \log_{10} T + 9.646 \times 10^{-5} T \qquad (5.12\text{-}1)$$

where p is in torr and T is in degrees Kelvin[11].

The table below gives some examples of pressure and density in the temperature range of interest.

T(°C)	p(torr)	N(cm^{-3})
200	1.2×10^{-11}	2.4×10^{5}
300	2.5×10^{-8}	4.3×10^{8}
400	5.5×10^{-6}	7.8×10^{10}
500	2.8×10^{-4}	3.5×10^{12}
600	5.7×10^{-3}	6.3×10^{13}
700	6.2×10^{-2}	6.1×10^{14}

The Doppler linewidth of barium is given by

$$\Delta \nu_D = 2\nu_0 \left(3.58 \times 10^{-7} \right) \sqrt{\frac{T}{M}} \qquad (5.12\text{-}2)$$

with $\nu_0 = \omega_0/2\pi$ in Hz, T is the temperature of the gas in °K , M is the mass of one barium atom in atomic mass units, and $\Delta \nu_D$ is given in Hz.

At the temperatures considered before, the Doppler linewidths are given below for ^{138}Ba as well as the average speed of an atom in a plane.

T(°C)	$\Delta \nu_D$ (GHz)	$\bar{v}$ (cm/sec)
200	0.72	2.12×10^{4}
300	0.79	2.33×10^{4}
400	0.86	2.52×10^{4}
500	0.92	2.70×10^{4}
600	0.98	2.87×10^{4}
700	1.03	3.03×10^{4}

5.13 Conclusion

In this chapter, we have described the important properties of sodium. The wavefunctions of sodium have been determined and used to calculate the transition rates of the sodium atom in the presence of applied fields. This information has been employed to study the optical pumping problem.

Because sodium doesn't exactly model a two-level system, we then discussed barium, which is a better model of a two-level atom and which may be a more efficient material in which to do phase conjugation.

References for Chapter V

1. J. Nilsen and A. Yariv, "Nearly degenerate four-wave mixing applied to optical filters," Appl. Opt. 18,143 (1979).

2. J. Nilsen and A. Yariv, "Nondegenerate four-wave mixing in a Doppler-broadened resonant medium," J.Opt.Soc.Am. 71,180 (1981).

3. Joseph Nilsen and Amnon Yariv, "A tunable narrowband optical filter via phase conjugation by nondegenerate four-wave mixing in a Doppler-broadened resonant medium," Opt. Comm.,to be published.

4. Charlotte E. Moore, **Atomic Energy Levels, Volume I** (Superintendent of Documents, U. S. Government Printing Office, Washington 25, D. C., 1949), p. 89.

5. C. Michael Lederer and Virginia S. Shirley, **Table of Isotopes, Seventh Edition** (John Wiley & Sons, Inc., New York, 1978).

6. M. Arditi and T. R. Carver, "Optical detection of zero-field hyperfine splitting of Na^{23}," Phys. Rev. 109,1012 (1958).

7. P. Kusch and H. Taub, "On the g_J values of the alkali atoms: The hyperfine structure of the alkali atoms," Phys. Rev. 75,1477 (1949).

8. M. L. Perl, I. I. Rabi, and B. Senitzky, "Nuclear electric quadrupole moment of Na^{23} by the atomic beam resonance method," Phys. Rev. 98,611 (1955).

9. J. N. Dodd and R. W. N. Kinnear, "The hyperfine structure of the $3\,^2P_{3/2}$ state of sodium and the quadrupole moment of Na^{23}," Proc. Phys. Soc. (London) 75,51 (1960).

10. Richard B. Miles and Stephen E. Harris, "Optical third-harmonic generation in alkali metal vapors," IEEE J. Quantum Electron. QE-9,470 (1973).

11. An. N. Nesmeyanov, **Vapor Pressure of the Elements** (Academic Press, Inc., New

York, 1963), p. 443.

12. L. Wilmer Anderson and Alan T. Ramsey, "Effect of spin-exchange collisions on the optical orientation of atomic sodium," Phys. Rev. 124,1862 (1961).

13. L. Wilmer Anderson and Alan T. Ramsey, "Study of the spin-relaxation times and the effects of spin-exchange collisions in an optically oriented sodium vapor," Phys. Rev. 132,712 (1963).

14. J. Nilsen, N. S. Gluck, and A. Yariv, "Narrowband optical filter via phase conjugation by nondegenerate four-wave mixing in sodium vapor," Opt. Lett. 6,380 (1981).

15. V. S. Letokhov, V. G. Minogin, and B. D. Pavlik, "Cooling and capture of atoms and molecules by a resonant light field," Sov. Phys. JETP 45,698 (1977).

16. Anthony F. Bernhardt, "Isotope separation by laser deflection of an atomic beam," thesis, UCRL-51796 (1975).

17. Charlotte E. Moore, **Atomic Energy Levels, Volume III** (Superintendent of Documents, U. S. Government Printing Office, Washington 25, D. C., 1958), p. 132.

Chapter VI

DYE LASER AND EXPERIMENTAL APPARATUS

6.1 Introduction

The lasers used in this research are optically pumped organic dye lasers. The active ingredient in the laser gain medium is rhodamine 6G. Fig.6.1[1] shows the characteristics of this dye. The operating region of the dye is from 5730 – 6350Å. It is seen that Rh6G in ethylene glycol has its peak fluorescent amplitude near the 5890Å orange resonance line of sodium, which is why this dye solution was chosen.

The operating bandwidth of a dye laser can be made quite small[2,3], on the order of 10^5 Hz, by introducing optical elements into the laser cavity. Narrow linewidth operation can extract a significant fraction of the unrestricted broadband laser power. The reason for this is as follows[4]. Rotational levels of the dye molecules have a spacing of a hundred wave numbers or less. The energy states are not well defined; they are perturbed by electrostatic and collisional interaction with the solvent molecules so that separate vibration-rotation levels are indistinguishable by separate emission or absorption lines. Only a few collision times, on the order of 10^{-12} sec each[5], are needed to establish rotation-vibration equilibrium. Therefore, an excited electronic state with a lifetime[6] of 5×10^{-9} sec can come into rotational-vibrational equilibrium before it radiates. In equilibrium, the only states of a given electronic level to be populated will be those states within a few kT of the lowest vibration-rotation level. Therefore, emission usually occurs from the lowest vibration-rotation level of the excited electronic state, while absorption occurs from this lowest level of the ground electronic state. In the dye lasers, rapid equilibrium repopulates the lowest vibration-rotation level of the excited electronic state quickly, and depopulates the excited vibration-rotation level of the ground electronic state, which is the lower laser level. The introduction of optical elements into

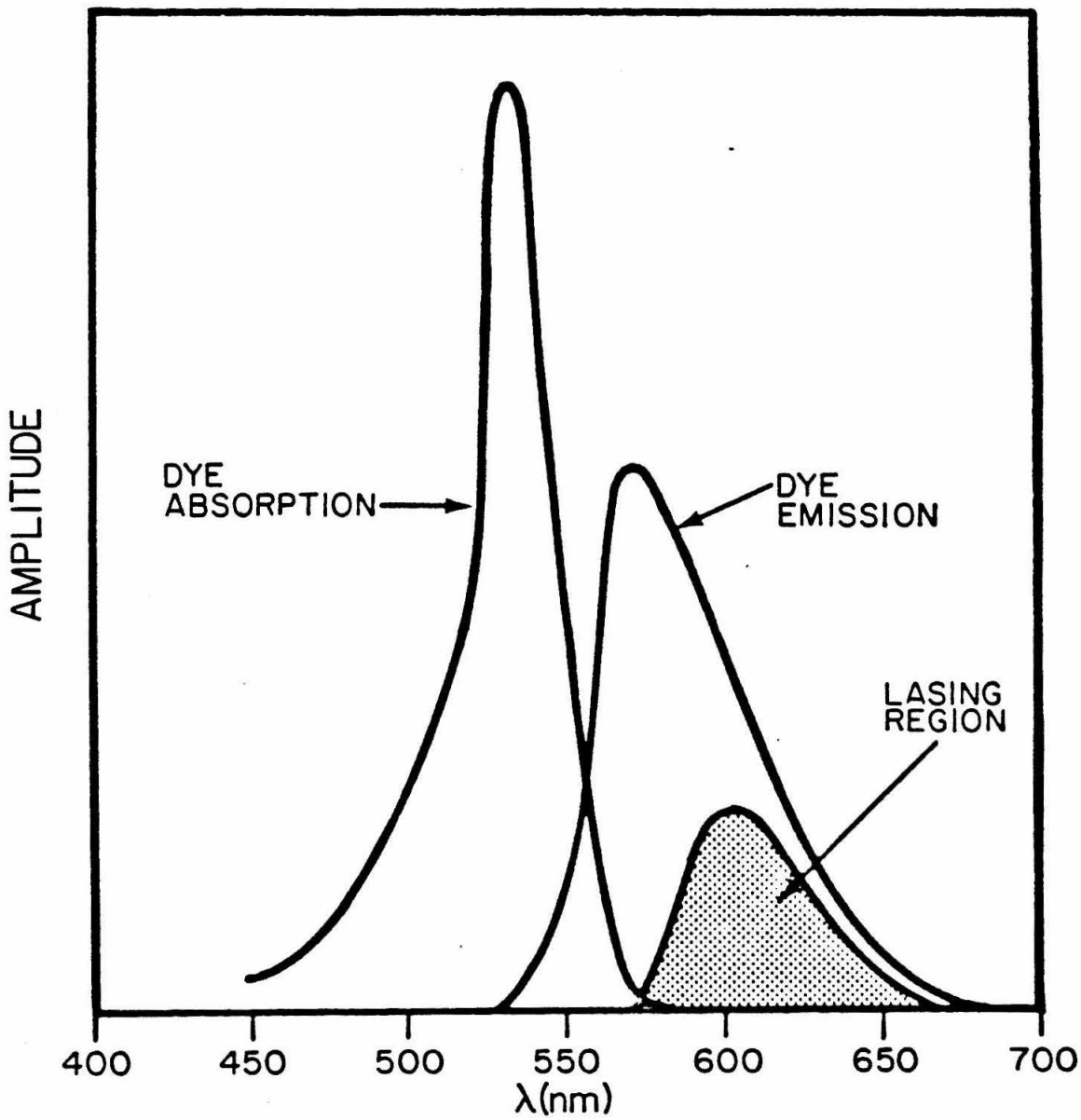

Fig. 6.1 Characteristics of Rh6G dye.

the laser cavity will prevent lasing except in a narrow frequency band. Excited molecules can then be forced to lase in this band.

6.2 Ring Dye Laser Theory

Typical single-frequency dye lasers[1] operate with a standing wave inside the dye laser cavity. An integral number of half-waves must fit inside the cavity, giving rise to a number of longitudinal cavity modes. Lasing only occurs at those frequencies corresponding to these modes. Etalons are introduced into the laser cavity to allow lasing at only one longitudinal mode in a single-frequency dye laser.

The maxima and minima of the standing wave always occur at the same points. Consequently, the dye molecules located at the minima of the standing wave are not stimulated by feedback radiation. This phenomenon of a standing wave creating regions of unused gain inside the lasing medium is called spatial hole-burning. These regions can have high enough gain to support simultaneous lasing at a different wavelength corresponding to a mode whose maxima match the unused high gain regions. This second lasing mode, when occurring, destroys the single-frequency nature of the dye laser output.

The primary laser used in this research is a Spectra-Physics Model 380A, which is a traveling-wave, ring resonator, continuous wave dye laser. It provides tunable, high power, single-frequency radiation. The conversion efficiency (ratio of the output of the dye laser to the output of the ion laser pumping the dye laser) can be as high as 23%, about four times that of a typical standing-wave dye laser.

A second laser used in the experiments was a Coherent Radiation Model 699-21 cw ring dye laser. Its general characteristics are quite similar to the Model 380A laser except for its active stabilization which is discussed later.

Since the Model 380A laser is a traveling-wave laser, the waves propagate continuously around the cavity and don't create regions of unused gain. Spatial hole-

burning, which destroys single-frequency operation, is eliminated. Inside the cavity, the traveling waves can propagate in both directions with equal probability. A unidirectional device which introduces a directional anisotropy into the cavity can be used to choose a specific propagation direction.

The combined loss of all the tuning elements (unidirectional device, birefringent filter, fine etalon and single-frequency etalon) is low compared with the loss involved in a standing wave cavity, so that our ring dye laser has much higher conversion efficiency than the standing wave single-frequency dye lasers. Also, elimination of spatial hole burning allows the laser to be pumped at higher input powers without creating extraneous modes.

6.3 Laser Description

As mentioned before, the primary laser used in our research was a Spectra-Physics Model 380A Scanning Ring Dye Laser[1]. Fig. 6.2[1] shows the beam path in the dye laser cavity. An Argon ion laser[7], Spectra-Physics Model 171, was used to pump the ring laser. An argon laser will typically operate at several wavelengths simultaneously, with the predominate wavelengths being 5145Å and4880Å for the mirror coatings used in this laser. Replacing the end mirror with a prism allows the laser to be tuned to only one wavelength. We operated the argon laser at 5145Å. Typically, the current through the plasma tube of the argon laser was set to give an output power of four watts, which was about 80% of the maximum power, at this wavelength.

A polarization rotator made of a coated crystalline quartz plate with its crystal axis perpendicular to the plane of the plate is used to rotate the vertical polarization of the pump laser 90° to the horizontal plane. This is done because the dye laser has a vertical dye jet which requires a horizontally polarized pump beam to minimize reflection loss off the jet, which is at Brewster's angle.

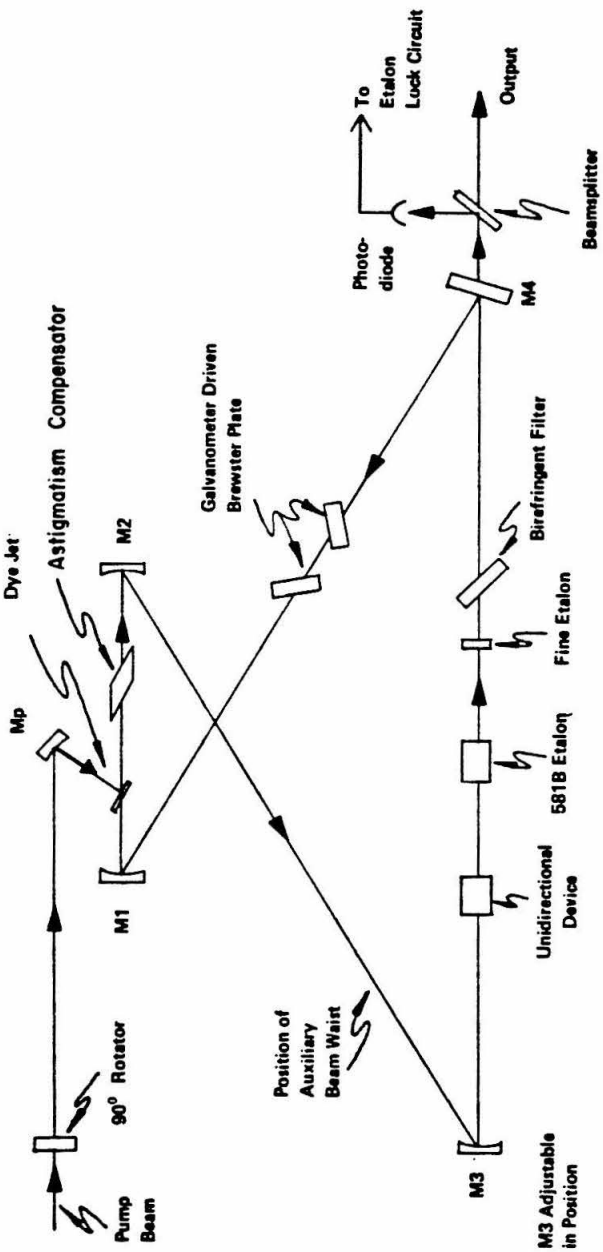

Fig. 6.2 Beam path in the Model 380A dye laser.

A pump mirror, which has a 5 cm radius of curvature, focuses the argon laser beam into the dye jet. The dye fluorescence is caught by the four- mirror cavity which uses three curved mirrors, M1, M2, M3 with radii of curvature 3.5 cm, 10 cm, and 23 cm respectively and a flat output mirror M4.

The intracavity optical elements in the laser are an astigmatism compensator, a unidirectional device, a pair of scanning galvanometers, a birefringent filter, a fine etalon, and the electronically tunable Model 581B etalon. We will now give a description of these elements and then discuss their effect on tuning and single frequency operation.

The astigmatism compensator plate is a .4 cm thick rhomb of fused silica which is placed at Brewster's angle in front of the mirror M2. It optically compensates for the astigmatism introduced by the off-axis curved mirrors used in the ring laser. Its effect is to change the output beam of the laser from the horizontal oval-shaped mode into a round beam.

The unidirectional device consists of a Faraday rotator plate and a quartz compensation plate. The plate thicknesses are designed so that for light propagating in the correct direction, the optical rotations cancel, while the rotations add for the opposite propagation direction. This introduces sufficient loss for the beam which propagates in the wrong direction, that stable, high power, one way propagation is obtained for the laser.

Each scanning galvanometer consists of a quartz plate mounted on a galvanometer, with the plate at Brewster's angle to the intracavity beam. The pair of galvanometers are mounted so that during rotation of the plates the beam displacement occurs between the pair of quartz plates, leaving the beam path unchanged in other parts of the cavity.

The birefringent filter is a three element filter made of crystal quartz cut with the optical axis in the plane of the plate. The filter is inserted into the intracavity beam at Brewster's angle. Rotating the filter causes a change in the extraordinary index of refraction as seen by the laser. Therefore, the plane of polarization is rotated. The wavelength whose rotation corresponds to an integral multiple of 2π sees minimum loss and is selected as the lasing wavelength.

The fine etalon is a thin uncoated piece of glass approximately 0.11 mm thick with a free spectral range of 900 GHz.

The 581B etalon is a plane-parallel electronically tunable Fabry-Perot etalon with a free spectral range of 75 GHz. The mirrors are coated with a 30% reflective coating. The separation between the mirrors is controlled by the length of a hollow cylindrical piezoelectric element. The etalon is tuned by changing the length of the piezoelectric element with an applied voltage.

6.4 Single-Frequency Scanning

Single-frequency operation[1] is achieved by using a birefringent filter with a fine etalon and an electronically tunable single-frequency etalon. The spectral ranges of the three frequency selection elements are chosen such that loss is introduced for all other cavity modes except for the particular one where lasing is desired.

The frequencies of the allowable lasing modes are controlled by the speed of light and the cavity length. For our Model 380A, the cavity mode spacing is about 200 MHz. To scan the output frequency, the cavity modes must be tuned by changing the length of the laser resonator. In the Model 380A ring dye laser, this change of length is accomplished with a pair of galvanometer-driven quartz plates. The index of refraction of the plates is higher than that of air. Therefore, changing the distance that the light travels inside each galvanometer plate, by rotating the plate itself, changes the effective cavity length.

The transmission peak of the scanning etalon is changed by changing the separation distance between the etalon mirrors. By scanning the inter-etalon mirror separation at the same rate as the galvanometer plate scans the cavity mode frequency, the output frequency of the single-frequency dye laser can be scanned.

The laser also has a passive stabilization loop which provides additional frequency stability to the laser. This is accomplished by putting a small 2 KHz dither signal on the voltage applied to the 581B etalon. A beamsplitter on the output end of the laser feeds a small part of the laser output into a photodiode which looks for amplitude modulation of the laser at 2 KHz. The stabilization loop then applies a voltage to the etalon to minimize the amplitude modulation. This minimization occurs when the peak transmission of the etalon is at the same frequency as the cavity length, the net result being that the stabilization loop keeps the etalon locked at the frequency of the longitudinal cavity mode.

The Coherent Radiation laser has one important difference from the Model 380A laser which should be mentioned here. It is an actively stabilized laser which, in addition to the passive stabilization loop, has an external cavity that the laser cavity is locked to by additional feedback. The external cavity is a low finesse, very stable, temperature stabilized Fabry-Perot. This results in the Coherent laser having a much narrower linewidth, approximately 1 MHz, as compared to the Model 380A (40 MHz rms).

6.5 Finding the Sodium Line

Because of the narrow bandwith of the ring dye laser(40 MHz rms) it is difficult to find an atomic transition without the aid of several frequency measuring devices. The dye laser can be scanned electronically over 75 GHz by a manual frequency scan on the electronics. The automatic frequency scan on the laser covers 30 GHz by using an internal ramp generator to apply a voltage to both the galvonometers and

the 581B etalon. A voltage divider insures that the voltage applied to the galvonometers changes the cavity length at the same rate as the voltage applied to the 581B etalon changes the center bandpass of the etalon. In addition the birefringent filter can be manually scanned over the entire range of the dye.

To find the 5890Å sodium transition we first take the output of the dye laser and put it into an optical fiber in our laboratory which runs into the neighboring lab and is butted against a second fiber which is used as the input to a one meter scanning monochromator. The output of the monochromator has a vidicon tube on it which provides input to an optical multichannel analyzer whose output is displayed on an oscilloscope. The vidicon tube has a resolution of .185Å/channel and covers about 500 channels. The monochromator was first calibrated against the known lines of a helium-neon laser and an argon laser. It was then used to determine the frequency of the dye laser enabling us to tune the birefringent filter until we were within several tenths of an angstrom of the sodium line. This was done with the fine etalon removed from the laser cavity.

Having done the crude tuning, the output of the dye laser was put into a sodium cell which would fluoresce when the laser was within the Doppler width of the transition. The automatic scan on the laser was activated to scan over 10 GHz. While the laser was scanning, the central frequency of the cavity was tuned manually, using the electronics, over 75 GHz until a flash of fluorescence was observed in the cell. The automatic scan was then turned off and the laser was tuned manually with the electronics until the laser was on the sodium line. The fine tuning etalon could then be replaced in the cavity and tuned to the sodium line.

6.6 Optical Spectrum Analyzer

The optical spectrum analyzer, which was used to monitor laser frequency, check for mode hopping during laser frequency scanning, and calibrate the extent of the

frequency scans was a Spectra Physics 470-03 spectrum analyzer[8] with a 2 GHz free spectral range.

The model 470 is a spherical mirror Fabry-Perot interferometer which is designed for high resolution optical spectroscopy. The interferometer is comprised of two identical spherical mirrors which are separated by a distance almost equal to their common radius of curvature. The mirrors are coated to work best in the 5500 – 6500Å region. The finesse of the Fabry-Perot, defined as the ratio of the free spectral range to the instrumental bandwidth, is approximately 150. The spectrum analyzer uses an auxiliary lens at its input to increase the effective aperture diameter and increase the light gathering power of the instrument. A photodiode is mounted on the back side of the Fabry-Perot to observe the fringe pattern from the interferometer. The spectrum analyzer scans in frequency by changing the cavity length. This is done by applying a voltage to the piezo-electric elements which control the separation of the mirrors in the Fabry-Perot.

6.7 Calibrated Photodiode

The photodiode used to measure the phase conjugate signal was a PIN-10D planar diffused silicon photodiode light sensor[9]. The PIN photodiode is a type in which a heavily doped p region and a heavily doped n region are separated by a lightly doped "i" region. The "i" region resistivity can range fron 10 ohm cm to 100,000 ohm cm, while the resistivities of the p and n region are less than 1 ohm cm. The output from this two terminal device is a current whose value is proportional to the input light power. The photodiode we used is optimized for voltage biased operation and has a high breakdown voltage and low capacitance. The biasing circuit is shown in Fig. 6.3. The photodiode has a 25 nanosecond response time, a 1 cm^2 active area, and a measured sensitivity of approximately .25 amps/watt of light power at 5890Å.

We carefully calibrated the photodiode at 5890Å for all the various load resistors

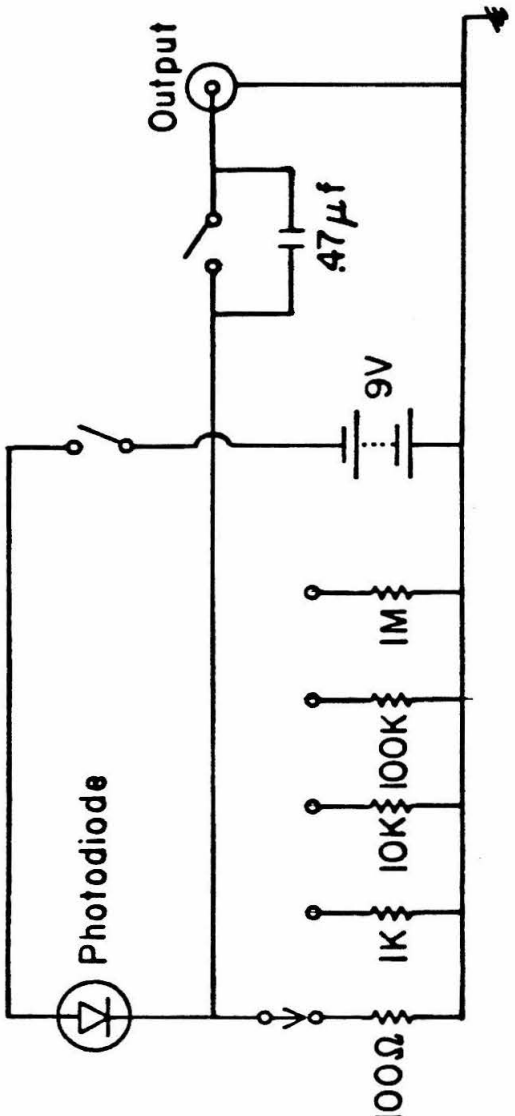

Fig. 6.3 Biasing circuit for the PIN photodiode.

and at different light levels so as to have an accurate power meter. The photodiode was calibrated against a Scientech surface absorbing disc calorimeter which is calibrated to be accurate within 1% and which has a flat spectral response over the whole optical spectrum.

6.8 Neutral Density Filters

A set of neutral density filters was used in the experiments to attenuate the laser power to enable us to study the dependence of our phase conjugate signal on the laser intensity. The filters were used because the laser itself worked best when aligned at a given power setting. Changing the dye laser power by changing the argon laser power resulted in mode hopping of the dye laser as well as amplitude instabilities in the output power as one approached the lasing threshold of the dye laser. Therefore a good set of calibrated ND filters was used to vary the dye laser power used in the experiments.

The neutral density filters used were absorption type filters whose thicknesses were varied to achieve the various optical densities. Our set of filters included optical densities .2, .4, .6, 1.0, and 2.0. The transmission of these filters were calibrated at 5890Å by using the dye laser and the PIN photodiode and measuring the power incident on the photodiode with and without the ND filters in the beam path. Of course, additional attenuators were placed in front of the photodiode to limit the power incident on it. The measurements were accurate to ± 3% due to power fluctuations in the dye laser. When calibrations were done using the argon laser as the light source, the accuracy was improved to better than ± 1%, but the absolute values of the measured transmissions were changed due to a slight frequency dependence of the filters. The change varied up to about 6%. Therefore the previous measurements had to be used. These are given below along with the calculated values of transmission.

ND filter	%T(calculated)	%T(measured)
0.2	63.1	59.5
0.4	39.8	36.8
0.6	25.1	22.5
1.0	10.0	8.5
2.0	1.00	1.07

One can see that the measured values of transmission differ from the nominal(calculated) values by as much as 15%.

6.9 Lock-In Amplifier

A Model 124A Lock-In Amplifier[10] manufactured by Princeton Applied Research was used to measure the phase conjugate signal seen by the PIN photodiode. In the experiments, the signal which is going to be phase conjugated is typically modulated by a mechanical chopper at 340 Hz. The chopper has a square wave output at the chopping frequency which provides an external reference that is used as an input to the amplifier. The lock-in amplifier will then phase-lock to this reference waveform enabling it to detect weak signals at this frequency which are buried in noise.

The lock-in amplifier was calibrated at the settings used in the experiment. The dye laser was tuned to 5890Å, attenuated by neutral density filters, sent through the mechanical chopper, and detected by the PIN photodiode which was connected to a DC voltmeter as well as the lock-in amplifier. The chopper wheel is a metal disc with six cutouts located symmetrically around the disc so that a laser incident on the rotating disc will be blocked half the time and the transmitted beam will turn on and off six times for each rotation of the disc. With the chopper turned off, the voltmeter measured the voltage from the output of the photodiode due to the unmodulated laser power incident on the detector. With the chopper turned on, the output of the lock-in amplifier was measured and compared against the DC voltmeter

measurements. The lock-in amplifier provides an output of 10 volts for an input voltage which is in phase with the reference waveform and equal in amplitude to the sensitivity setting of the amplifier. For example, with a laser power incident on the photodiode which results in a reading of 100 mV on the DC voltmeter, chopper off, the output of the lock-in amplifier, chopper on, was 4.35 volts for a sensitivity setting of 100 mV. This is about 13% less than the 5 volt output one would expect under ideal conditions; that is, if the modulated laser beam looked like a perfect sine wave at 340 Hz with an average power half of the DC laser power and the detector and amplifier operated perfectly.

6.10 Sodium Cell

In our experiments, the nonlinear material used is sodium vapor. Several sodium cells were constructed, all of roughly the same design, and tested in the experiments. The one described below is the one used to collect data in our experiments, since it worked the best of all our cells.

The sodium cell was a 2.44 cm long cylindrical quartz cell of inside diameter 2.2 cm which contained sodium metal in a sidearm. The quartz cell was evacuated to 10^{-5} torr and heated with a gas-air torch for half an hour to drive off water vapor, oxygen and other impurities. It was then filled with sodium metal in a glove box which was back filled with nitrogen gas. Cesium metal was also added to the cell. The cesium resonances are far from the sodium transition used and do not affect the nonlinear process. However the presence of the cesium seemed to help keep the windows of the cell clear. The cell was then attached to a vacuum line and again pumped down to 10^{-5} torr and sealed off while being pumped by the diffusion pump.

The next step was to make a little oven around the cell. To do this we attached to either end of the cell 5 cm long quartz sleeves whose diameters were identical to the cell. The cell was wrapped with forty turns of nichrome wire which was connected to

a variac. The quartz sleeves were each wrapped with thirty two turns of the nichrome wire which were joined in series and wired to a second variac. The nichrome wire used was size #29 which was double glass insulated so as to work up to 200°C. The whole structure was wrapped with four layers of asbestos tape to insulate it and provide temperature stability. The sodium vapor is provided by heating the cell. The sodium vapor density is determined by the liquid vapor equilibrium discussed in section 5.6. The cell is heated by applying a voltage to the heater wire. The glass sleeves are kept at a higher temperature in order to maintain the windows of the cell at a high enough temperature to stop the sodium from depositing on the windows. Otherwise a film of sodium will fog the windows, making the cell opaque. A torch can be used to clear the windows, but the sodium tends to attack the quartz and turn it brown when heated too much.

This cell worked so well partly because great care was taken to carefully clean any sodium off the windows after the cell was sealed off and before the oven was built around the cell. After constructing the oven around the cell, we were very careful to heat up the windows first to a high enough temperature to insure that the sodium would not deposit on the windows when the cell itself was heated up. We used our past experience with other cells to provide us with the information on what voltages could be applied to the cell and sleeves without fogging the windows.

6.11 Conclusion

In this chapter, we have discussed the basic operating principles of dye lasers and then explained the detailed operation of the ring dye lasers used in our experiments. For the sodium cell, we presented an explanation of the methods used to fill the cell, as well as the details of constructing an oven around the cell. The calibration of the neutral density filters which are used to attenuate the pump laser and the biasing and calibration of the photodiode used to measure the phase conjugate

signal are given. We also discussed the optical spectrum analyzer used to monitor the frequency stability of the dye lasers, thereby enabling us to determine when the lasers were operating well enough to conduct the experiments.

References for Chapter VI

1. **Spectra-Physics Model 380A Ring Dye Laser Instruction Manual**, Spectra-Physics, 1250 W. Middlefield Road, Mountain View, California 94042.

2. R. L. Barger, M. S. Sorem, and J. L. Hall, "Frequency stabilization of a cw dye laser," Appl. Phys. Lett. 22, 573 (1973).

3. F. Y. Wu, R. E. Grove, and S. Ezekiel, "CW dye laser for ultrahigh-resolution spectroscopy," Appl. Phys. Lett. 25, 73 (1974).

4. Anthony F. Bernhardt, "Isotope separation by laser deflection of an atomic beam," thesis, UCRL-51796 (1975).

5. B. B. Snavely, "Flashlamp-excited organic dye lasers," Proc. IEEE, 57, 1374 (1969).

6. B. B. Snavely and O. G. Peterson, "Experimental measurement of the critical population inversion for the dye solution laser," IEEE J. Quantum Electron. QE-4, 540 (1968).

7. **Spectra-Physics Model 171 Ion Laser with Model 270 Power Supply Instruction Manual**, Spectra-Physics, 1250 W. Middlefield Road, Mountain View, California 94042.

8. **Spectra-Physics Model 470 Optical Spectrum Analyzer Instruction Manual**, Spectra-Physics, 1250 W. Middlefield Road, Mountain View, California

9. **Planar Diffused Photodiode Series Data Sheet 9F002**, United Detector Technology Inc., 3939 Landmark Street, Culver City, California 90230.

10. **Model 124A Lock-In Amplifier Operating and Service Manual**, Princeton Applied Research, P. O. Box 2565, Princeton, New Jersey 08540.

Chapter VII

NARROWBAND OPTICAL FILTER VIA PHASE CONJUGATION BY NONDEGENERATE FOUR-WAVE MIXING IN SODIUM VAPOR

7.1 Introduction

In the first four chapters we analyzed phase conjugation via nondegenerate four-wave mixing and demonstrated theoretically that this process is capable of yielding a narrow-bandpass optical filter[1-6]. The filter bandpass has been shown to be a function both of phase mismatch constraints and the frequency dependence of the coefficients coupling the waves in the nonlinear process. Optical filtering has recently been demonstrated in CS_2, a transparent medium, using high power pulsed lasers to provide the pump waves needed in the nonlinear process[7]. The filtering was dependent only on the phase mismatch constraints in this type of medium. Saikan and Wakata[8] demonstrated optical filtering in sodium vapor using pulsed dye lasers to provide the pump waves. Their lasers had a linewidth of 9 GHz and were therefore three orders of magnitude broader than the natural linewidth of sodium. The effects they observed were dominated by phase mismatch constraints. In this chapter, we present the first experimental demonstration of optical filtering by phase conjugation in a resonant system using narrow bandwidth dye lasers which can resolve the frequency dependence of the coupling coefficients[9]. The resonant system, sodium in this case, has the advantage of providing much larger nonlinear coupling constants than a transparent medium, enabling one to use low power cw lasers to provide the pump waves. The filter response also depends on the frequency dependence of the coupling coefficients which can result in a much narrower filter than a transparent medium. An ultrahigh-Q filter with a FWHM bandwidth of 41 MHz is demonstrated in our experiments.

7.2 Experimental Setup

The output of a passively stabilized Spectra Physics cw ring dye laser at 5890 Å provides the counterpropagating pump waves. The laser output is first passed through a set of plano convex lenses, with focal lengths 50 mm and 100 mm respectively, to expand and collimate the beam. The beam is then linearly polarized by being passing through a glan prism. The linearly polarized beam then goes through a quarter wave plate which has been cut for 5890 Å. This results in a circurlarly polarized beam which passes through the nonlinear medium and is retroreflected by a broadband dielectric mirror to provide the second counterpropagating pump wave. This choice of polarization provides optical isolation of the counterpropagating pump from the laser. An actively stabilized Coherent Radiation cw ring dye laser generates the signal wave, which intersects the pump wave at an angle of 0.39°.

Sodium vapor acts as the nonlinear medium. A 2.44 cm long cylindrical quartz cell of diameter 2.2 cm contains sodium metal in a sidearm. As described in the previous chapter, the cell is heated to provide the sodium vapor. Cesium metal was also present in the cell. It provides a background pressure of 10^{-2} torr of cesium vapor. The cesium resonances are far from the sodium transition used, and do not affect the nonlinear process. As stated previously, the presence of the cesium seemed to help keep the windows of the cell clear.

The signal wave is chopped mechanically at 340 Hz and the phase conjugate signal is detected by a PIN photodiode connected to a lock-in amplifier to provide an excellent signal to noise ratio.

Fig. 7.1 shows the experimental setup. The pump beam has a FWHM diameter of .106 cm and a maximum power of 35.2 mW at the entrance to the cell. The signal beam has a FWHM diameter of .15 cm and provides .3 mW of power. The beam diameters were measured by placing a 25μm pinhole on an x-y translation stage in

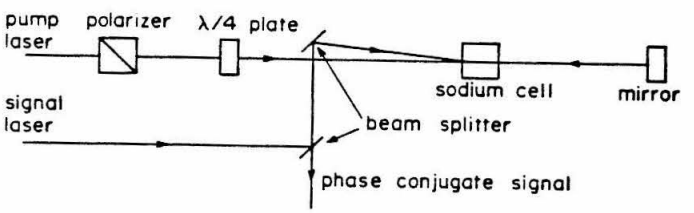

Fig. 7.1 Experimental setup for cw nondegenerate phase conjugation.

front of the beam. Behind the pinhole was a photodiode to measure the power transmitted through the pinhole. Initially, the pinhole was placed in the center of the beam. Then the output of the photodiode was measured as the pinhole was translated horizontally across the diameter of the beam. The pinhole was then returned to the center of the beam and scanned vertically over the beam. These values were then fit to a gaussian profile in each dimension. The geometric average of the values for the two dimensions was used to determine a FWHM diameter for the beam.

7.3 Discussion of Experimental Results

In this experiment, a phase conjugate signal is generated by the coupling of two counterpropagating pump waves to a signal wave by an intensity dependent modulation of the atomic population. Physically, the signal wave and one of the pump waves form an absorption grating which diffracts the second pump wave to create the phase conjugate wave. Fig. 7.2 shows the frequency dependence of degenerate phase conjugation in sodium when both pump and signal waves are provided by one laser tuned to the $3S_{1/2}$ to $3P_{3/2}$ transition at 5890Å. The pump power is 35.2 mW. The large set of peaks on the left corresponds to the laser tuning through the F=2 hyperfine line of the sodium ground state while the smaller peaks are due to tuning through the F=1 hyperfine level of the ground state. In the nondegenerate case, the pump laser is tuned to the stronger peak of the $3S_{1/2}$ (F=2) to $3P_{3/2}$ (F=3) transition shown in Fig. 7.2. The temperature of the sodium cell is adjusted to provide a saturated pump wave transmission of 46% through the cell. This corresponds to a sodium density of $5 \cdot 10^{11}/cm^2$. The pump power is 31.5 mW. The signal laser is then scanned in frequency through the transition at 5890Å and the measured phase conjugate signal is shown in Fig. 7.3. The observed signal has a FWHM bandwidth of 48 MHz and a peak reflectivity of $4 \cdot 10^{-3}$. When the pump laser is tuned to each of the other three peaks in Fig. 7.2 and the signal laser scanned, we observe a similar

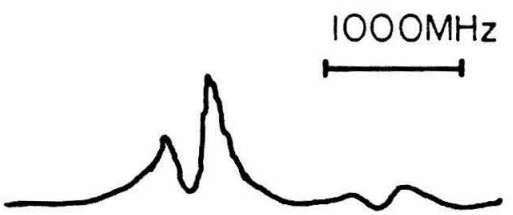

Fig. 7.2 Reflectivity for degenerate phase conjugation versus laser tuning for the $3S_{1/2}$ to $3P_{3/2}$ transition. The laser intensity for the pump wave is 2800 mW/cm^2.

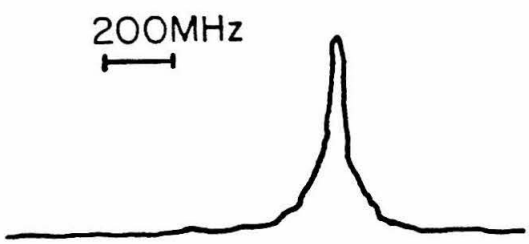

Fig. 7.3 Reflectivity for nondegenerate phase conjugation versus signal laser tuning with the pump laser fixed on the stronger peak of the $3S_{1/2}$ (F=2) to $3P_{3/2}$ (F=3) transition. The laser intensity for the pump wave is 2500 mW/cm^2.

frequency response but the reflectivities are smaller.

An independent photomixing experiment verifies that the peak of the signal occurs when the pump and signal lasers are degenerate. This is done by taking part of the pump laser and aligning it to be collinear with the signal laser. The set of collinear beams goes through the experimental setup shown in Fig. 7.1. A fast photodiode is put on the back side of one of the beam splitters to measure the interference between the two lasers. The photodiode output is measured by a microwave spectrum analyzer to detect a beat signal between the two lasers due to a frequency difference. After scanning the signal laser to observe the nondegenerate four-wave mixing, we scan a second time to observe when the beat frequency goes to zero, and we note this on the same oscilloscope trace as the phase conjugate signal.

The saturated transmission of the pump wave by the sodium vapor is determined by measuring the power of the pump wave transmitted through the cell when the laser is tuned to the peak of the sodium transition as in Fig. 7.2. The power is measured by placing a photodiode behind the sodium cell and in front of the mirror used to retroreflect the pump wave. Then the pump laser is detuned from the sodium line so that there is no absorption and the power of the pump wave transmitted through the cell is again measured. The ratio of these measurements gives the saturated transmission through the cell. To determine the sodium density we must first determine the unsaturated absorption coefficient from the measured saturated absorption coefficient. If we assume that the intensity of the pump wave which was detuned from the sodium line is I_0 while that of the absorbed pump wave is I_{abs} then we can calculate the saturated absorption coefficient, α_{sat}, to be

$$2\alpha_{sat}L = \ln(I_0/I_{abs})$$

The unsaturated absorption coefficient, α_{unsat}, can be determined from

$$\alpha_{sat} = \frac{\alpha_{unsat}}{\sqrt{1 + \frac{I_0}{I_s}}}$$

We have measured the line center absorption as a function of I_0 to determine a best fit to this formula. It gives a value of 19.2 mW/cm^2 for I_s, which is approximately the saturation intensity for sodium. We can now determine α_{unsat}. Now we can use

$$2\alpha_{unsat}L = 2 \cdot \frac{5}{8} \cdot \sqrt{\pi \ln 2}\, \frac{\Delta\nu_N}{\Delta\nu_D}\, \frac{\lambda^2}{2\pi} NL$$

where $\lambda^2/2\pi$ is the line center absorption cross-section for the transition, 5/8 is the fraction of the total atoms in the F = 2 ground state, 2 is the ratio of the degeneracies of the $3P_{3/2}$ excited state to the $3S_{1/2}$ ground state, L is the interaction length of the laser with the sodium vapor, N is the atomic density, and $\sqrt{\pi \ln 2}\, \Delta\nu_N/\Delta\nu_D$ is the fraction of the atoms which are resonant with the laser tuned to line center due to Doppler broadening.

In Fig. 7.4, the frequency dependence of degenerate phase conjugation is shown with the pump power attenuated to 2.4 mW. The angle between the signal and pump waves is now .32°. There is now one peak when the laser is tuned through the F=2 hyperfine line. This single peak narrows even more as the pump power is reduced with its bandwidth limited by the natural linewidth of sodium[10,11]. The pump laser is now tuned to the peak of the $3S_{1/2}$ (F=2) to $3P_{3/2}$ (F=3) transition shown in Fig. 7.4. The sodium density is adjusted to provide a saturated pump wave transmission of 48% through the cell, which corresponds to a sodium density of $1 \cdot 10^{11}$/cm^2. The pump power is 2.5 mW. The signal laser is frequency scanned and the resulting phase conjugate signal is shown in Fig. 7.5. The FWHM bandwidth is measured to be 41 MHz with a peak reflectivity of $6 \cdot 10^{-6}$. The bandwidth remains basically unchanged at the lower pump power but the reflectivity is greatly reduced.

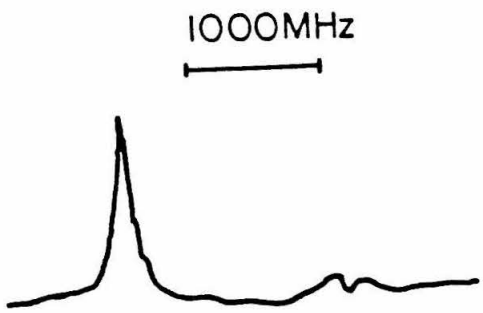

Fig. 7.4 Reflectivity for degenerate phase conjugation versus laser tuning for the $3S_{1/2}$ to $3P_{3/2}$ transition. The laser intensity for the pump wave is 190 mW/cm^2.

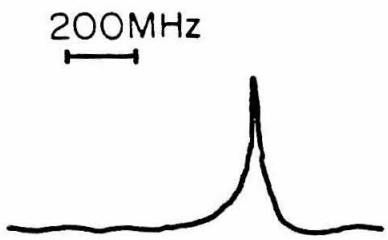

Fig. 7.5 Reflectivity for nondegenerate phase conjugation versus signal laser tuning with the pump laser fixed on the $3S_{1/2}$ (F=2) to $3P_{3/2}$ (F=3) transition. The laser intensity for the pump wave is 200 mW/cm^2.

7.4 Conclusion

We have demonstrated an optical filter with a minimum FWHM bandwidth of 41 MHz. From phase mismatch constraints alone, one can calculate a FWHM bandwidth of 5.2 GHz[4]. The frequency response of a resonant two level system is limited by the T_2 transverse relaxation time[1-3,5,6]. If we assume $T_2 = 2T_1$ (T_1 is the natural lifetime, 16 nanosecs for sodium), then the theory for a Doppler broadened two level system yields a FWHM bandwidth of 13 MHz at low intensities[2,3]. In our system, the frequency jitter of the two dye lasers appears to limit our bandwidth to 40 MHz. It is important to note that we do not observe any significant change in the filter bandwidth as the pump power is increased. Also, the Rabi sidebands which are theoretically predicted[6] are not observed. The maximum pump intensity used in these experiments is already two orders of magnitude greater than the saturation intensity of sodium. This suggests that much higher pump powers can be used without seriously affecting the filter bandwidth. A maximum reflectivity of $4 \cdot 10^{-3}$ is observed for the filter. However, recent degenerate phase conjugation experiments in sodium vapor have demonstrated amplified reflectivity exceeding unity using a cw dye laser with a maximium power of one watt[12]. This suggests that a highly efficient narrow bandwidth filter can be constructed using a resonant medium such as sodium. In sodium, it should be noted that hyperfine optical pumping transfers the population of the ground state hyperfine level resonant with the laser into the other ground state hyperfine level, thereby diminishing the efficiency of the phase conjugation process. Resonant systems which do not suffer from this effect, such as an atomic system with zero nuclear spin, should be more efficient and allow much lower cw pump powers to be used. One disadvantage of the Doppler broadened system is the narrow field of view of the filter. The maximum phase conjugate signal is observed in a collinear geometry. The acceptance angle(angle between the signal and pump waves such that the reflectivity is reduced by one half from the collinear geometry)

of the filter is approximately the ratio of the natural line width to the Doppler width[2,3].

The central frequency of the filter can be selected to coincide with that of the hyperfine transitions. The splitting between the two components of the F=2 hyperfine transition in Fig. 7.2 is intensity dependent and increases as the square root of the pump wave intensity in our experiments. The filter therefore has a limited tuning range which is a function of pump intensity. Additional tuning could be achieved by detuning the pump laser from the atomic resonance as the filter's frequency bandpass is centered at the frequency of the pump wave. This would be at the expense of the phase conjugate efficiency[1-3], however.

References for Chapter VII

1. J. Nilsen and A. Yariv, 'Nearly degenerate four-wave mixing applied to optical filters," Appl. Opt. 18,143 (1979).

2. J. Nilsen and A. Yariv, 'Nondegenerate four-wave mixing in a Doppler-broadened resonant medium," J.Opt.Soc.Am. 71,180 (1981).

3. Joseph Nilsen and Amnon Yariv, "A tunable narrowband optical filter via phase conjugation by nondegenerate four-wave mixing in a Doppler-broadened resonant medium," Opt. Comm. 39,199 (1981).

4. D. M. Pepper and R. L. Abrams, 'Narrow optical bandpass filter via nearly degenerate four-wave mixing," Opt. Lett. 3,212 (1978).

5. Fu Tao-Yi and M. Sargent III, 'Effects of signal detuning on phase conjugation," Opt. Lett. 4,366 (1979).

6. D. J. Harter and R. W. Boyd, 'Nearly degenerate four-wave mixing enhanced by the ac Stark effect," IEEE J. Quantum Electron. QE-16,1126 (1980).

7. L. K. Lam and R. W. Hellwarth, "A wide-angle narrowband optical filter using phase-conjugation by four-wave mixing in a waveguide," Eleventh International Quantum Electronics Conference 1980. Also, private conversation with Dr. R. W. Hellwarth.

8. S. Saikan and H. Wakata, "Configuration dependence of optical filtering characteristics in backward nearly degenerate four-wave mixing," Opt. Lett. 6,281 (1981).

9. J. Nilsen, N. S. Gluck, and A. Yariv, 'Narrowband optical filter via phase conjugation by nondegenerate four-wave mixing in sodium vapor," Opt. Lett. 6,380 (1981).

10. L. M. Humphrey, J. P. Gordon, and P. F. Liao, "Angular dependence of line shape and strength of degenerate four-wave mixing in a Doppler-broadened system with optical pumping," Opt. Lett. 5,56 (1980)

11. P. F. Liao, D. M. Bloom, and N. P. Economou, "CW optical wave-front conjugation by saturated absorption in atomic sodium vapor," Appl. Phys. Lett. 32,813 (1978)

12. R. C. Lind, D. G. Steel, J. F. Lam, R. K. Jain, and R. A. McFarlane, "Studies of degenerate four-wave mixing in atomic and molecular systems," Eleventh International Quantum Electronics Conference 1980. Also, private communications with Dr. Duncan G. Steel of the Hughes Aircraft Research Laboratories.